INVESTIGATION ON MULTI-CORE FIBER AND FEW-MODE FIBER AND THEIR APPLICATIONS ON OPTICAL FIBER SENSING

TAN FENGZE

PhD

The Hong Kong Polytechnic University

2020

The Hong Kong Polytechnic University

Department of Electronic and Information Engineering

INVESTIGATION ON MULTI-CORE FIBER AND FEW-MODE FIBER AND THEIR APPLICATIONS ON OPTICAL FIBER SENSING

TAN FENGZE

A thesis submitted in partial fulfillment of the requirements for the degree of

Doctor of Philosophy

August 2019

Certificate of Originality

I hereby declare that this thesis is my own work and that, to the best of my knowledge and belief, it reproduces no material previously published or written, nor material that has been accepted for the award of any other degree or diploma, except where due acknowledgement has been made in the text.

.... (Signed)

Fengze Tan

.... (Name of student)

Abstract

Few-mode fiber (FMF) and multi-core fiber (MCF) are two typical specialty optical fibers in the space-division multiplexing (SDM) system, in which modes and cores act as independent channels to carry information in order to achieve capacity improvement. In addition to the SDM communication system, FMF and MCF also show excellent performance in the optical fiber sensing community. The properties of mode and cores can be utilized for the measurement of many parameters. This thesis focuses on investigating the FMF and MCF, and further exploring their sensing applications.

Firstly, based on the basic parameters of FMF, mode calculation is presented in detail, and the electric field distribution of the modes, including the fundamental mode and high-order modes, is simulated. According to mode properties, a novel technique named spatially and spectrally resolved (S^2) imaging is introduced and employed for mode characterization in FMF. Based on the proposed signal processing method, as a result, the differential mode group delay between modes, intensity as well as phase distribution of modes and mode coupling in FMF are obtained. Besides, the S^2 imaging system is modified and accurate mode characterization is achieved, then an advanced algorithm is also proposed for detailed mode-pairs classification. For FMF-based sensing, a miniatured modal interferometer based on mode interference in FMF is explored and also demonstrated for temperature measurement. As a result, dual-sensitivity performance is achieved, which can be utilized for multi-parameters measurement.

Similar to modes in FMF, the cores in MCF can be also utilized in some novel sensing applications. Thus, in this thesis, a torsion sensor based on inter core-mode coupling in seven-core fiber (SCF) is proposed. The torsion sensor is designed

by tapering a SCF and splicing single-mode fibers (SMFs) on both ends. As a result, different sensitivities are achieved with different pre-twist angles on tapered SCF, and the highest can reach 1 nm/°, which stands out in current torsion sensors. Besides, this torsion sensor is also demonstrated to achieve twist direction discrimination with stable performance. The mode coupling dynamics and optical anisotropy are theoretically analyzed in twisted SCF to discuss the sensitivity performance. This work demonstrates the potential sensing application of MCF.

Finally, another novel sensing application of FMF and MCF, the non-invasive vital signs monitoring, is investigated. The monitors are based on the interference of modes and cores, which can help to design and fabricate in-line interferometers for stable as well as accurate vital signs monitoring. The twin-core fiber (TCF) sensor is firstly designed by splicing SMFs on both ends with optimized offset distances. The fabricated sensor is embedded as a smart mattress, and both heartbeat rate (HR) and respiration rate (RR) are obtained successfully in a non-invasive way. In addition, the SCF and two kinds of FMFs, including two-mode fiber and four-mode fiber, are fabricated as in-line interferometers for contactless vital signs monitoring. FMF-based interferometers can realize simultaneous HR and RR monitoring while the SCF can monitor the RR accurately. Besides, traditional Mach-Zehnder interferometers are leveraged for remote activities monitoring and myocardial contractility assessment. In summary, based on the properties of modes and cores, FMF and MCF are demonstrated with excellent performance in temperature sensing, torsion sensing and non-invasive vital signs monitoring.

Acknowledgements

At this moment, I realize I almost reach the end of my Ph.D. study. I have so many people to express my sincere appreciation hereby. Firstly, I would like to thank my supervisor, Prof. Changyuan YU. He provided me the opportunity to study at The Hong Kong Polytechnic University and supported me in doing research work in his group. His passion for career, patriotism and kindness deeply impressed me. Also, it is his guidance and support that guides me to devote to entrepreneurship after graduation. I cannot predict my career, but I am sure I must try this time and work as hard as possible in the upcoming few years. I am fortunate and feel grateful that I can under Prof. YU's supervision and feel hopeful with our future collaboration.

Also, I want to thank Prof. Chao LU and Prof. Hwa-yaw TAM, who always gave me suggestions generously and helped me to overcome the difficulties. Their attitudes towards research and life also profoundly affected me. Besides, I would like to thank their group members, including Dr. Xin Cheng, Miss. Jingxian Cui, Pendy, Dash, Dinusha, and Dr. Jijun He. Especially, I want to express my appreciation to Dr. Zhengyong Liu, a senior research fellow in Prof. TAM's group. He helped me a lot with my first journal article, including experiment details, draft revision and publication. Without his patience and help, I cannot finish my Ph.D. study smoothly.

For the projects during my Ph.D. study, I want to thank Miss. Shuyang Chen for her help and support in the nursing house project. She is going to begin her Ph.D. study in our team and best wishes to her. In the nursing house project, I also want to thank Mr. Weimin Lyu, who is currently a master student in our group, Mr. Zhenyu Huang, who is now an excellent engineer in Huawei, and Henry, Louis, Alex, Robert and Michael from Industrial Center in PolyU. This project is still going on, and I believe I can complete it with satisfying results. Here I also want to thank Mr. Wei

Xu and Miss. Na Zhang from National University of Singapore Suzhou Institute. Without their help, I cannot proceed with this project.

During my Ph.D. study, I feel very grateful to join polyu yu team. They are all very nice to me, including Dr. Yi Liu, Dr. Jiajing Tu, who is a professor now in Jinan University and wish her smooth career, Mr. Biwei Wang, Mr. Zhuo Wang, Mr. Weihao Yuan, Mr. Huaijian Luo, Ms. Wenxuan Wang, Dr. Xiaodi You, Dr. Yan Li, Dr. Xinwei Du, Dr. Min Xue, Dr. Shandong Dong, Mr. Zhongxu Liu and Noman. My thanks are also extended to the General Office in Department of Electronic and Information Engineering and Research Office in PolyU.

Hereby, I also want to thank my friends in the gym, including Miss. Yisui Li, Ms. Mianmian Cai, Mr. Yiming Li and Mr. Xihui Liang. Thank you guys so much for the happiness you shared with me. I wish you happy forever. Also, appreciate the facilities in PolyU, such as canteens, hall and gyms.

Finally, I would like to express my gratitude to my family, my parents and sister, my grandfather and my grandmother. My grandfather fell ill recently, and I wish he can recover soon.

August 2019

Contents

List of abbreviations

A	
ADRD	Alzheimer’s disease and related dementia
ANS	Autonomic nervous system
B	
BLS	Broadband light source
BCG	Ballistocardiogram
bpm	Beat per minute
BL	Bending loss
C	
C.W	Clockwise
C.C.W	Counterclockwise
COPD	Chronic obstructive pulmonary disease
CHF	Congestive heart failure
D	
DOF	Degree of freedom
DMGD	Differential mode group delay
DAQ	Data acquisition
DFB	Distributed feedback
DSP	Digital signal processing
E	
EDFA	Erbium doped optical fiber amplifier
ER	Extinction ratio
EMI	Electromagnetic interference
ECG	Electrocardiography
F	
FMF	Few-mode fiber
FM-MCF	Few-mode multi-core fiber
FUT	Fiber under test
FWMH	Full width at half maximum height
FM	Fundamental mode
FFT	Fast Fourier transform
FBG	Fiber Bragg grating

FP	Fabry-Perot
FSR	Free spectrum range
H	
HOM	High-order mode
HR	Heart rate
HP	High-pass
HRV	Heart rate variability
L	
LP	Linear polarization
LPG	Long period grating
M	
MCF	Multi-core fiber
MMF	Multi-mode fiber
MZI	Mach-Zehnder Interferometer
MDM	Mode-division multiplexing
MMI	Miniaturized modal interferometer
MIMO	Multiple-input-multiple-output
MC	Mode coupling
MCU	Microprogrammed control unit
N	
NA	Numerical aperture
O	
OSA	Optical spectrum analyzer
OTDR	Optical time-domain reflector
P	
PCA	Principle component analysis
PD	Photodetector
PNS	Parasympathetic nervous system
PEP	Pre-ejection period
R	
RI	Refractive index
RR	Respiration rate
RAM	Remote activity monitoring
RCT	Randomized controlled trial

S

SMF	Single mode fiber
SDM	Space-division multiplexing
S^2	Spatially and spectrally resolved
SI	Sagnac interferometer
SPR	Surface plasmon resonance
SNS	Sympathetic nervous system
SWD	Sleep/wake cycle disturbance

T

TMF	Two-mode fiber
TLS	Tunable laser source
TA-MCF	Trench assisted MCF
TA-SCF	Trench assisted SCF
TCF	Twin core fiber
TC-PCF	Twin core photonic crystal fiber

U

UDP	User datagram protocol

W

WDM	Wavelength division multiplexing

List of major notations

n_{core}	Refractive index of core
$n_{cladding}$	Refractive index of cladding
β	Propagation constant
k_0	Wave number in vacuum
U	Normalized transverse phase parameter
W	Normalized transverse attenuation parameter
E_r	Electric field component in radial direction
E_φ	Electric field component in angular direction
E_z	Electric field component in axial direction
l	Order of Bessel function
V_c	Cutoff frequency
I_{core}	Intensity of core mode
$I_{cladding}$	Intensity of cladding mode
λ_d	Dip wavelength monitored
A_{01}	Electric field amplitude of LP_{01} mode
A_{11}	Electric field amplitude of LP_{11} mode
Ψ_{01}	Electric field distribution of LP_{01} mode
Ψ_{11}	Electric field distribution of LP_{11} mode
L	Length of optical fiber
β_{01}	Propagation constant of LP_{01} mode
β_{11}	Propagation constant of LP_{11} mode
ω	Optical angular frequency
V_g	Group velocity
τ_{01}	Mode group delay of LP_{01} mode
τ_{11}	Mode group delay of LP_{11} mode
$\Delta\omega$	Optical angular frequency variation

$\Delta\phi_{11}$	Initial phase difference between LP_{01} and LP_{11} mode
$\Delta\tau_{11}$	DMGD between LP_{01} mode and LP_{11} mode
M	Number of modes supported in FMF
$C_{p,q}$	Coupling coefficient between mode p and mode q
B	Coefficient of optical indicatrix
σ	Tensor
p_{ij}	Component in stress-optical tensor
r	Radial distance
θ	Torsion angle
δn	RI change
$\delta\theta$	Torsion range change
F_c	Cut-off frequency
λ	Wavelength
P	Core pitch size in TCF
n_s	RI of symmetric mode
n_a	RI of antisymmetric mode
C	Curvature
J	Jitter level

List of Figures

List of Tables

Publications

The publications during my Ph.D. study, which contribute to this thesis, are given below.

Journal articles

1. ***F. Tan***, Z. Liu, J. Tu, C. Yu, C. Lu, and H. Y. Tam, “Torsion sensor based on inter-core mode coupling in seven-core fiber,” Opt. Express, 26(16), 19835-19844 (2018).
2. ***F. Tan***, S. Chen, W. Lyu, Z. Liu, C. Yu, C. Lu, and H. Y. Tam, “Non-invasive human vital signs monitoring based on twin-core optical fiber sensors,” Biomed. Opt. Express, 10(11), 5611-5624 (2019).
3. ***F. Tan***, W. Lyu, S. Chen, Z. Liu, and C. Yu, “Contactless vital signs monitoring based on few-mode and multi-core fibers,” (Accepted by Opto-Electronic Advances). **(Invited review)**
4. ***F. Tan***, S. Chen, W. Lyu, Z. Huang, T. Yang, C. Yu, C. Lu, and H. Y. Tam, “Optical fiber interferometer-based remote activities monitoring system for Alzheimer’s disease and related dementia caregiving,” (Submitted to Biomedical Optics Express).
5. J. Huo, X. Zhou, K. Zhong, T. Gui, ***F. Tan***, J. Tu, J. Yuan, H. Zhang, K. Long, C. Yu, A. P. T. Lau, and C. Lu, “100-Gb/s 80-km transmission of PIM-SSB-OFDM at C-band using a single-end photodetector,” Opt. Engineering, 56(10), 106116 (2017).

Conference papers

6. ***F. Tan***, Z. Liu, J. Tu, C. Yu, C. Lu, and H. Y. Tam, “Stable Torsion Sensor with Tunable Sensitivity and Rotation Direction Discrimination Based on a tapered Trench-Assisted Multi Core Fiber,” in *Optical Fiber Communication*

Conference 2018, paper W1K.6, San Diego, California United States, 11-15 March, 2018.

7. ***F. Tan***, Z. Liu, S. Chen, C. Yu, "Vital signs monitoring using twin core fiber-based sensor," in *Opto-Electronics and Communications Conference (OECC) 2019*, Paper WC3-2, pp.1-3, Fukuoka, Japan, July 7-11, 2019.
8. ***F. Tan***, C. Yu, J. Zhao, and G. Li, "Accurate measurement of total mode coupling in few mode fibers (FMFs) based on a modified spatial and spectral resolved (S^2) imaging system," in *Opto-Electronics and Communications Conference (OECC) 2017*, pp. 1-2, Singapore, July 31- Aug 4, 2017.
9. C. Yu, ***F. Tan***, Z. Liu, S. Chen, and Z. Huang, "Application of seven core fiber-based sensor on torsion angle measurement and vital signs monitoring," in *21th International Conference on Transparent Optical Networks (ICTON) 2019*, Paper We.E1.1, pp. 1-4, Angers, France, July 9-13, 2019. **(Invited)**
10. W. Lyu, ***F. Tan***, S. Chen, and C. Yu, "Myocardial Contractility Assessment using Fiber Optic Sensors," in *Asia Communications and Photonics Conference (ACPC) 2019*, pp. M4A, Chengdu, China, November 2-5, 2019.
11. S. Dong, ***F. Tan***, B. Dong, C. Yu, and Y. Guo, "High sensitivity curvature sensor based on seven core fiber," in *Opto-Electronics and Communications Conference (OECC) 2019*, Paper TuC1-4, pp.1-3, Fukuoka, Japan, July 7-11, 2019.
12. S. Dong, ***F. Tan***, B. Dong, C. Yu, and Y. Guo, "Simultaneous measurement of curvature and temperature based on seven core fiber cascaded with fiber Bragg grating," in *International Multidisciplinary Conference on Optofluidics (IMCO) 2019*, Hong Kong, China, June 14-17, 2019.
13. S. Chen, ***F. Tan***, Z. Huang, T. Yang, J. Tu, and C. Yu, "Non-invasive smart monitoring system based on multi-core fiber optics interferometers," in *Asia*

Communications and Photonics Conference (ACP) 2018, pp.1-3, Hangzhou, China, October 26-29, 2018. **(Best Poster Award)**

14. S. Chen, Z. Huang, ***F. Tan***, T. Yang, J. Tu, and C. Yu, "Vital signs monitoring using few-mode fiber-based sensors," in *Photonics Asia 2018*, Beijing, China, October 11-13, 2018.
15. J. Qu, Y. Shen, W. Xu, ***F. Tan***, C. Yu, and C. C. Yu, "Non-invasive Vital Signs Monitoring Based on Polarization Maintaining Fiber and Sagnac Interferometer," in *Opto-Electronics and Communications Conference (OECC) 2019*, Fukuoka, Paper WC3-3, pp.1-3, Japan, July 7-11, 2019.
16. Q. Zeng, W. Xu, Y. Shen, C. Yu, and ***F. Tan***, "Investigation on fiber-optic curvature sensor based on SMF-FMF-SMF structure with up-taper fusion," in *International Conference on Optical Communications and Networks (ICOCN) 2018*, Zhuhai, China, November 16-19, 2018.
17. J. Huo, X. Zhou, K. Zhong, T. Gui, ***F. Tan***, X. Huang, J. Tu, J. Yuan, H. Zhang, F. Li, K. Long, C. Yu, Alan P. T. Lau, and C. Lu, "PDM-SSB-OFDM Transmission Over 80km SSMF Based On A Single Photodetector At C-band," in *Opto-Electronics and Communications Conference (OECC) 2017*, Singapore, July 31- Aug 4, 2017.

1 Introduction

In this chapter, few-mode fiber and multi-core fiber in the spatial-division multiplexing system are introduced firstly. Subsequently, few-mode fiber and multi-core fiber applications, including optical fiber communication systems and sensing communities, are reviewed. Then, the research objectives and organization of the thesis are given.

1.1 Overview

Optical fiber communication, acting as the backbone for telecommunications infrastructure, has been drawing extensive attention to both research and industry areas. As the transmission media, optical fiber plays a key role in the transmission system due to its excellent advantages of wide bandwidth, low loss, lightweight, low cost and electromagnetic interference immunity. Optical fiber was firstly invented by K. C. Kao in 1966, and he proposed that "a dielectric fiber with a refractive index higher than its surrounding region is a form of dielectric waveguide which represents a possible medium for the guided transmission of energy at optical frequencies" [1]. Since then, optical fibers were widely investigated and single-mode fiber (SMF) was then fabricated for practical communication system. The schematic diagram of standard SMF is shown in Fig. 1.1. The material of cladding is silica while the core is silica with Ge doped. The refractive index of core is higher than that of cladding to confine the light propagating within the core region according to the basic principle of total reflection. Generally, the diameter of core and cladding of standard SMF are 8 μm and 125 μm, respectively. Other than standard SMF, many specialty optical fibers were designed as well as fabricated according to different requirements, such as ultra-low loss SMF, dispersion compensating fibers and polarization-maintaining fibers [2].

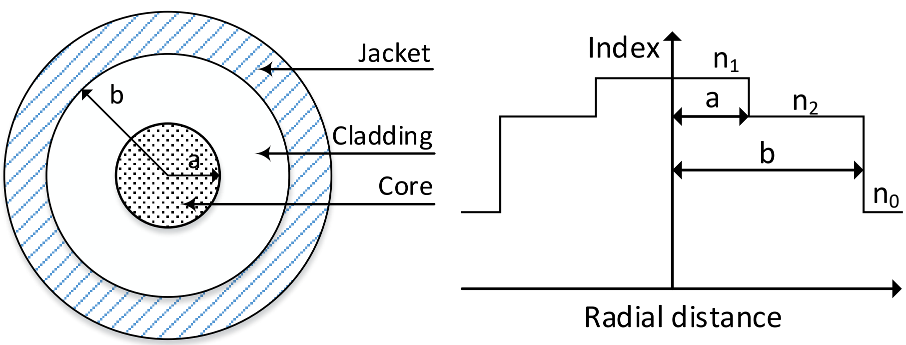

Fig. 1.1: Schematic diagram of standard SMF.

In the optical fiber communication system, high capacity has always been a major concern, and many technologies were developed to increase the transmission capacity to cope with the internet traffic growth in the past few decades, such as the wavelength division multiplexing (WDM), advanced modulation formats and the coherent receiver. In recent years, another kind of technology named space-division multiplexing (SDM) was proposed aiming to bring exponential capacity growth in optical fiber communication system. Similar to WDM system employing wavelength degree of freedom (DOF), SDM utilizes the space DOF in optical fibers, such as modes and cores, to explore additional channels for independent information transmission. Thus, the specialty optical fibers with more than one mode or one core supported in a single optical fiber are explored, which are called few-mode fiber (FMF) and multi-core fiber (MCF) [3].

1.2 Few-mode fiber and multi-core fiber

FMF, with more than one mode propagating in a single optical fiber, plays a vital role in SDM system. According to the fundamental mode theory in optical fibers, with reasonable parameters design and optimization, a few modes, including fundamental mode and high-order modes, can be supported [4]. There are many kinds of schemes proposed to achieve FMF design, such as elliptical core [5] and trench structure around the core [6]. Among them, the most straightforward way is to increase and control the core diameter. With the enlarged core, SMF can evolve to FMF or even multi-mode fiber (MMF) with a larger core diameter, which are illustrated in Fig. 1.2. Another optical fiber employed in the SDM system is MCF. With additional cores positioned away from the center core, MCF can realize multi-channel information transmission. Various MCFs were proposed with different layouts, such as three-core fiber in triangular form [7] and seven-core fiber in hexagonal from [8]. One of the most important issues in MCF is the coupling between the cores, which may degrade the transmission performance. Thus, there are also some schemes proposed to achieve weak coupling, like trench-assisted MCF [9] and heterogeneous MCF [9]. Besides, few-mode multi-core fiber (FM-MCF) with a few enlarged cores in a single optical fiber is also designed for SDM transmission, which is shown in Fig. 1.2.

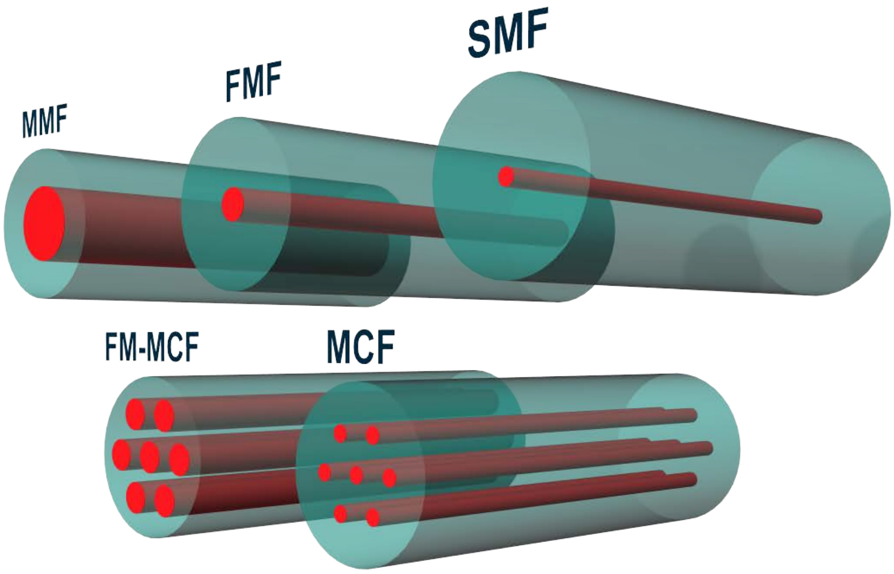

Fig. 1.2: Specialty optical fibers for SDM transmission system.

1.3 Applications of FMF and MCF

As introduced above, FMF and MCF are proposed for the high-capacity optical fiber communication system. Up to now, the SDM communication system has been explored widely, and ultra-high capacity transmission using both FMF and MCF has been realized. For example, a recent SDM system employing 19 core with 114 spatial modes can achieve the capacity as high as 10.16-Peta-B/s [10]. Other than the communication system, FMF and MCF are also utilized in sensing communities. Many kinds of structures are designed based on FMF and MCF for optical fiber sensing, and excellent performance are achieved. For FMF, mode interference can be utilized to measure temperature and strain [5] while mode coupling in MCF is applied for vibration and torsion sensing [11,12]. Apart from these single-point sensors, distributed optical fiber sensing system employing FMF and MCF also shows excellent performance, including simultaneous temperature and strain sensing in MCF-based Brillouin distributed sensing system and improved sensing performance using FMF in Raman distributed sensing system [13,14]. A conventional FMF-based distributed sensing system is shown as Fig. 1.3 [15].

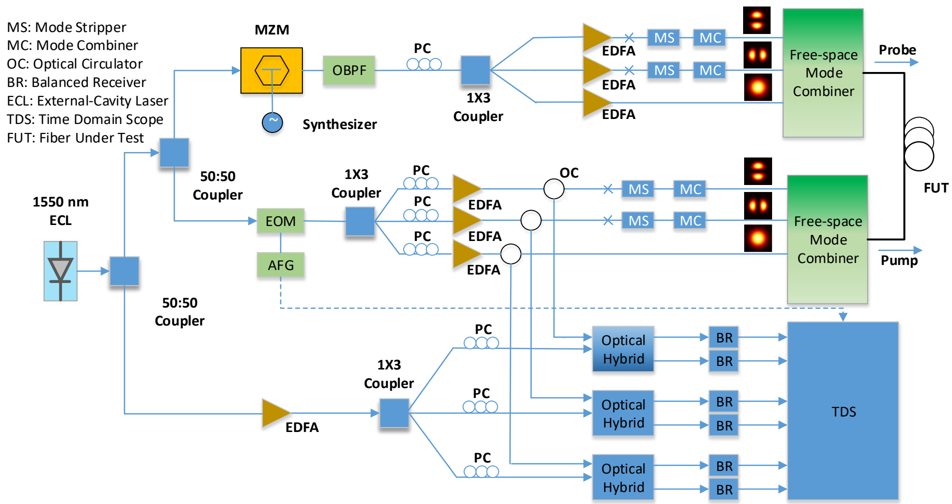

Fig. 1.3: Conventional FMF-based distributed sensing system.

1.4 Research Objectives

Research objectives in this thesis are to investigate FMF and MCF, including mode interference and mode coupling, and further explore their sensing applications. The thesis explores the following research directions:

- Investigation on mode properties in FMF and corresponding techniques to measure them, and mode interference in FMF for sensing, such as novel structures design like miniatured modal interferometers and other potential applications, such as vital signs monitoring.
- Exploration of core-mode coupling in MCF and sensing applications for

parameter measurement. Since MCF exhibited excellent performance in previous sensing systems, the interaction between cores can be further investigated and more parameters in both conventional and novel applications can be measured.

1.5 Organization of the thesis

This thesis is composed of seven chapters. Chapter 1 gives a brief introduction of FMF and MCF in the SDM system and then reviews their typical applications on the communication and sensing area. Then, research objectives, as well as organization of thesis, are given.

Chapter 2 introduces the FMF and presents its mode calculation in detail. Based on FMF parameters, the characterization function of every mode is obtained, and mode profiles are simulated. For sensing applications of FMF, miniatured modal interferometer in SMF with dual-taper structure is introduced firstly, and temperature sensing experiment is conducted. The same structure is fabricated on FMF and the mode interference is analyzed. Then, in chapter 3, an FMF mode characterization method is introduced. This technique can measure mode properties such as mode dispersion and intensity as well as phase distribution of modes. Other than that, mode coupling, including discrete and distributed mode coupling, can also be measured. Based on this system, an advanced algorithm is introduced for detailed interference mode pairs classification.

In chapter 4, a novel torsion sensor using MCF is described. The structure is based on the tapered seven-core fiber, which is fabricated with an optimized dimension. The wavelength shift results are collected under different torsion angles, and the sensitivities are also discussed in detail. Then, the capability for rotation direction discrimination is discussed while repeated experiments are conducted to discuss the stability performance. Mode coupling dynamics and optical anisotropy theory are introduced for sensitivity performance analysis of the torsion sensor.

Chapter 5 presents the application of MCF and FMF sensors on non-invasive vital signs monitoring, including respiration and heartbeat. Twin-core fiber based sensor for vital signs monitoring is introduced firstly. The sensor structure, experimental setup and vital signs monitoring results are presented, and supermode interference within twin-core fiber is employed for curvature sensing experiment. Then, in-line optical fiber interferometers using SCF and FMF for vital signs monitoring are introduced.

Healthcare applications of optical fiber sensors are further explored in chapter 6. Firstly, traditional optical fiber Mach-Zehnder Interferometer (MZI) for remote activities monitoring for Alzheimer's disease and related dementia caregiving is introduced, including the optical fiber sensor layout, circuit fabrication and Wi-Fi network deployment. Other than that, application of optical fiber MZI on myocardial contractility assessment is also described.

In the end, chapter 7 gives a summary of the work in this thesis and also suggests future research directions based on current systems and results.

2 FMF and its sensing application

In this chapter, the SDM technique and FMF are first introduced. Then, mode calculation regarding FMF is presented in detail and the distribution of supported modes is obtained. For the sensing application, a miniatured modal interferometer using FMF with a taper structure is investigated, and its temperature sensing performance is discussed.

2.1 Overview of FMF

Optical fiber communication, as the dominate information transmission system in modern society, has always been investigated to improve performance further to meet different demands, one of which is the transmission capacity. In the past few decades, many kinds of techniques were developed successively to cope with the pressure of internet traffic on the capacity of optical fiber transmission system. These technologies included improved transmission optical fibers, Erbium doped optical fiber amplifier (EDFA), wavelength division multiplexing and high spectral efficiency coding techniques, as shown in Fig. 2.1. In principle, the improvement of capacity mainly depends on the employment of different DOFs of light, such as intensity, phase, time, wavelength and polarization. To cope with the current information crisis on capacity, new DOF needs to be employed and investigated. Space, including cores and modes in optical fibers, is the only DOF which has not been employed. Current optical fibers employed in the optical fiber communication system are SMFs with only fundamental mode and one core supported in a single optical fiber. Space of DOF can be further explored to multiplex more than one mode and one core as transmission channels in order to achieve capacity growth in an exponential way. Thus, a new kind of technique named SDM becomes the solution, and many research work are devoted on the development of this novel technology. These research work includes the specialty optical fiber design and fabrication [4] to employ the space of DOF in a single optical fiber, multiplexing and de-multiplexing techniques and devices to convert and combine the modes or cores together [16], advanced algorithms to deal with the signal crosstalk due to mode coupling in optical fibers and transmitter as well as receiver design [17].

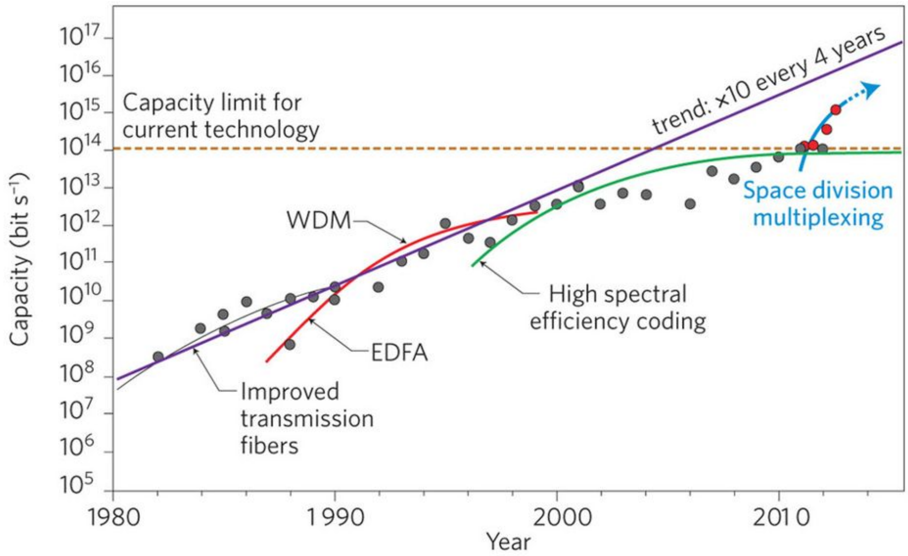

Fig. 2.1: The evolution of transmission capacity in optical fiber communication system and the corresponding technologies [15].

In 2009, "3M technology" was proposed for the SDM system: core multiplexing using MCFs, which used different cores as the independent channels; mode-division multiplexing with individual mode employed in FMFs; hybrid approach using FM-MCFs [18]. Optical fibers used in the SDM system are summarized in Fig. 2.2 [19,20]. Among these three schemes, mode-division multiplexing (MDM) technique is the most popular one in the research area to explore properties of different modes. The optical fiber in the MDM system is FMF, which supports more than one mode in a single optical fiber, including fundamental mode and high-order modes. These modes are orthogonal to each other, which can be utilized as independent transmission channels to improve capacity exponentially [21]. Mode multiplexer and de-multiplexer and FMF assemble an MDM system as shown in Fig. 2.3.

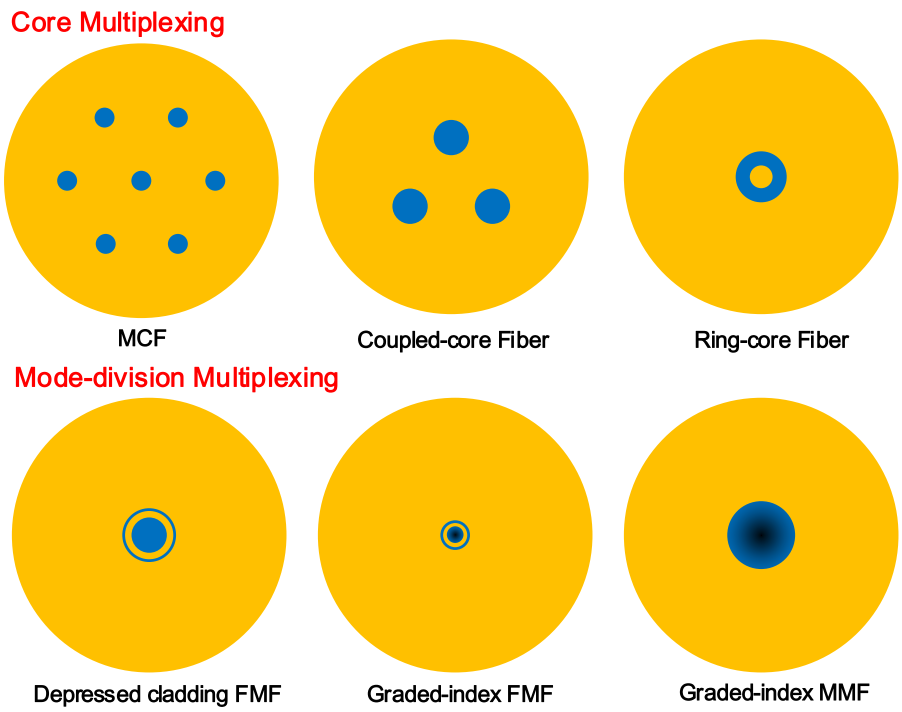

Fig. 2.2: Different kinds of optical fibers proposed for the SDM system.

To increase the number of modes in FMF, the most straightforward way is enlarging the core in terms of diameter. With increased core diameter, the V number, which will be discussed in the next section, will increase and then high-order modes appear. For example, as shown in Fig. 2.4, only fundamental mode is supported in optical fiber under the condition of V lower than 2.405. When the value of V exceeds 2.405 under increased core diameter, high-order mode becomes supported except for fundamental mode.

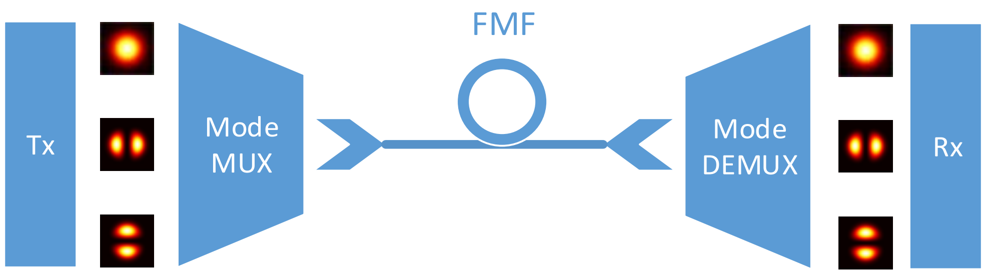

Fig. 2.3: Mode-division multiplexing (MDM) system.

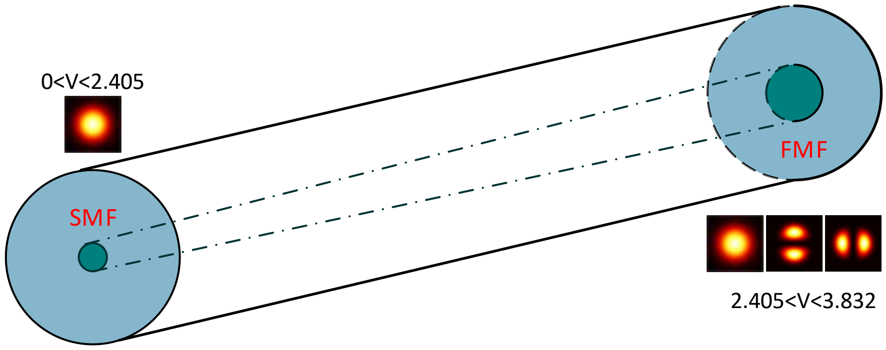

Fig. 2.4: Schematic diagram of evolution from SMF to FMF with diameter of core increases.

2.2 FMF parameters

As introduced above, with enlarged core in the optical fiber, high-order modes will appear, and SMF will evolve to FMF. Except for the core diameter, there are other parameters in FMF, which will be introduced as follows [2].

(1) Geometrical parameters

The schematic diagram of optical fiber is shown as Fig. 2.5, in which the diameter of core and cladding are the geometrical parameters. n_{core} and $n_{cladding}$ are the refractive index (RI) of core and cladding, respectively. To confine the light propagating in the optical fiber, the value of n_{core} will be a little larger than that of $n_{cladding}$ to meet the total reflection principle.

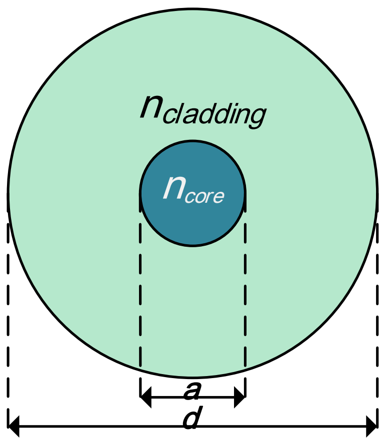

Fig. 2.5: Schematic diagram of optical fiber.

(2) Numerical aperture

Numerical aperture (NA) is another parameter related to n_{core} and $n_{cladding}$, which can be expressed as Eq. (2.1). NA is used to characterize the capability of light collection of optical fiber, which is very useful in optical fiber imaging applications.

$$NA = \sqrt{n_{core}^2 - n_{cladding}^2} \tag{2.1}$$

(3) Relative refractive index difference

Relative refractive index (RI) difference of optical fiber can be expressed as follows:

$$\Delta = \frac{n_{core}^2 - n_{cladding}^2}{2n_{core}^2} \approx \frac{n_{core} - n_{cladding}}{n_{core}}. \tag{2.2}$$

Generally, the value of relative RI difference is around 0.001.

(4) Normalized frequency

Normalized frequency is used to calculate the number of modes supported in optical fiber and also the modal electrical field distribution. It is expressed as follow:

$$V = \frac{\pi a}{\lambda} NA, \tag{2.3}$$

in which the normalized frequency V is related to core diameter, NA and operation wavelength. It can be concluded that under different operation wavelength, the optical fiber can operate on the state of single-mode or few-mode.

(5) Effective refractive index

For every mode supported in optical fiber, the effective RI can be used to analyze modal properties, such as modal dispersion and modal electrical field distribution. The effective RI can be expressed as follows:

$$n_{eff} = \frac{\beta}{k_0}, \tag{2.4}$$

in which β is the propagation constant and k_0 is the wave number in vacuum.

(6) Normalized transverse phase and attenuation parameters

The normalized transverse phase parameter U and attenuation parameter W are used to calculate modal electrical field distribution in transverse plane and the attenuation property of modes in cladding region, respectively. They can be expressed as Eq. (2.5) and Eq. (2.6).

$$U = \frac{a}{2}\sqrt{k_0^2 n_{core}^2 - \beta^2} \tag{2.5}$$

$$W = \frac{a}{2}\sqrt{\beta^2 - k_0^2 n_{cladding}^2} \tag{2.6}$$

Based on Eq. (2.3), U, W and V follow the relationship:

$$V^2 = U^2 + W^2, \tag{2.7}$$

in which the U and W are used for later mode calculation in FMF.

2.3 Mode calculation in FMF

The mode calculation in FMF originates from the solution of Maxwell equation under the boundary condition in optical fiber. Since optical fiber follows the circular waveguide, it is appropriate to perform the calculation in cylindrical coordinate system [22]. (E_r, E_φ, E_z) and (H_r, H_φ, H_z) represent the electric and magnetic field in optical fiber respectively in radial, angular and axial direction. In this chapter, only electric field in optical fiber is analyzed. Based on Maxwell equation, E_z meets the Helmholtz equation as follows:

$$\nabla^2 E_z + k_0^2 n^2 E_z = 0, \tag{2.8}$$

where k_0 is the wave number in vacuum, n is the RI of waveguide, namely core and cladding in optical fiber. Under cylindrical coordinate system, Eq. (2.8) can be expressed further as follows:

$$\frac{\partial^2 E_z}{\partial r^2} + \frac{1}{r}\frac{\partial E_z}{\partial r} + \frac{1}{r^2}\frac{\partial^2 E_z}{\partial \varphi^2} + \frac{\partial^2 E_z}{\partial z^2} + k_0^2 n^2 E_z = 0, \tag{2.9}$$

where r, φ and z represent radial, angular and axial direction. According to different RI of core and cladding in optical fiber, Eq. (2.9) can be solved with different conditions and different mode solutions will be obtained consequently, which will be discussed later. Basically, for electric field in optical fiber, E_z can be represented as follows:

$$E_z = R(r)\Phi(\varphi)Z(z), \tag{2.10}$$

where R, Φ and Z are the radial, angular and axial component of electric field in optical fiber. Angular and axial component, Φ and Z, can be expressed as follows:

$$\begin{aligned} Z(z) &= e^{-i\beta z} \\ \Phi(\varphi) &= \begin{bmatrix} \sin(l\varphi) \\ \cos(l\varphi) \end{bmatrix}, \end{aligned} \tag{2.11}$$

where β is the propagation constant. This follows the traditional analysis of light in cylindrical waveguide. According to radial component R, the equation needs to be separated into two equations due to the RI difference in core and cladding. As a result, the radial component R can be expressed as follows:

$$\begin{aligned} &\frac{d^2R(r)}{dr^2} + \frac{1}{r}\frac{dR(r)}{dr} + [(k_0^2 n_{core}^2 - \beta^2) - \frac{m^2}{r^2}]R(r) = 0, r \le \frac{a}{2} \\ &\frac{d^2R(r)}{dr^2} + \frac{1}{r}\frac{dR(r)}{dr} + [(k_0^2 n_{cladding}^2 - \beta^2) - \frac{m^2}{r^2}]R(r) = 0, r \ge \frac{a}{2} \end{aligned}, \tag{2.12}$$

where m is the number of periods of electric field in angular direction. Eq. (2.12) is the standard Bessel equation.

For the electric field in core region in optical fiber, the solution of Eq. (2.12) is the first Bessel function $J_l(r)$. The curve of first Bessel function group $J_l(r)$ is shown in Fig. 2.6. It can be seen that, according different order l, the Bessel function can be in different shape, which represents different modal distribution in radial direction in optical fiber.

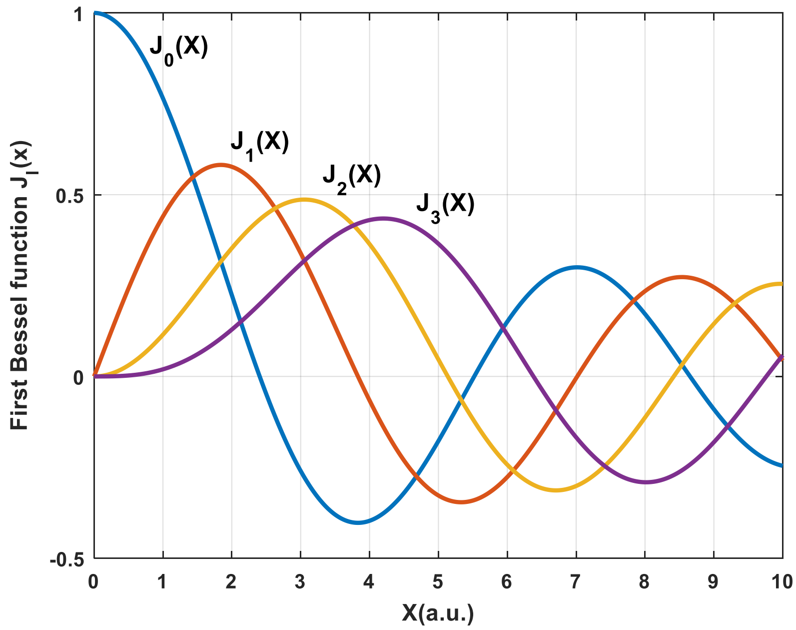

Fig. 2.6: First Bessel function in different orders.

In cladding region in optical fiber, the solution of Eq. (2.12) is second Bessel function $K_l(r)$. The corresponding curve of $K_l(r)$ is shown in Fig. 2.7. It can been seen that, the amplitude of radial component in electric field decreases away from core, which accords with the light propagation property in cladding area.

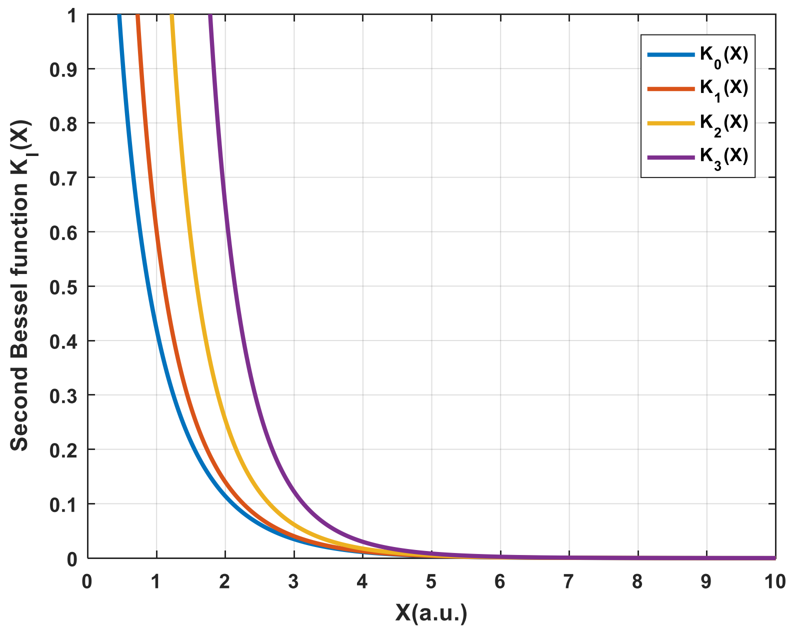

Fig. 2.7: Second Bessel function in different orders.

Based on Eq. (2.12) and analysis above on Bessel function, the radial component R of electric field in optical fiber can be updated as follows:

$$\begin{aligned} R_{core}(r) &= A_1 J_l(UR_a), R_a \le 1 \\ R_{cladding}(r) &= A_2 K_l(WR_a), R_a \ge 1 \end{aligned}, \tag{2.13}$$

where R_a is equal to 2r/a. According to the boundary condition in optical fiber, combined with angular and axial components: Φ and Z aforementioned, the electric field E_z in both core and cladding region can be eventually expressed as follows:

$$\begin{aligned} E_{z\_core} &= A\frac{J_l(UR_a)}{J_l(U)}\sin(l\varphi)e^{-i\beta z}, R_a \le 1 \\ E_{z\_cladding} &= A\frac{K_l(WR_a)}{K_l(W)}\sin(l\varphi)e^{-i\beta z}, R_a \ge 1 \end{aligned}, \tag{2.14}$$

where $A=A_1J_l(U)=A_2K_l(W)$. In Eq. (2.14), only $sin(l\varphi)$ component in angular direction is given for simple analysis and $cos(l\varphi)$ can be another solution.

To obtain the mode parameters, such as effective RI and electric field distribution, from Eq. (2.4), the U and W are under solved. U and W can be obtained from the characteristic equations, which can be deduced based on the boundary condition in optical fiber: the tangential components of both electric and magnetic field are continuous in the boundary between core and cladding. It is worth noted that, the calculation is based on the assumption that RI of core and cladding are very close to each other, $n_{core} \approx n_{cladding}$, in other words, which is called weak waveguide approximation. Finally, the characteristic equation can be expressed as follows:

$$\frac{J_l'(U)}{UJ_l(U)} + \frac{K_l'(W)}{WK_l(W)} = \pm l(\frac{1}{U^2} + \frac{1}{W^2}), \tag{2.15}$$

where two sets of solution can be obtained with positive and negative right part.

Based on Eq. (2.15), the modes supported in optical fiber can be categorized with different number of order l. Mode classification using Eq. (2.15) is investigated under linear polarization (LP) mode. LP mode is proposed to simplify the mode calculation instead of using conventional vector mode analysis, such as TE and EH modes. Under the weak waveguide approximation, LP mode is composed of some degenerate vector modes, whose propagation constants are very close to each other. In this chapter, mode calculation is based on LP modes. In LP modes, based on Eq. (2.15), under certain order *l*, there can be different sequence of solution *m*. Thus, LP mode can be categorized using subscripts of *l* and *m*. Eventually, characteristic equations of LP_{lm} modes are expressed by following equations:

$$\begin{aligned} &\frac{J_0(U)}{UJ_1(U)} = \frac{K_0(W)}{WK_1(W)} \rightarrow [LP_{0m}(l=0)]; \\ &\frac{J_1(U)}{UJ_0(U)} = -\frac{K_1(W)}{WK_0(W)} \rightarrow [LP_{1m}(l=1)]; \\ &\frac{J_l(U)}{UJ_{l-1}(U)} = -\frac{K_l(W)}{WK_{l-1}(W)} \rightarrow [LP_{lm}(l \geq 2)]. \end{aligned} \tag{2.16}$$

Thus, based on Eq. (2.16) and Eq. (2.7), by a given *V* of optical fiber, *U* and *W* can be obtained. With characteristic equations, the cutoff frequency (V_c) of every mode can be calculated, the results of which are shown as follows:

$$\begin{aligned} &LP_{0m}(l=0) \rightarrow J_1(U=V_c)=0; \\ &LP_{1m}(l=1) \rightarrow J_0(U=V_c)=0; \\ &LP_{lm}(l \geq 2) \rightarrow J_{l-1}(U=V_c)=0; (NonzeroSolution) \end{aligned} \quad , \tag{2.17}$$

It can be seen that, V_c is the solution of Bessel functions with different order *l*. For example, for LP_{0m} mode, V_c are the solutions of first order Bessel function. The curve of first order Bessel function and the solution are as shown in Fig. 2.8. It can be seen that, at each position where first order Bessel function is equal to zero, the corresponding LP_{0m} mode will be cut off. In the same way, the cutoff frequency of LP_{1m} mode and LP_{3m} mode can be obtained from the solutions of the zero order Bessel function and second order Bessel function, respectively.

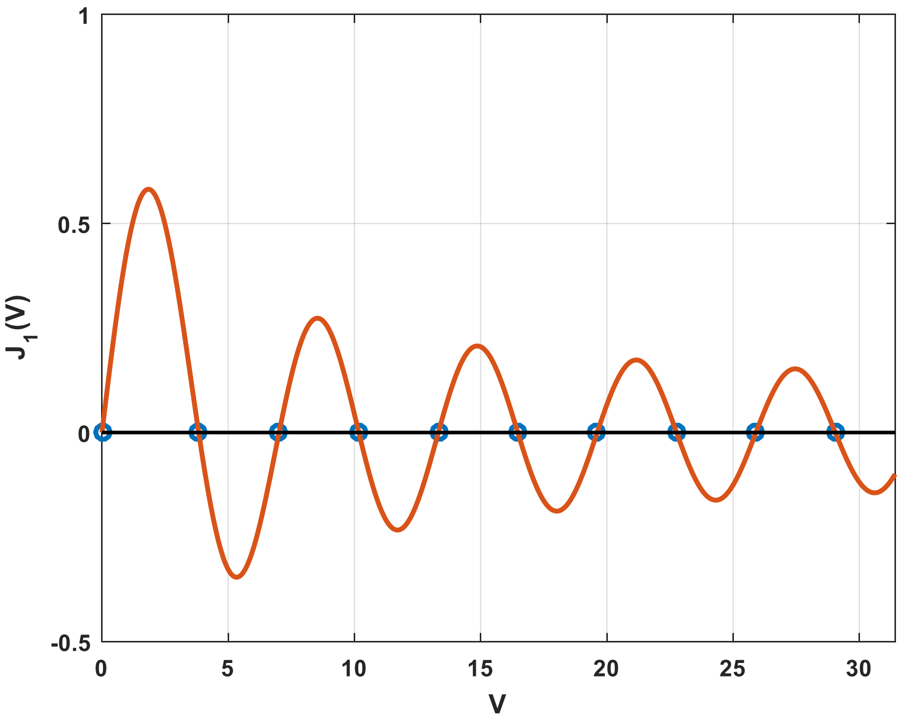

Fig. 2.8: Cutoff frequency calculation of LP_{0m} mode.

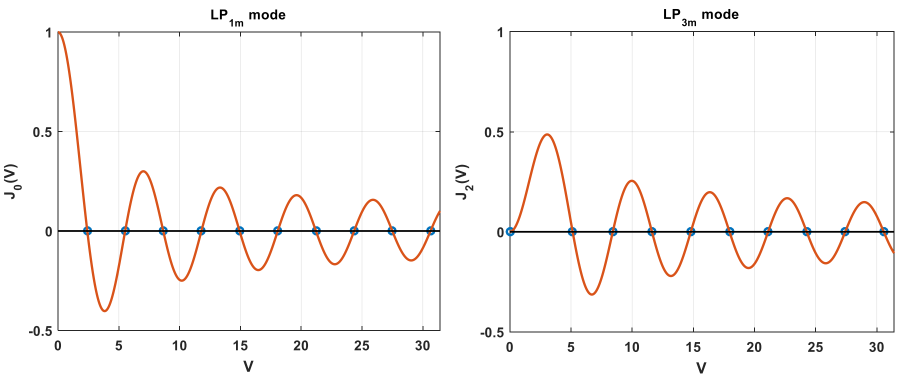

Fig. 2.9: Cutoff frequency calculation of LP_{1m} mode and LP_{3m} mode.

Thus, cutoff frequency V_c of every LP_{lm} mode can be obtained and the results are summarized in Table 2.1. For example, when the V number of optical fibers is lower than 2.4048, only LP_{01} mode is supported, which is also the working condition of SMF. Then, when it exceeds 2.4048, high-order modes appear. When V number locates within the range of (2.4048, 3.8317), LP_{01} mode and LP_{11} mode become supported.

Table 2.1 Cutoff frequency of LP_{lm} mode

V_c	$m=1$	$m=2$	$m=3$	$m=4$
$l=0$	0	3.8317	7.0156	10.1735
$l=1$	2.4048	5.5201	8.6537	11.7915
$l=2$	3.8317	7.0156	10.1735	13.3237
$l=3$	5.1356	8.4172	11.6198	14.7960

For modal electric field distribution simulation in optical fiber, in core region, the ratio between E_y and E_z, which are the amplitudes of y component and z component of electric field, can be expressed as follows:

$$\frac{|E_z|}{|E_y|} \approx \frac{\sqrt{k_0^2 n_1^2 - \beta^2}}{k_0}, \tag{2.18}$$

which indicates that the y component, same as x component in electric field in optical fiber core region, is larger than z component. For mode electric field distribution calculation, the x component is the main focus since it can be intuitively observed from experiments. Therefore, electric field in optical fiber core and cladding region can be expressed eventually by Eq. (2.19) and Eq. (2.20), respectively.

$$E_{x\_core} = AJ_l(UR_a)\begin{bmatrix}\cos(l\varphi)\\ \sin(l\varphi)\end{bmatrix}, \tag{2.19}$$

$$E_{x\_cladding} = AJ_l(U)\frac{K_l(WR_a)}{K_l(W)}\begin{bmatrix}\cos(l\varphi)\\ \sin(l\varphi)\end{bmatrix}, \tag{2.20}$$

Thus, for the optical fiber with given V number, U and W can be obtained firstly based on Eq. (2.16) and Eq. (2.7). Then, the mode electric field distribution can be obtained from Eq. (2.19) and Eq. (2.20). In this section, two kinds of FMF are simulated, including two-mode fiber (TMF) and four-mode fiber. For example, with an optical fiber with V number of 3.7, LP_{01} mode and LP_{11} mode are supported and the fiber acts as TMF. The electric field distribution and intensity field distribution of LP_{01} mode are shown in Fig. 2.10.

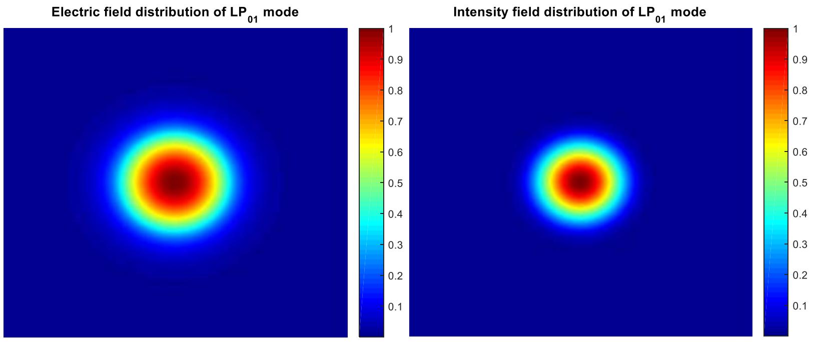

Fig. 2.10: Electric field distribution and intensity field distribution of LP_{01} mode in two mode fiber.

For LP_{11} mode, two degenerate modes are calculated, LP_{11a} and LP_{11b} mode. The field distribution of LP_{11a} mode is shown in Fig. 2.11 while LP_{11b} mode is shown in Fig. 2.12.

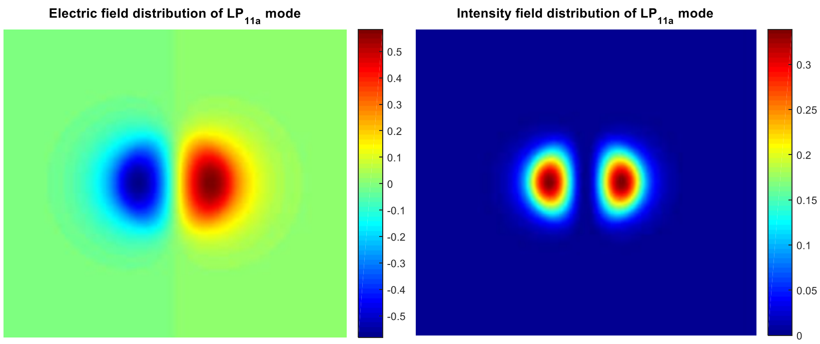

Fig. 2.11: Electric field distribution and intensity field distribution of LP_{11a} mode in two-mode fiber.

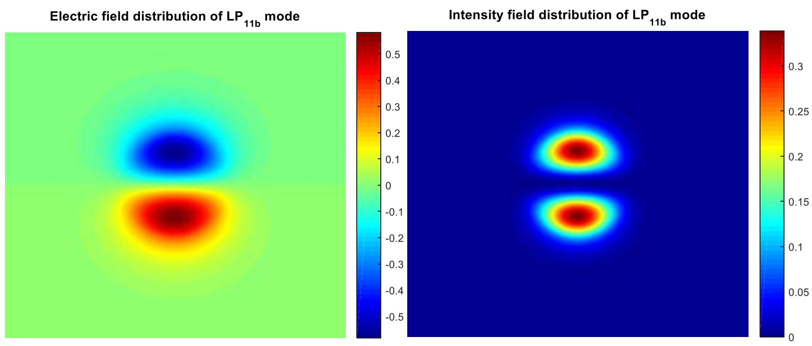

Fig. 2.12: Electric field distribution and intensity field distribution of LP_{11b} mode in two mode fiber.

For FMF with V number over 2.4048, more high-order modes become supported, such as LP_{02} mode and LP_{21} mode. According to LP_{02} mode, the mode electric field distribution function follows Eq. (2.18) and Eq. (2.19) under l of 0. The electric and intensity field distribution are shown in Fig. 2.13.

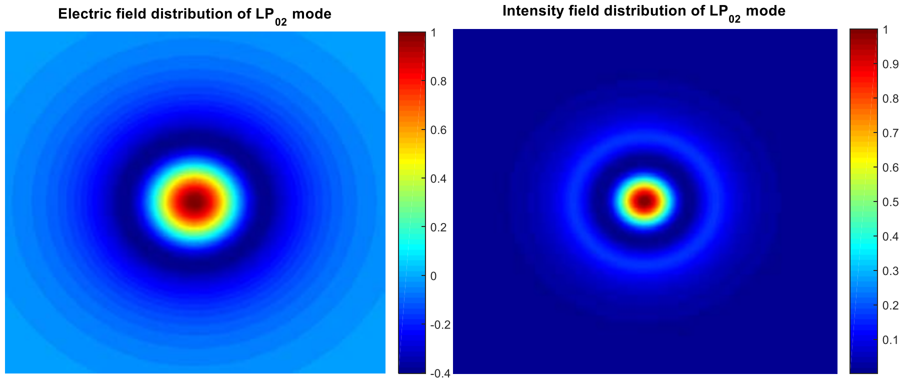

Fig. 2.13: Electric field distribution and intensity field distribution of LP_{02} mode in four-mode fiber.

Similar to LP_{11} mode, LP_{21} mode also includes two generate mode LP_{21a} and LP_{21b} mode. The mode electric field distribution function follows Eq. (2.18) and Eq. (2.19) under l of 2. The electric and intensity field distribution of LP_{21a} mode are shown in Fig. 2.14 while LP_{21b} mode are shown in Fig. 2.15.

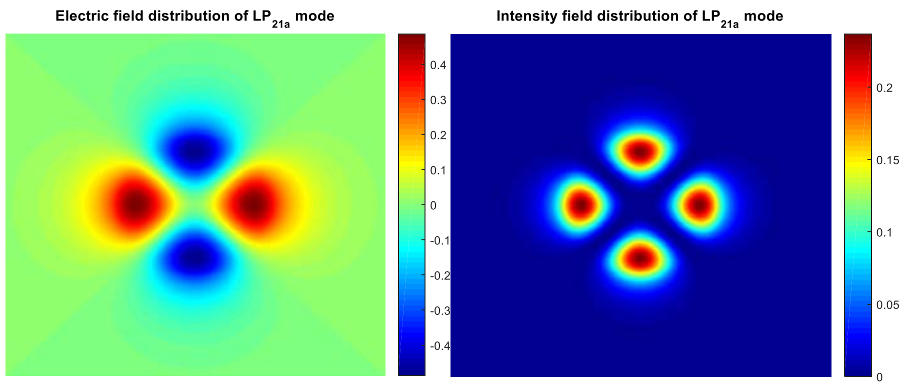

Fig. 2.14: Electric field distribution and intensity field distribution of LP_{21a} mode in four-mode fiber.

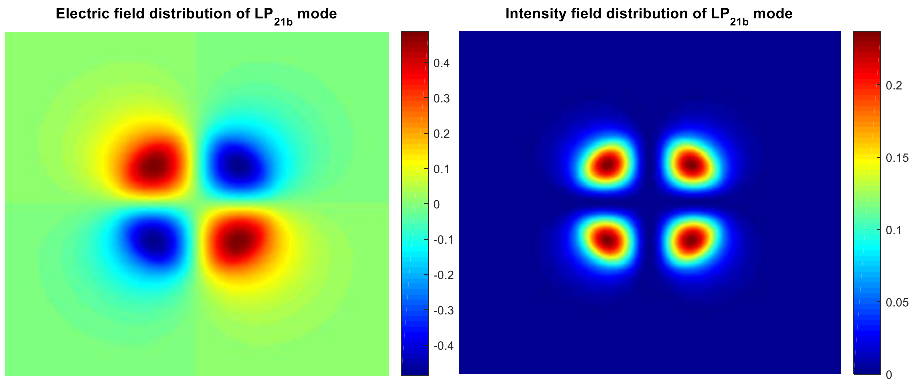

Fig. 2.15: Electric field distribution and intensity field distribution of LP_{21b} mode in four-mode fiber.

For the same mode, mode profile, including electric and intensity distribution, will be different in few mode fibers with different V number. For example, for LP_{01} mode, with different V numbers, the electric field distribution in one dimension is different, which is shown in Fig. 2.16. It can be seen that with increased V number, the mode will be more focus in the center of optical fiber.

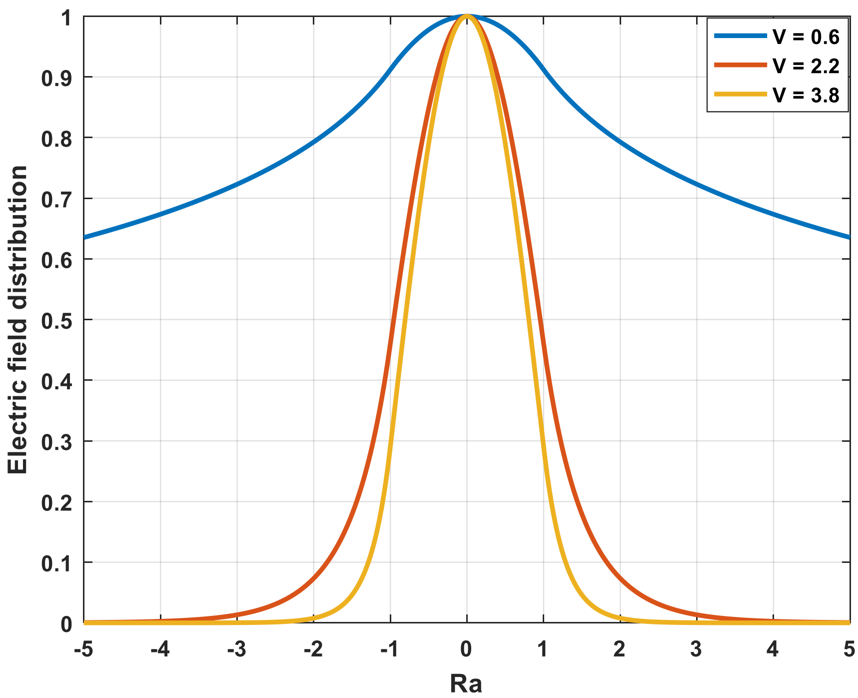

Fig. 2.16: One dimensional electric field distribution of LP_{01} mode under different values of normalized frequency V.

2.4 Miniaturized modal interferometer

Optical fiber interferometer is one kind of typical optical fiber sensors and has been widely used for temperature, strain and vibration sensing. Among different kinds of optical fiber interferometers, miniaturized modal interferometer (MMI) is proposed for compact sensor design using conventional SMF [23]. A common structure used in MMI is based on dual-taper structure on SMF. In the first taper region, cladding mode will be excited and co-propagate with core mode along the fiber, and emerge together on the second taper region, which is shown as Fig. 2.17 [24]. Due to the RI difference of cladding mode and core mode, their interference will happen, which can be utilized for parameter measurement [25]. In this section, MMI is designed and fabricated using SMF and the temperature sensing experiment is conducted to demonstrate the sensing application of MMI.

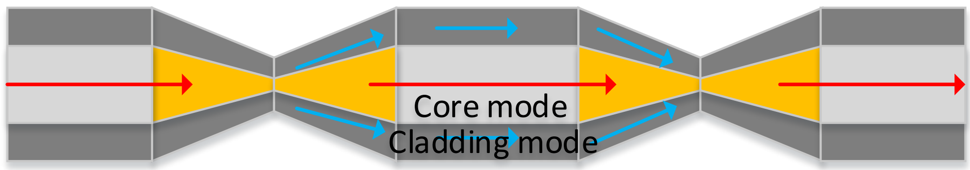

Fig. 2.17: Miniatured modal interferometer using dual-taper structure in SMF.

The taper structure is fabricated using CO_2 laser glass-processing machine (Fujikura, LZM-100), which can also realize the dimension optimization. In taper structure, waist diameter, length and transition length are the parameters under optimized. In this section, the MMI is designed and optimized in terms of transition length. The dimension of MMI is shown in Fig. 2.18, in which the fiber used is standard SMF with the cladding diameter of 125 μm. Two tapers in MMI are designed with the same waist diameter of 40 μm and waist-length of 1 mm. The length of interference path in SMF is 10 mm.

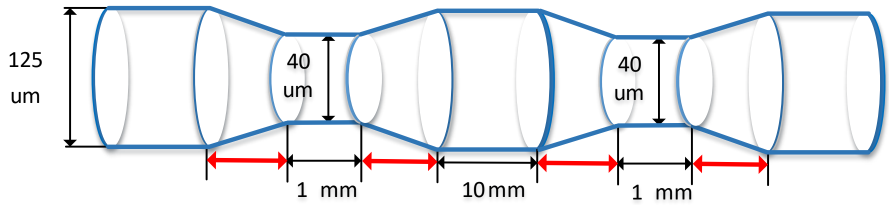

Fig. 2.18: Dimension of MMI.

To obtain a desired transition length, optical spectrum of MMI is monitored using combination of broadband light source (BLS) with spectral range from 1250 nm to 1650 nm and optical spectrum analyzer (OSA, Yokogawa AQ6370D). The transition length changes from 1 mm to 4 mm and the corresponding spectra are summarized as Fig. 2.19. It can be seen that the extinction ratio (ER) increases with transition length. ER under the transition length of 4 mm can achieve 26 dB. Thus, considering the fabrication complexity and stability, the transition length in a taper is confirmed to be 4 mm.

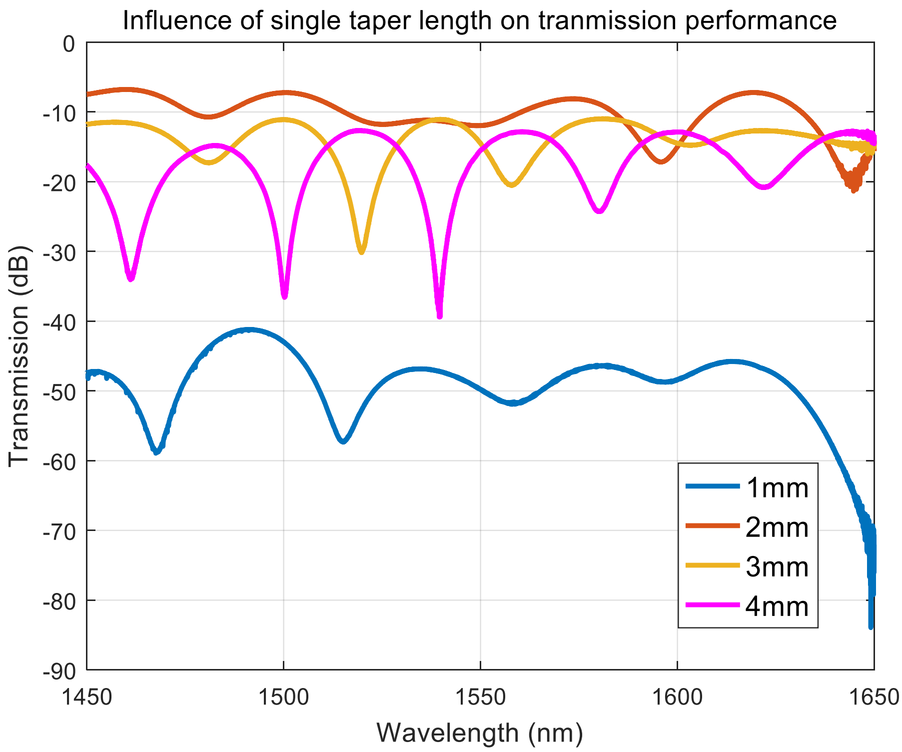

Fig. 2.19: Optical spectra under different transition lengths in taper structure.

Based on this MMI, a temperature sensing experiment is conducted. The

MMI is placed into a heating tube, where the temperature can be tuned from 80° to 200°. The optical spectrum under every temperature condition is collected. The sensing results are shown in Fig. 2.20.

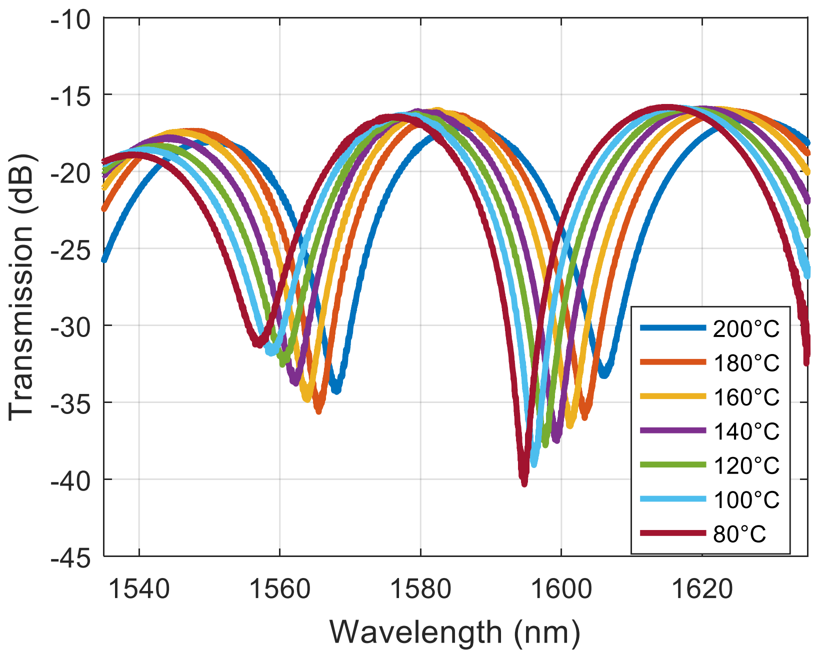

Fig. 2.20: Temperature sensing results using MMI.

It can be seen that the spectrum experiences red-shift with temperature. Then, one dip of spectrum is monitored, and the wavelength shift results are shown in Fig. 2.21. Curve fitting is applied to the results to obtain sensitivity. Finally, the sensitivity of MMI for temperature sensing can achieve 0.0946 nm/°. This kind of sensitivity is desirable among current temperature sensors.

In summary, MMI based on SMF has been demonstrated with excellent temperature sensing results. The dimension, namely transition length, is optimized to achieve high ER and the spectrum shows blue-shift with temperature and the achieved sensitivity is 0.0946 nm/°. In the next section, MMI is designed on FMF, and the sensing performance is also discussed.

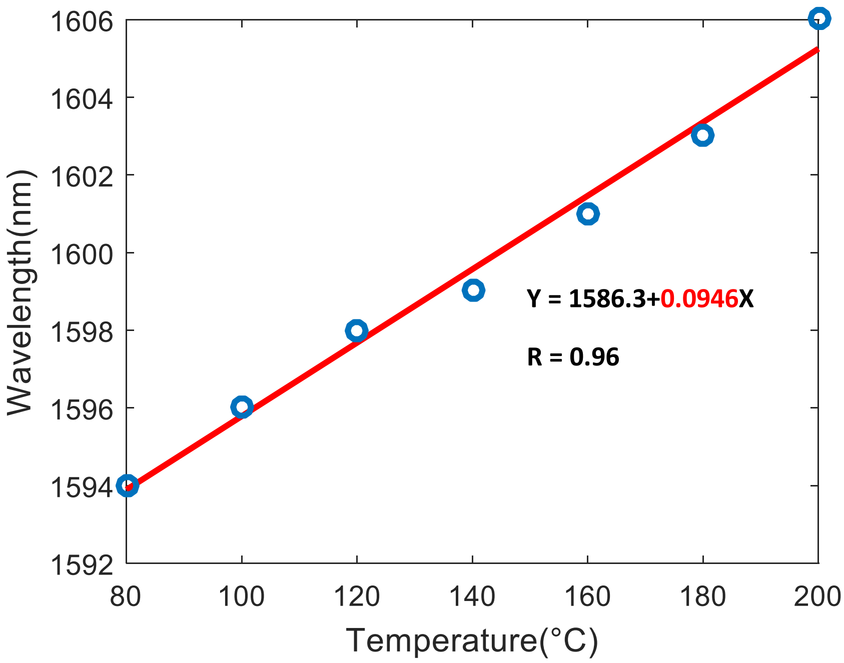

Fig. 2.21: Curve fitting results to obtain the sensitivity.

2.5 MMI based on FMF

With more than one mode supported in single optical fiber, FMF is a promising candidate for modal interferometer design. Due to the intrinsic RI difference of fundamental mode and high-order modes, the inter-mode interference will happen, which can be utilized for sensing as an FMF-based interferometer. Mode excitation in FMF is very important, and many kinds of schemes are proposed, such as offset splicing [25], long-period gratings [26]. Among these, the taper structure on FMF can also be used for mode excitation. Combined with the MMI with dual-taper structure mentioned above, MMI using FMF is fabricated. The structure still follows Fig. 2.17, and the dimension also needs optimization.

The fiber used in MMI fabrication is a TMF with LP_{01} and LP_{11} mode supported. The dimension of TMF-based MMI is shown in Fig. 2.22.

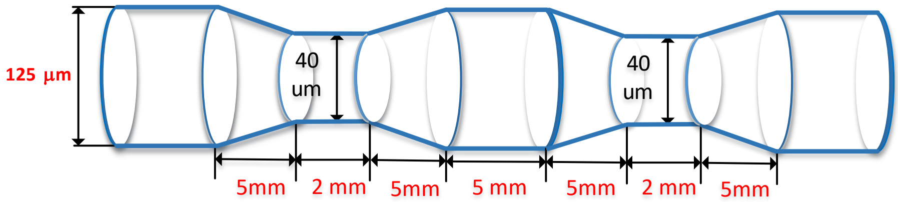

Fig. 2.22: Dimension of MMI based on TMF.

By using the same optical spectrum monitoring setup, the optical spectrum of this MMI device is shown in Fig. 2.23.

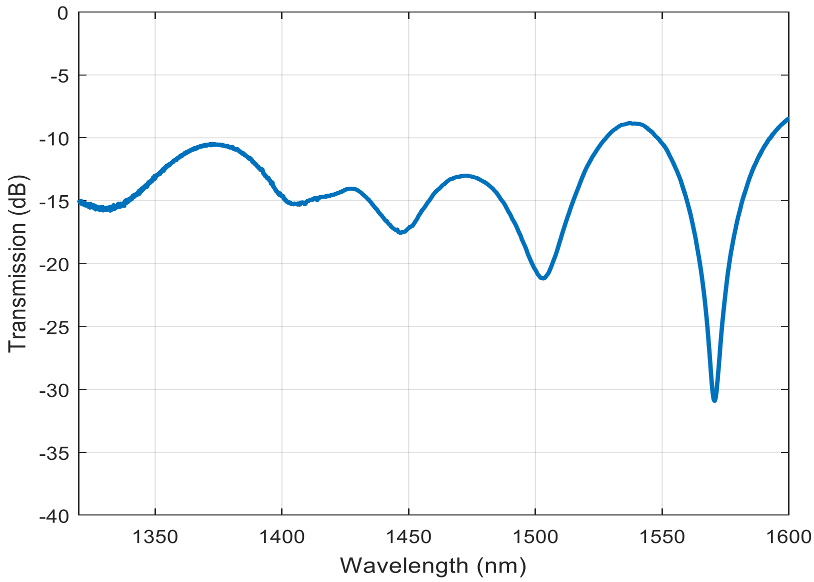

Fig. 2.23: Optical spectrum of MMI based on TMF.

Similarly, the temperature sensing experiment is conducted, and the result is shown in Fig. 2.24.

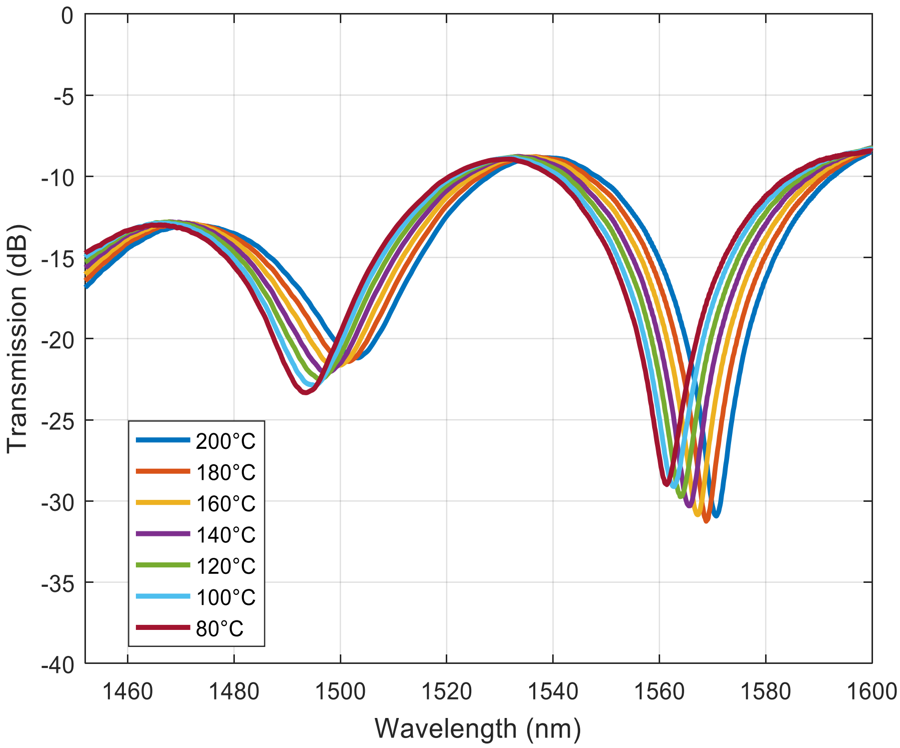

Fig. 2.24: Temperature sensing results using MMI based on TMF.

2.6 Discussion on MMI

For MMI based on SMF, in taper region, cladding mode is excited and then interferes with existed core mode along the fiber [27]. This kind of interference can be expressed as follows:

$$I = I_{core} + I_{cladding} + 2\sqrt{I_{core} I_{cladding}} \cos(\frac{\lambda}{2\pi}(n_{core} - n_{cladding})L), \tag{2.21}$$

where I_{core} and $I_{cladding}$ are the intensity of core mode and cladding mode, n_{core} and $n_{cladding}$ are the corresponding RIs. The dip wavelength can be then expressed as follows:

$$\lambda_d = \frac{2}{2k+1}(n_{core} - n_{cladding})L, k = 0,1,2..., \tag{2.22}$$

where λ_d is the dip wavelength monitored.

For MMI using TMF, since the TMF can support both LP_{01} and LP_{11} mode, in the taper region, not only cladding mode but also LP_{11} mode is excited. Thus, the interference occurs within two mode-pairs: LP_{01} mode with cladding mode and LP_{01} mode with LP_{11} mode, which can be concluded from the spatial frequency spectrum. Fourier transform is conducted on the optical spectrum in Fig. 2.23 to obtain the spatial frequency results, which are shown in Fig. 2.25. It can be seen that there are two peaks in the spatial frequency spectrum, which represent two mode-pairs.

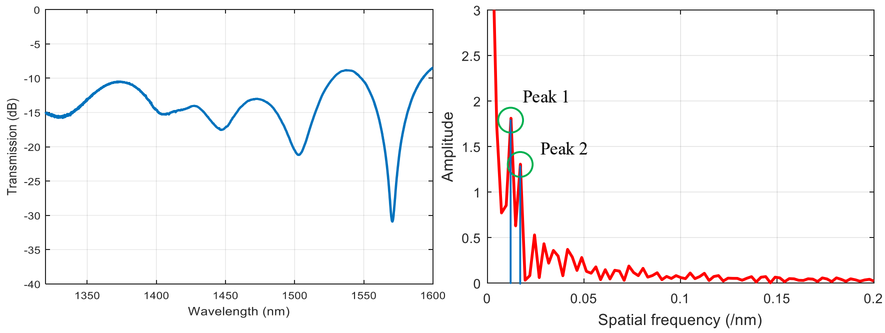

Fig. 2.25: Spatial frequency spectrum in MMI based on TMF.

Then, the temperature sensing performance can also be divided into two mode-pairs sensing results. Separated temperature sensing results are extracted from Fig. 2.24 and shown in Fig. 2.26.

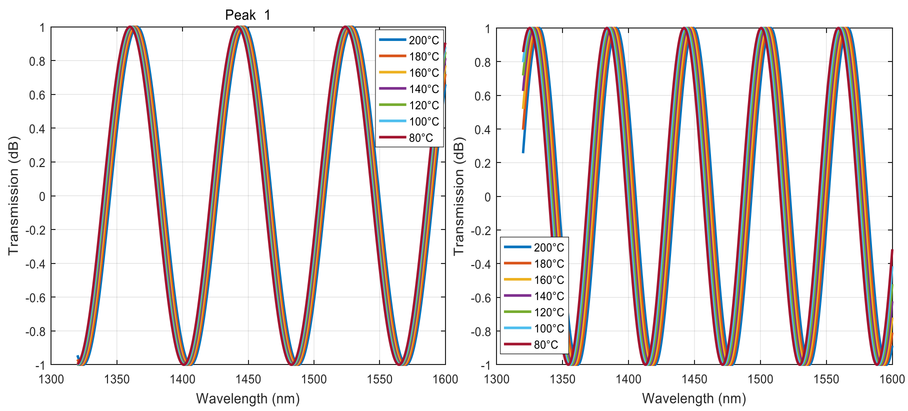

Fig. 2.26: Extracted temperature sensing results of two mode pairs.

In detail, the wavelength shift results are shown in Fig. 2.27, which represent the thermal response of two mode-pairs, or two peaks in spatial frequency spectrum.

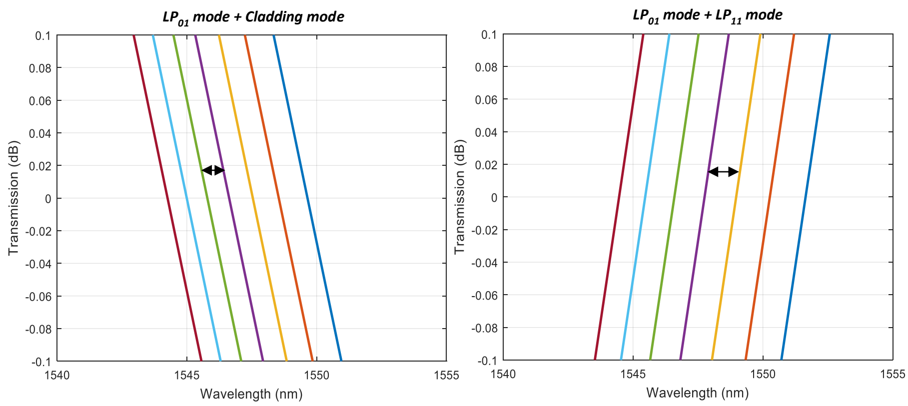

Fig. 2.27: Detailed wavelength shift results.

As a result, the sensitivity performance of two mode-pairs on temperature variation is different, as shown in Fig. 2.28. It can be seen that the temperature sensitivities of two mode-pairs are 0.050 nm/° and 0.059 nm/°, respectively.

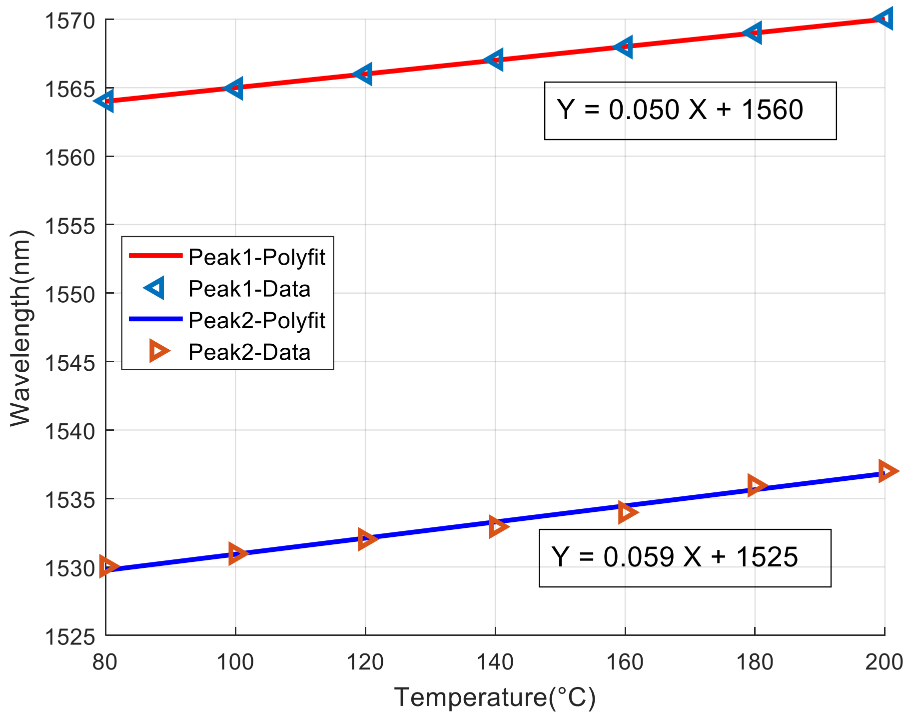

Fig. 2.28: Temperature sensitivities of two mode-pairs.

In summary, for MMI based on TMF, the interference in two mode-pairs is demonstrated, and different temperature sensing performance are obtained.

2.7 Summary

As the typical specialty optical fiber in the SDM system, FMF with the enlarged core can support more than one mode. Starting from the Maxwell equation, based on fundamental parameters in the optical fiber, mode electrical component can be obtained, which can be used for further mode simulation. The obtained characteristic equation shows that every mode has its own U and W while the cut-off frequency can also be obtained by solving a series of Bessel functions. By a given V number, every mode in FMF can be calculated and corresponding electric field distribution can be obtained, such as LP_{01} mode, LP_{11} mode, LP_{02} mode and LP_{21} mode. For sensing applications, MMI based on SMF is firstly introduced. The optimization on transition length of the taper structure is conducted to achieve good interference between the core mode and cladding mode. The temperature experiment is performed, and the sensitivity obtained is 0.0946 nm/°. For MMI using TMF, with similar dimension as the SMF, two mode pairs exist, LP_{01} mode with cladding mode and LP_{01} mode with LP_{11} mode, according to the spatial frequency spectrum. The temperature sensitivity of two mode pairs are also different. The simulation of FMF and its initial sensing exploration can help to further investigate the mode properties for future sensing applications.

3 Spatially and spectrally resolved imaging technique for mode characterization in FMF

In this chapter, the technique named spatially and spectrally resolved imaging is introduced for mode characterization in FMF. This technique can measure mode properties such as mode dispersion and intensity as well as phase distribution of modes. Other than that, mode coupling, including discrete and distributed mode coupling, can also be measured. Based on this technique, a modified system is presented for accurate mode characterization while an advanced algorithm is introduced for detailed mode-pairs classification.

3.1 Introduction

Mode-division multiplexing (MDM) using FMFs has attracted more and more attention as a promising technology to overcome the current capacity limitation of the optical fiber communication system. High-capacity and long-haul MDM transmission has been demonstrated recently [28]. Compared to SMFs, FMFs have larger core diameters to support high-order modes (HOMs) propagating along the fiber, and the nonlinearity can be reduced significantly at the same time. In addition to the same performance as SMFs in terms of dispersion and loss [21], FMFs have been successfully applied in many optical fiber communication devices and systems. For example, based on the interferometer structure and the stimulated Brillouin scattering, discrete and distributed FMF sensors were reported and have been applied to measure a wide range of parameters [15]. Moreover, few-mode erbium doped fiber amplifier (FM-EDFA) has been widely investigated in recent years. Six spatial modes amplifying FM-EDFA was reported in [29], in which differential mode gain can be reduced to less than 2 dB. Along with the increasing wide applications of FMFs, the investigation of mode properties in FMFs becomes necessary. One of the most important properties is mode coupling. In FMFs, due to fiber imperfection, bending and twisting, the random evolution of propagating modes can induce crosstalk between signals in different modes [30]. As an inevitable and fundamental obstacle in FMFs, mode coupling has a dramatic influence on FMF-based components and systems [31]. For example, in the MDM transmission system, mode coupling may result in signal degradation and increase the multiple-input-multiple-output digital signal processing (MIMO-DSP) complexity [32]. Thus, with techniques to quantify the mode coupling in FMFs, many FMF based systems and components can be optimized to achieve higher performance.

Recently, Masataka et al demonstrated the measurement of mode coupling along FMFs by using a synchronous multi-channel optical time-domain reflector (OTDR) [33]. Although this method can achieve the measurement of mode coupling, the setup was too complicated and costly. Spatially and spectrally resolved (S^2) imaging technique, initially presented by Nicholson et al [34] to analyze the modal content of large-mode-area fibers, provided properties of fiber under test (FUT), including the differential mode group delay (DMGD), power ratio between high-order modes (HOMs) and fundamental mode. In addition, S^2 imaging system has been utilized to characterize FMFs [35].

In this chapter, a standard S^2 imaging system is set up to measure the mode coupling in FMFs. A 100 m length of TMF and a 100 m length of four-mode fiber are measured respectively. Based on the data processing method in [36], some equations are further explored to get the parameters of discrete and distributed mode coupling. In the standard S^2 imaging system, however, the electromagnetic interference (EMI) in the experimental setup degrades the measurement accuracy. Thus, the S^2 imaging system is modified to mitigate the EMI and accurate measurement of mode properties is achieved. Other than that, an advanced algorithm is proposed for detailed mode-pairs classification based on data collected in S^2 imaging system.

3.2 Operation principle in S^2 imaging technique

In FMF, mode than one mode propagates along the optical fiber, which makes FMF a desirable candidate as mode interferometer due to the RI difference of fundamental mode and high-order modes. This inter-mode interference can also be utilized for mode characterization, which is the basic principle of S^2 imaging technique. This kind of interference occurs in both spatial (x, y) and spectral (ω) domain, which can be utilized for mode properties measurement, including the mode dispersion and profile. Also, mode coupling in FMF can be measured. In this section, mode interference and coupling are analyzed in S^2 imaging technique.

3.2.1 Mode interference in FMF

The TMF is used to introduce the mode interference in FMF. The schematic diagram is shown in Fig. 3.1.

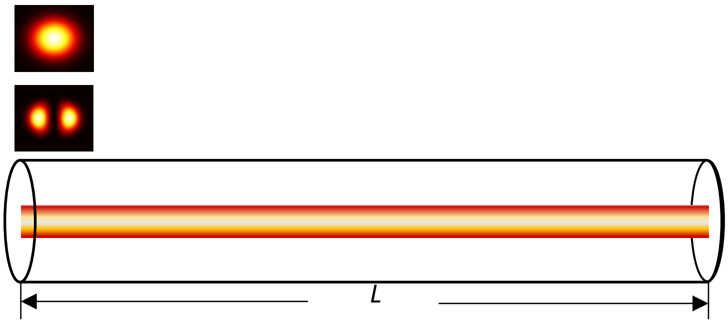

Fig. 3.1: Two-mode fiber model for inter-mode interference analysis.

In the input end, two modes are excited, including LP_{01} mode and LP_{11} mode. Thus the input electric field can be expressed as follows:

$$E(x,y,z=0,t)=\left[A_{01}\psi_{01}(x,y)+A_{11}\psi_{11}(x,y)\right]e^{-i\omega t}, \tag{3.1}$$

where A_{01} and A_{11} are the electric field amplitude of LP_{01} mode and LP_{11} mode, Ψ_{01} and Ψ_{11} are the electric field distribution in cross-section plane (x, y), ω is the optical angular frequency. Then, after the propagation along the TMF with length of L, the output electric field can be expressed as follows:

$$E(x,y,z=L,t)=\left[A_{01}\psi_{01}(x,y)e^{i\beta_{01}L}+A_{11}\psi_{11}(x,y)e^{i\beta_{11}L}\right]e^{-i\omega t}, \tag{3.2}$$

where β_{01} and β_{11} are the propagation constant of LP_{01} mode and LP_{11} mode and they are related to ω. Therefore, the output intensity can be obtained by multiplying Eq. (3.2) and its conjugate, the result of which is as follows:

$$I(x, y, z = L, \omega) = E \cdot E^* = I_{01}\left|\psi_{01}(x, y)\right|^2 + I_{11}\left|\psi_{11}(x, y)\right|^2 + . \quad (3.3)$$
$$2\,\mathrm{Re}\left\{A_{01}\psi_{01}(x, y)A_{11}^*\psi_{11}^*(x, y)e^{i\left[\beta_{11}(\omega)-\beta_{01}(\omega)\right]L}\right\}$$

It can be seen that the output intensity is composed of direct current components and the interference term, which is directly related to the mode propagation constants. Then, based on the chromatic dispersion, propagation constant is expanded in Taylor form as follows:

$$\beta(\omega) = \beta(\omega_0) + \left.\frac{d\beta}{d\omega}\right|_{\omega=\omega_0}(\omega - \omega_0) + \frac{1}{2}\left.\frac{d^2\beta}{d\omega^2}\right|_{\omega=\omega_0}(\omega - \omega_0)^2 + \ldots, \quad (3.4)$$

where the first term in the right end is the propagation constant under certain angular frequency ω_0, and the second term is mode dependent. Different modes own different first derivatives of β on ω, which introduces the inter-mode chromatic dispersion. This kind of dispersion results from the group velocity difference between modes. The group velocity can be expressed as follows:

$$\tau = \frac{1}{v_g} = \frac{d\beta}{d\omega}, \quad (3.5)$$

where V_g is the group velocity and τ is the group delay. τ represents the time delay after propagation along fiber with unit length. Thus, based on Eq. (3.5) and Eq. (3.4), the output intensity in Eq. (3.3) can be updated as follows:

$$I(x, y, z = L, \omega_0 + \Delta\omega) = I_{01}\left|\psi_{01}(x, y)\right|^2 + I_{11}\left|\psi_{11}(x, y)\right|^2 + , \quad (3.6)$$
$$2\,\mathrm{Re}\left\{A_{01}\psi_{01}(x, y)A_{11}^*\psi_{11}^*(x, y)e^{i\left[\beta_{11}(\omega_0)-\beta_{01}(\omega_0)\right]L}e^{i(\tau_{11}-\tau_{01})L\cdot\Delta\omega}\right\}$$

where τ_{01} and τ_{11} are the mode group delay of LP_{01} mode and LP_{11} mode, $\Delta\omega$ is the angular frequency variation around ω_0. To extract the inter-mode chromatic dispersion terms, Eq. (3.6) can be updated to Eq. (3.7) as follows:

$$I(x, y, z = L, \omega_0 + \Delta\omega) = I_{01}\left|\psi_{01}(x, y)\right|^2 + I_{11}\left|\psi_{11}(x, y)\right|^2 + , \quad (3.7)$$
$$2\,\mathrm{Re}\left\{A_{01}\psi_{01}(x, y)A_{11}^*\psi_{11}^*(x, y)\right\}\cos(\Delta\phi_{11})\cos(\Delta\tau_{11}\cdot\Delta\omega)$$

where $\Delta\phi_{11}$ is the initial phase difference between LP_{01} mode and LP_{11} mode under the angular frequency ω_0, $\Delta\tau_{11}$ is differential mode group delay (DMGD) of LP_{01} mode and LP_{11} mode after the propagation along the TMF. It can be concluded from Eq. (3.7) that, for a fixed point (x, y) of output profile, the intensity changes with optical angular frequency in cosine form and the corresponding frequency is DMGD.

For S^2 imaging technique to characterize TMF, DMGD between the fundamental mode and the high-order mode is the basic measurand. However, for FMF with more than two modes supported, the inter-mode interference will become complicated and it is not convenient to measure individual DMGD between fundamental mode and every high-order mode. Thus, in S^2 imaging system, mode excitation is necessary and important to guarantee the fundamental mode as the major mode and other high-order modes as the minors. This will be discussed in the next section. Thus, with fundamental mode LP_{01} mode as only major mode, the inter-mode interference in FMF with more than two modes supported is expressed as follows:

$$\begin{aligned} I(x,y,z = L, \omega_0 + \Delta\omega) &= I_{01}\left|\psi_{01}(x,y)\right|^2 + \\ & 2\sum_{mn} \mathrm{Re}\left\{A_{01}\psi_{01}(x,y)A_{mn}^{*}\psi_{mn}^{*}(x,y)\right\}\cos\left(\Delta\phi_{mn}\right)\cos\left(\Delta\tau_{mn}\cdot\Delta\omega\right) \end{aligned}, \tag{3.8}$$

where direct current component only includes LP_{01} mode with major power and $\Delta\tau_{mn}$ is DMGD between LP_{01} mode and every high-order mode with subscript of *m* and *n*.

3.2.2 Mode coupling in FMF

As introduced in chapter 2, modes in FMF are orthogonal to each other, which concludes that the modes can propagate along the optical fiber independently without coupling. However, due to the imperfect fabrication of optical fiber or other ambiance factors such as temperature and strain, the coupling between modes always happens [37]. Mode coupling (MC) in FMF has been widely investigated in both theoretical and experimental way. Different models were proposed, such as power coupling model and electric field coupling model, in which power coupling model is the common one since it can interpret the coupling in an intuitive and quantitive way [30]. MC occurs in many forms, among which two kinds of MC are usually discussed, discrete MC and distribute MC [35]. Discrete MC takes place on the splicing point between SMF and FMF while distributed MC occurs along the FMF. Generally, the discrete MC is larger than distributed MC in terms of power ratio. In S^2 imaging technique, the mode excitation is utilized in the input end of FMF, where discrete MC dominates. Along the FMF, the power fraction of fundamental mode will couple to high-order modes, which is based on the distributed MC. Similarly, the TMF model is utilized to discuss these two kinds of MC, and the schematic diagram is shown in Fig. 3.2.

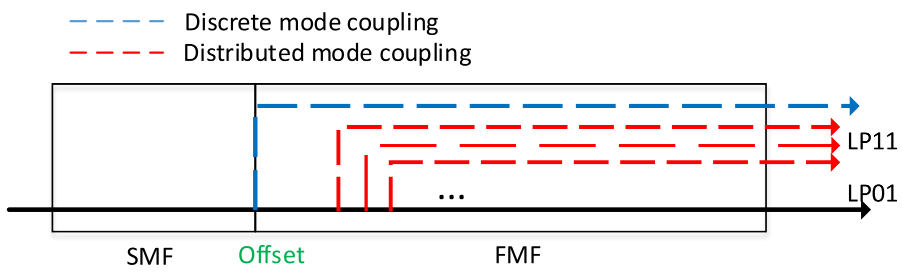

Fig. 3.2: Schematic diagram of discrete and distributed mode coupling.

3.3 S^2 imaging experimental setup for mode characterization

The S^2 imaging system experiences the change from the combination of broadband light source and optical spectrum analyzer to tunable laser source (TLS) and CCD camera [36]. The latter setup owns the advantages of fast measurement, easy operation and high accuracy. In this chapter, the setup of a tunable laser source and a CCD camera is utilized for FMF characterization. The experimental setup is shown in Fig. 3.3. TLS is used as the light source with tunable wavelength. The attenuator here is applied to protect the CCD camera from saturation. Offset splicing is introduced as a method to excite the high-order modes in the input end of FMF. In the meantime, this kind of mode excitation can also guarantee LP_{01} mode as the major mode and high-order modes as the minors. Collimator is a lens system that can realize the light coupling from optical fiber end to the free space so that the intensity distribution at the output end of the fiber can be collected by the camera. Beam expander here is used to enlarge the optical output pattern, which can be fully recorded by CCD camera. The beam expander is a conventional telescope system, which contains a negative lens with a small focal length and a positive lens with a large focal length. The beam expanding ratio is the ratio between two focal lengths. CCD is used to record the intensity profile of the output end. According to the aforementioned principle of S^2 imaging technique, the intensity will change with different optical frequencies. Thus, data collection in this experiment is to record the intensity profile by camera under every wavelength tuned by TLS.

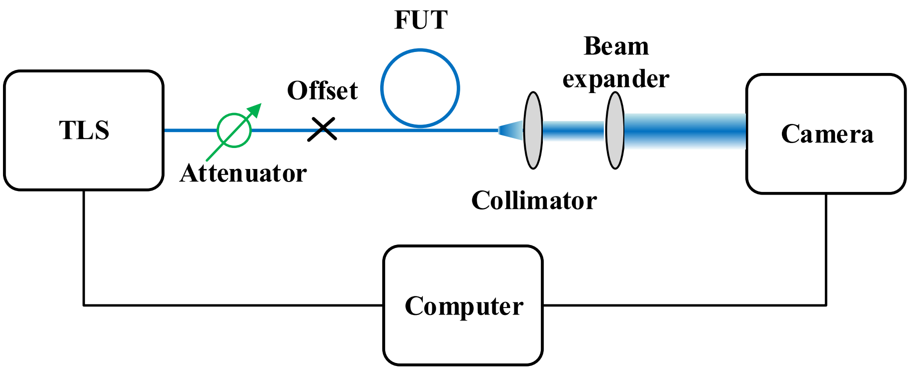

Fig. 3.3: S^2 imaging experimental setup.

In the experiment, the fiber under test (FUT) is FMF. Two kinds of step-index FMFs, including two-mode fiber (TMF) and four-mode fiber, are measured. The FMFs are from OFS, Furukawa, and their specifications, especially the DMGDs, are provided as follows: for TMF, LP_{11}-LP_{01}: 3.5 ps/m; for four-mode fiber, LP_{11}-LP_{01}: 2.0 ps/m, LP_{02}-LP_{01}: 3.0 ps/m, LP_{21}-LP_{01}: 3.9 ps/m. The length of two FMFs are both 100 m. Thus, the maximum DMGD is 390 ps. Based on Eq. (3.8), the relationship between maximum measurable DMGD value and the frequency scanning interval meets the Nyquist principle, which can be expressed as follows:

$$\Delta\tau_{max} \cdot 2 \cdot \Delta f = 1. \tag{3.9}$$

Thus, to measure the DMGD of two FMFs, the frequency scanning interval of TLS under maximum DMGD of 390 ps is 1.28 GHz. In the experiment, the interval is confirmed to be 1 GHz, which guarantees the maximum measurable DMGD of 500 ps. In addition, based on Eq. (3.8), the measured DMGD is obtained under the angular frequency ω_0 and the modal chromatic dispersion is under wavelength of 1550 nm. Thus, the start frequency of TLS is 193.415 THz. For data collection, we aim to collect 512 pictures, which confirms that the end frequency of TLS is 193.927 THz.

In the experiment, offset splicing between SMF and FMF is utilized for mode excitation. For example, due to the electric field mismatch between SMF and TMF, LP_{11} mode will be excited, and the excitation ratio between excited LP_{01} mode and LP_{11} mode in TMF will change with offset distances. This can be simulated based on the equation as follows:

$$\alpha = \frac{\int_{-\infty}^{+\infty}\int_{-\infty}^{+\infty} E_{01}(x,y)E_{11}(x,y)dxdy}{\int_{-\infty}^{+\infty}\int_{-\infty}^{+\infty} E_{01}^{2}(x,y)dxdy}, \tag{3.10}$$

where *OI* is the overlap integral [38], E_{01} represents electric field of input LP_{01} mode while E_{11} represents excited LP_{11} mode. The simulated excitation result is shown in Fig. 3.4. As is shown in Fig. 3.4, the power ratio (MPI, multipath interference) increases with off-center distances.

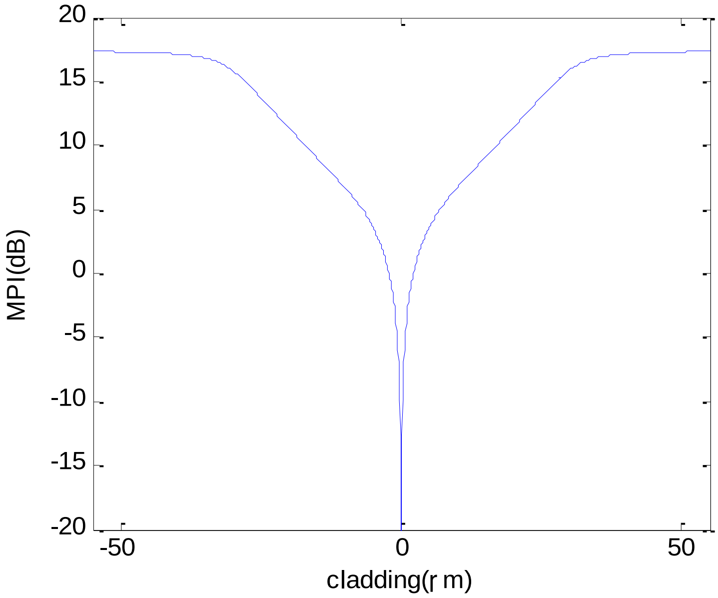

Fig. 3.4: Power ratio between excited LP_{11} mode and LP_{01} mode under different offset distances.

For the collimator, the focal length is 11 mm, and it can convert the Gaussian beam from fiber end to parallel beam in free space. Focal lengths of the negative lens and positive lens are -75 mm and 30 mm, which makes the expanding ratio 2.5x. Thus, with all components set, the computer controls the TLS and CCD camera synchronously to record the output intensity of optical fiber end under every wavelength.

3.4 Signal processing and results

As introduced above, the data collected are a series of intensity profiles. For example, for the FUT of TMF, one of the pictures is shown in Fig. 3.5. It is the interference pattern between LP_{01} mode and LP_{11} mode in the spatial domain.

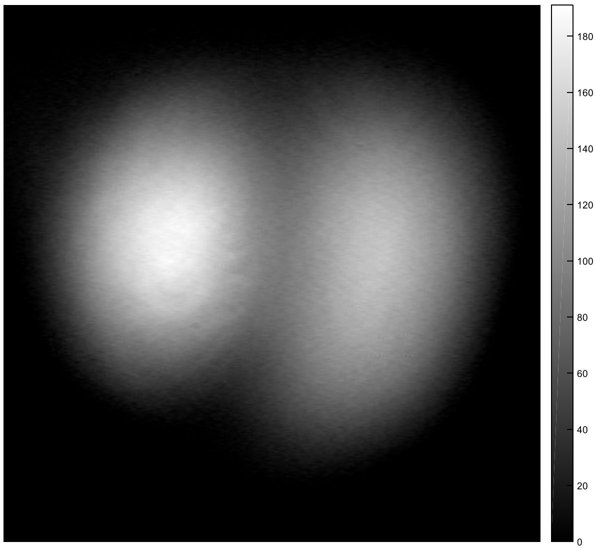

Fig. 3.5: The LP_{01} and LP_{11} mode interference pattern.

The pictures are read in MATLAB, and certain fixed point is selected and the pixel values of this point in every image are collected. This corresponds to the interference spectrum in the spectral domain. The FFT result on data collected is shown in Fig. 3.6.

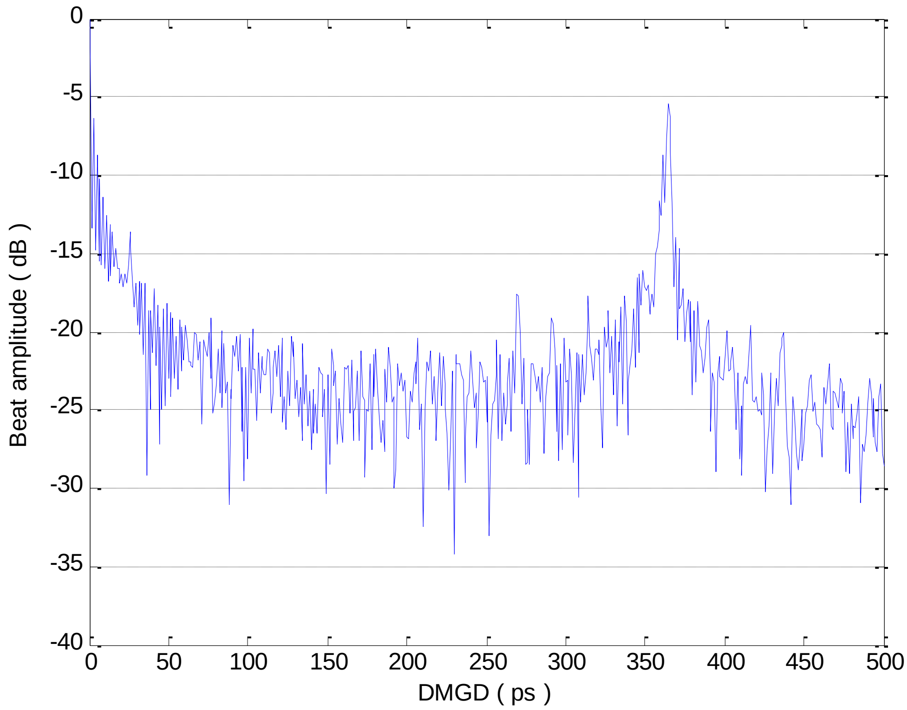

Fig. 3.6: FFT result on fixed point of picture collected under every optical frequency.

As is shown in Fig. 3.6, the Y-axis represents the beat amplitude between two modes and X-axis represents the spatial frequency, which is the DMGD value according to the principle introduced above. It can be seen that except the direct current component which locates on position where DMGD is equal to zero, another peak locates away. The X axis value of this peak is 363.6 ps/m. From Eq. (3.7), the frequency of interference pattern in spectral-domain is the DMGD between two modes. Thus, it can be concluded that the measured DMGD of this TMF is around 3.6 ps/m, which agrees well with the specifications. Similarly, the measurement results on four-mode fiber are shown in Fig. 3.7. It can be seen that three peaks appear, which correspond to the three mode pairs: LP_{01}+LP_{11}, LP_{01}+LP_{02}, LP_{01}+LP_{21}. The obtained DMGD values in four-mode fiber with length of 100 m are 199.6 ps, 300.2 ps and 388.7 ps, which also agree well with the given specifications of four-mode fiber aforementioned.

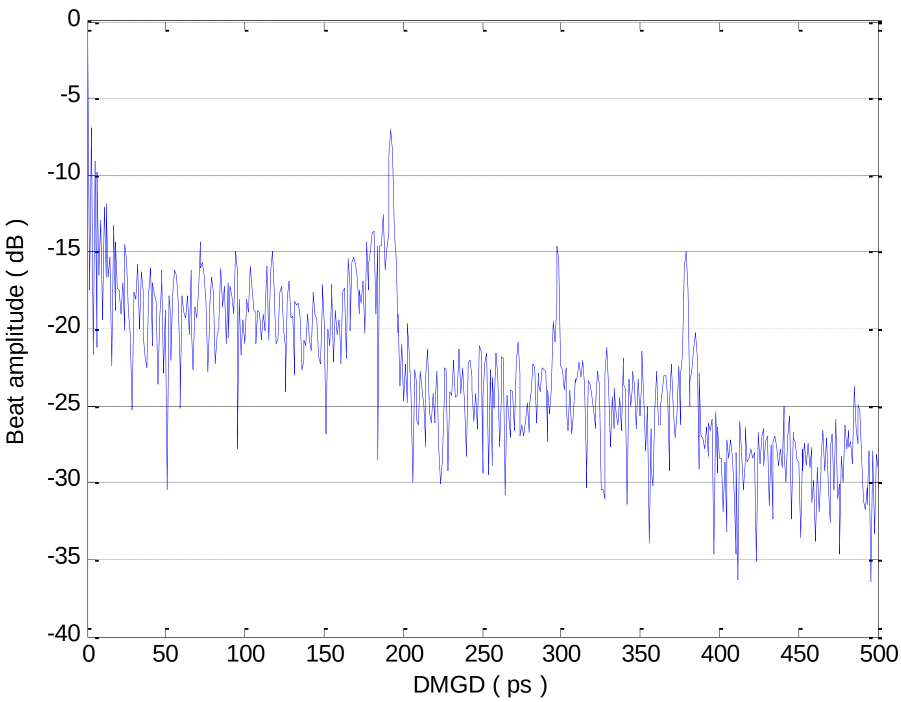

Fig. 3.7: DMGD measurement results on four-mode fiber.

For mode intensity distribution results, the algorithm used is the filtering technique [36]. As introduced above, the interference between the fundamental mode and high-order modes follows Eq. (3.8). In another way, the output electric field distribution can be expressed as follows:

$$E\left(x,y,\omega\right) = E_1\left(x,y,\omega\right) + E_2\left(x,y,\omega\right), \tag{3.11}$$

where E_1 and E_2 represent the major mode and minor mode, respectively. Then, the intensity can be concluded as follows:

$$I\left(x,y,\omega\right) = I_1\left(x,y,\omega\right) + 2\,\mathrm{Re}\left\{\sqrt{I_1\left(x,y,\omega\right)}E_2\left(x,y,\omega\right)\right\}, \tag{3.12}$$

where the second term in the right is the interference term. Based on this, another function is defined as follow:

$$J\left(x,y,\omega\right) = \frac{I\left(x,y,\omega\right) - I_1\left(x,y,\omega\right)}{2\sqrt{I_1\left(x,y,\omega\right)}} = \mathrm{Re}\left\{E_2\left(x,y,\omega\right)\right\}, \tag{3.13}$$

where J is used to extract the interference term E_2. I_1 is the direct current component with low frequency while J is the interference term with high frequency. Thus, the filtering technique can be used to classify and extract them. Firstly, a low-pass filter with a center frequency around 5 ps according to the X-axis in the FFT result is used to get I_1. Then, with obtained I_1, J can be extracted based on Eq. (3.13). By using bandpass filters with the center frequencies where peaks locate in Fig. 3.6 and Fig. 3.7, the intensity value of one mode-pair and three mode-pairs on that fixed point can be obtained for TMF and four-mode fiber. The bandwidth of bandpass filter can be obtained from the parameter of full width at half maximum height (FWMH). Then the intensity of both fundamental mode and high-order modes can be obtained using the following equations.

$$I_{FM}\left(x,y\right) = 2\int d\omega\left(J_{Lowpass}\left(x,y,\omega\right)\right) \tag{3.14}$$

$$I_{HOM}\left(x,y\right) = 2\int d\omega\left(J_{Bandpass}\left(x,y,\omega\right)\right) \tag{3.15}$$

The results of TMF and four-mode fiber are shown in Fig. 3.8 and Fig. 3.9, respectively.

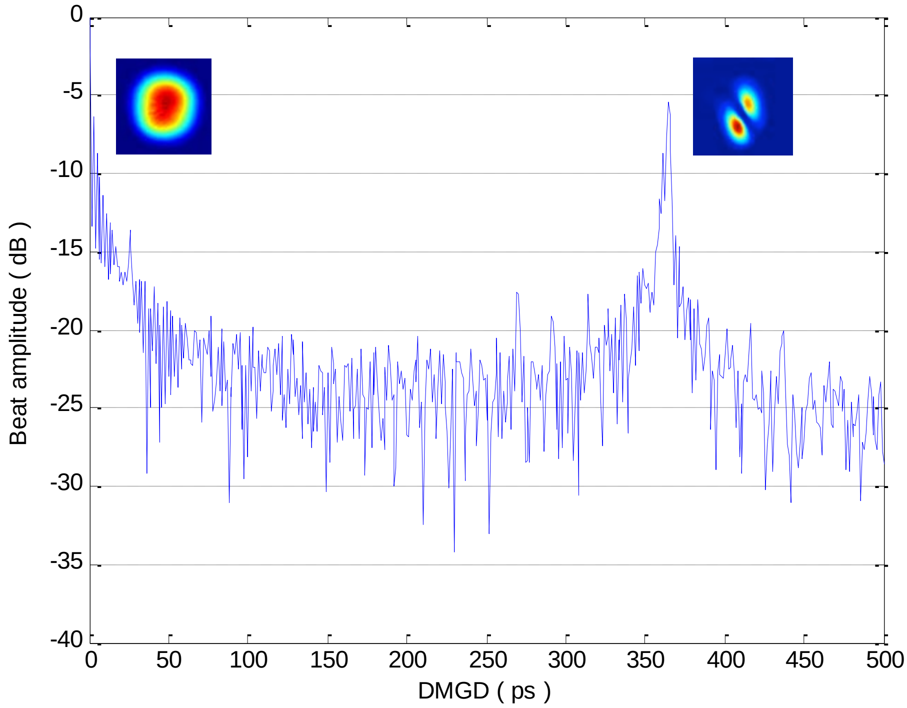

Fig. 3.8: Intensity distribution of LP_{01} mode and LP_{11} mode on two peaks.

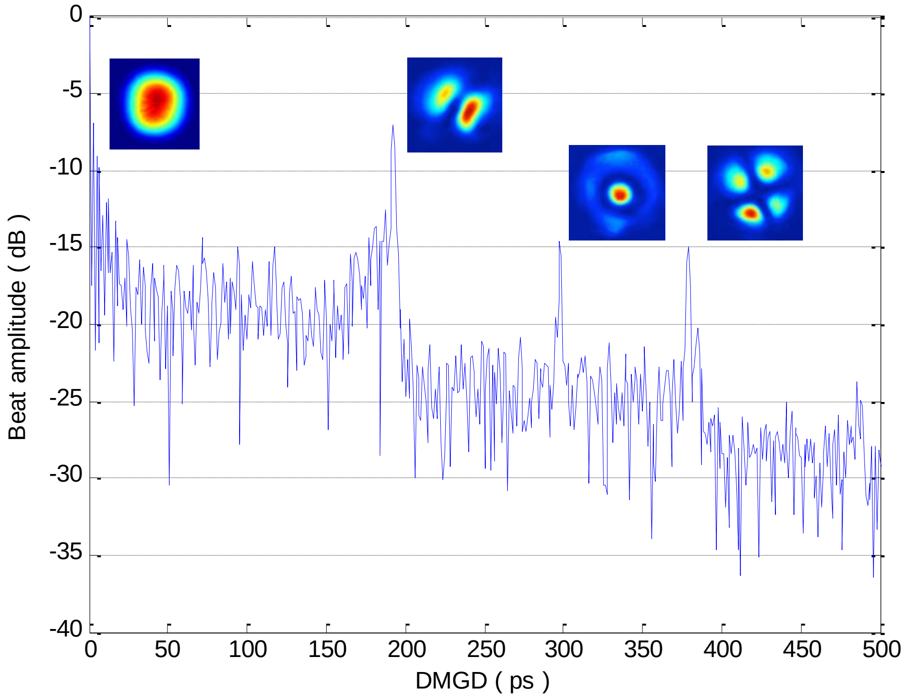

Fig. 3.9: Intensity distribution of LP_{01} mode, LP_{11} mode, LP_{02} mode and LP_{21} mode.

From the mode calculation results in chapter 2, the modes in FMF, including fundamental mode (LP_{01}) and high-order modes (LP_{11}, LP_{02}, LP_{21}) are all recovered successfully, which demonstrates the feasibility of S^2 imaging technique on mode intensity distribution characterization.

The intensity distribution is recovered based on the amplitude information of FFT results. Then, for the phase component of FFT results, following the same data processing method mentioned above, the phase distribution of modes can also be obtained. The results are shown in Fig. 3.10 and Fig. 3.11.

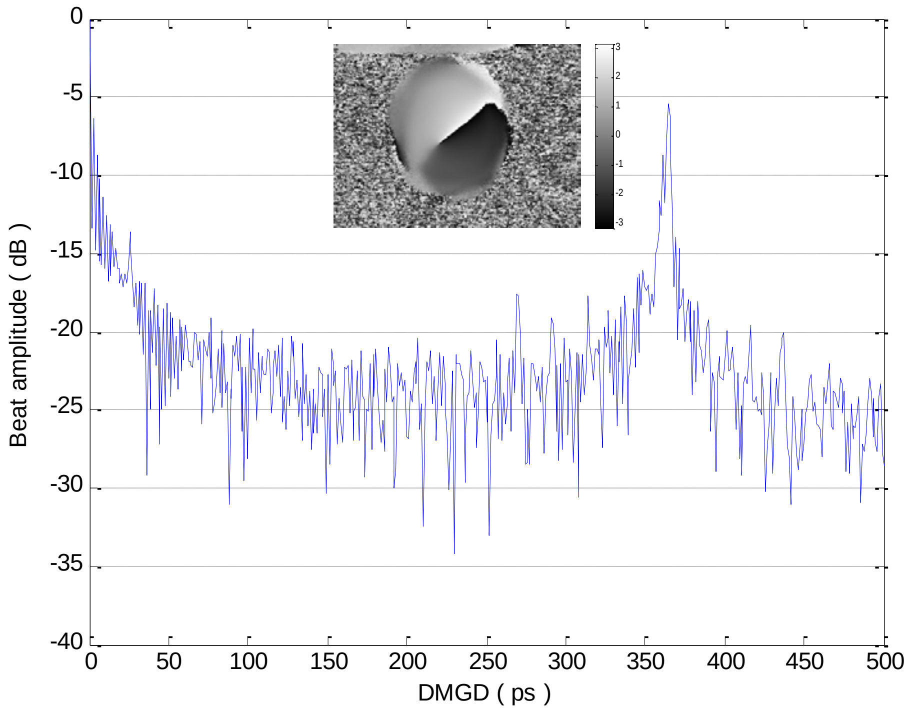

Fig. 3.10: Phase distribution of LP_{11} mode in TMF.

It can be seen that, for LP_{11} mode in TMF, the phase difference between two sections is around π, which corresponds to the mode calculation result. The noisy points in the mode patterns are due to electromagnetic interference, which can be mitigated by the method introduced in the next section. The results of four-mode fiber also show the correct phase distribution of three high-order modes. In summary, by S^2 imaging technique, not only intensity but also phase distribution of modes can be measured successfully.

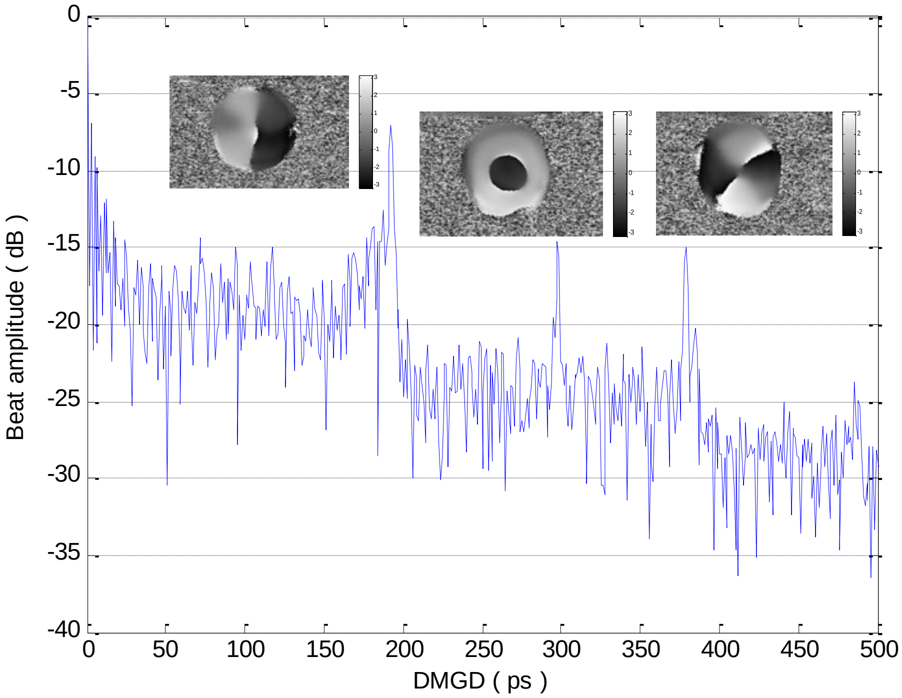

Fig. 3.11: Phase distribution of LP_{11} mode, LP_{02} mode and LP_{21} mode.

As mentioned before, mode coupling (MC) happens in FMF, and there are two kinds of MC: discrete and distributed MC, which can also be measured using S^2 imaging technique. In Fig. 3.8, the peak represents the interference between LP_{11} mode and LP_{01} mode, which are both excited in the input end of FMF. This kind of MC is the discrete MC from LP_{01} mode in SMF to LP_{11} mode and LP_{01} mode in TMF. Based on Eq. (3.14) and Eq. (3.15), the power can be obtained by the integral on the optical fiber cross section, which can be expressed as follows:

$$I = \iint dxdy I_{HOM/FM}(x,y), \tag{3.16}$$

where I_{HOM} and I_{FM} are the intensity of HOM and fundamental mode (FM). For the discrete and distributed MC, in Fig. 3.8, the plateau represents the coupling from LP_{01} mode to LP_{11} mode, which happens along the fiber under test [39]. Thus, two kinds of MC can be expressed by Eq. (3.17) and Eq. (3.18):

$$MC_{discrete} = 10\log_{10}\left[\frac{\sum_{mn}\iint I_{mn}(x,y)\,dxdy}{\iint I_{01}(x,y)\,dxdy}\right], \tag{3.17}$$

$$MC_{distributed} = 10\log_{10}\left[\frac{\iint I_{Fullband}\left(x,y\right)dxdy - \sum_{m} \iint I_{m}\left(x,y\right)dxdy}{\iint I_{01}\left(x,y\right)dxdy}\right]. \tag{3.18}$$

Thus, the mode coupling measurement results for TMF and four-mode fiber can be obtained, which are shown in Table 3.1 and Table 3.2.

Table 3.1 Discrete and distributed mode coupling measurement results in TMF.

Parameters	Value (dB)
Discrete mode coupling	-11.53
Distributed mode coupling	-15.66

Table 3.2 Discrete and distributed mode coupling measurement results in four-mode fiber.

Parameters	Value (dB)
Discrete mode coupling	LP_{11} / LP_{01} : -11.62
	LP_{02} / LP_{01} : -14.56
	LP_{21} / LP_{01} : -14.72
	Overall : -9.49
Distributed mode coupling	Overall : -5.68

3.5 Modified S^2 imaging system

In the standard S^2 imaging system, electromagnetic interference (EMI) happens inevitably, which will introduce the noise on the data collected. In this section, the S^2 imaging system is modified to mitigate EMI and performance is improved as a result.

The modified S^2 imaging system is shown in Fig. 3.12. With other components unchanged, an aluminum tube with a length of 50 mm is fabricated and fixed on the front of the camera to mitigate the EMI. The internal and external diameter of this tube is 23 mm and 25 mm, which can accommodate the optical beam. The tube is fabricated with helical burr to be fixed into the camera [40].

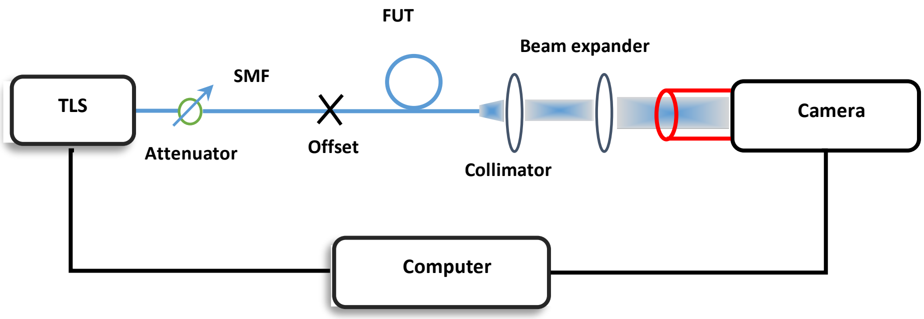

Fig. 3.12: Modified S^2 imaging system.

Fig. 3.13 (a) shows one image collected in the standard S^2 system (with EMI), in which high-level noise can be seen. The image collected by the modified S^2 system is shown in Fig. 3.13 (b). We can observe that the noisy points are mitigated effectively.

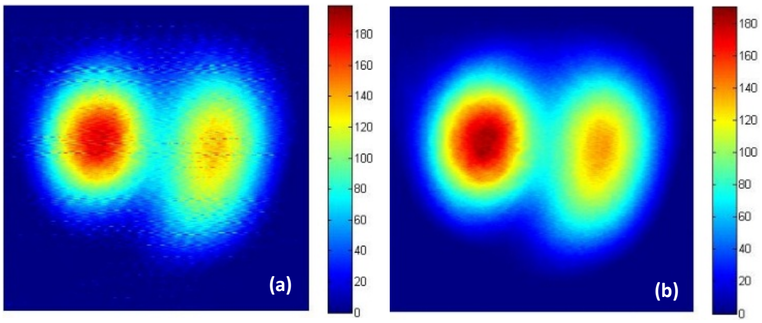

Fig. 3.13: Images collected by standard (a) and modified (b) S^2 imaging system.

According to the DMGD and intensity distribution characterization performance, the comparison of the result is shown in Fig. 3.14 for TMF and Fig. 3.15 for four-mode fiber. It can be seen that, with EMI, the peaks in results fail to appear, which makes the DMGD measurement inaccurate. Also, the mode intensity distribution fails to be recovered clearly, especially for some high-order modes. For mode coupling measurement, the corresponding comparison is shown in Table 3.3 and Table 3.4.

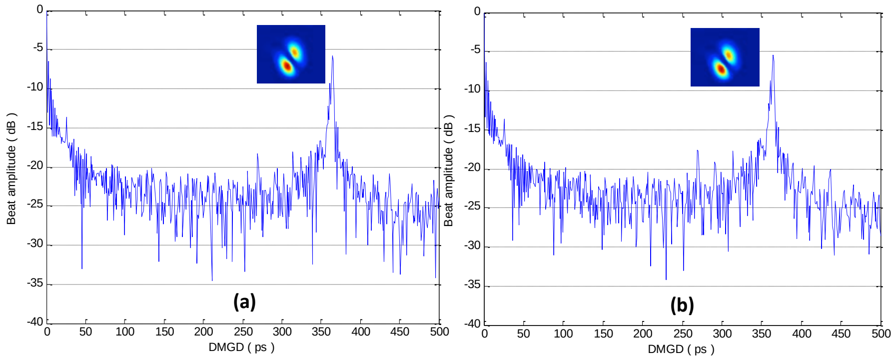

Fig. 3.14: Results comparison for TMF between standard S^2 imaging system (a) and modified S^2 imaging system (b).

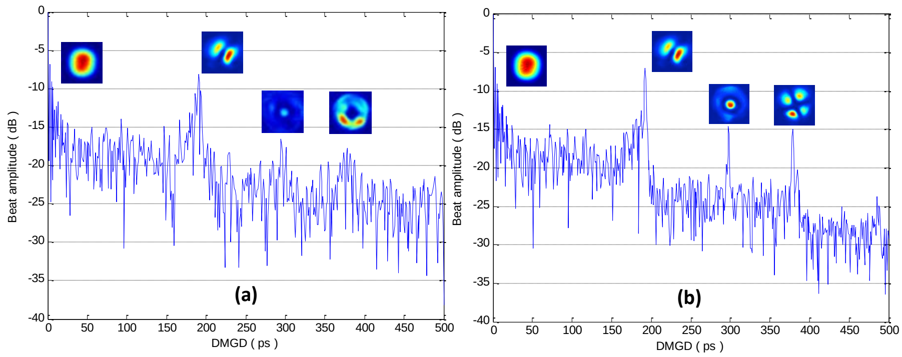

Fig. 3.15: Results comparison for four-mode fiber between standard S^2 imaging system (a) and modified S^2 imaging system (b).

Table 3.3 Comparison of discrete and distributed mode coupling measured by standard and modified S^2 imaging system (TMF)

	Total discrete mode coupling (dB)	Total distributed mode coupling (dB)
Standard S^2 system	-10.21	-14.44
Modified S^2 system	-11.53	-15.66
Improvement	1.32	1.22

Table 3.4 Comparison of discrete and distributed mode coupling measured by standard and modified S^2 imaging system (Four-mode fiber)

	Total discrete mode coupling (dB)	Total distributed mode coupling (dB)
Standard S^2 system	-10.91	-3.01
Modified S^2 system	-9.49	-5.68
Improvement	1.42	2.67

In summary, with modified S^2 imaging system, EMI is mitigated and the measurement performance is improved, including the DMGD location, intensity distribution recovery and mode coupling results.

3.6 Advanced algorithm for mode-pairs classification

For the S^2 imaging system, fundamental mode is the major mode with most power while other high-order modes are minor modes with little power. This can help to make sure the interference only happens between one major mode and other minor modes. However, when the number of modes increases or the power level of modes is equal to each other, this technique becomes invalid. On the other hand, with filtering technique, degenerate modes, such as the aforementioned LP_{11a} and LP_{11b} mode, cannot be distinguished. Thus, a new algorithm is necessary to solve this problem. In this section, an advanced algorithm based on principal component analysis (PCA) is introduced for mode-pairs classification [41].

Based on Eq. (3.8), all the modes, including degenerate modes, are considered in the interference term. Then, the output intensity can be expressed as follows:

$$X\left(x, y, \omega\right) = I\left(x, y\right) + \sum_{k=1}^{M-1} \sum_{l=k+1}^{M} 2\sqrt{P_k P_l} F_k F_l \cos\left(\tau_{kl}\omega + \phi_{kl}\right), \tag{3.19}$$

where *I (x, y)* is the direct current component with low frequency, *M* is the number of modes supported in FMF, *k* and *l* are the mode labels, *P* is the intensity, *F* is the electric field distribution, τ_{lk} is the DMGD between mode *k* and mode *l*, ϕ is their initial phase difference. Eq. (3.19) shows the interference between all mode-pairs. As introduced before, bandpass filter is utilized on the peaks in fast Fourier transform (FFT) results and the corresponding mode intensity distribution can be obtained. If more bandpass filters are used around one peak, except for the dominate mode, other modes will appear, as shown in Fig. 3.16. It can be seen that around the peak, there is more than one mode, which indicates that more than one mode-pair interferes in this region. Thus, an algorithm can be used to extract them.

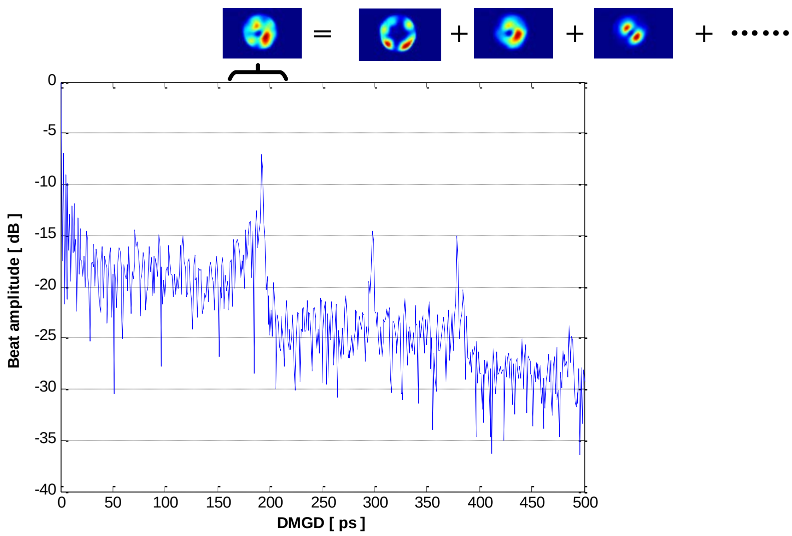

Fig. 3.16: Modes recovered using bandpass filtering around the peak.

PCA is a data classification method to extract independent components that represents most information of the data set. This data processing method has been widely investigated and is also easy to use. Firstly, the mathematic model is introduced briefly. A sample set X with a size of n and a variable number of p can be expressed as follows:

$$X = \begin{pmatrix} x_{11} & x_{12} & \cdots & x_{1p} \\ x_{21} & x_{22} & \cdots & x_{2p} \\ \vdots & \vdots & \vdots & \vdots \\ x_{n1} & x_{n1} & \cdots & x_{np} \end{pmatrix} = \left(x_1, x_2, \cdots x_p\right). \tag{3.20}$$

Principal components can then be expressed as follows:

$$\begin{cases} F_1 = a_{11}x_1 + a_{12}x_2 + \cdots a_{1p}x_p \\ F_2 = a_{21}x_1 + a_{22}x_2 + \cdots a_{2p}x_p \\ \cdots \\ F_n = a_{n1}x_1 + a_{n2}x_2 + \cdots a_{np}x_p \end{cases}, \tag{3.21}$$

where F represents the principal components from reconstructed samples, α is the corresponding coefficient. By diagonalizing the coefficients matrix, eigenvalues and eigenvectors can be obtained, which can help to finalize the principal component F.

Based on Eq. (3.19), new variables are obtained, which can be expressed as follows:

$$\overline{X}^2 = \left(X - I\right)^2, \tag{3.22}$$

$$C\left(x, y\right) = \int \overline{X}^2 d\,\omega, \tag{3.23}$$

$$C'\left(\omega\right) = \iint \overline{X}^2 dxdy\ , \tag{3.24}$$

where C and C' are variables that represent the spatial and spectral components of mode-pairs. Based on the data obtained in S^2 imaging system for four-mode fiber, C and C' can be updated. Then, the PCA method is used in C and C', and both spectral and spatial information can be obtained. Some of the results are shown in Fig. 3.17. It can be seen that, not only the interference between the fundamental mode and generate modes, but also the interference between degenerate modes are classified successfully.

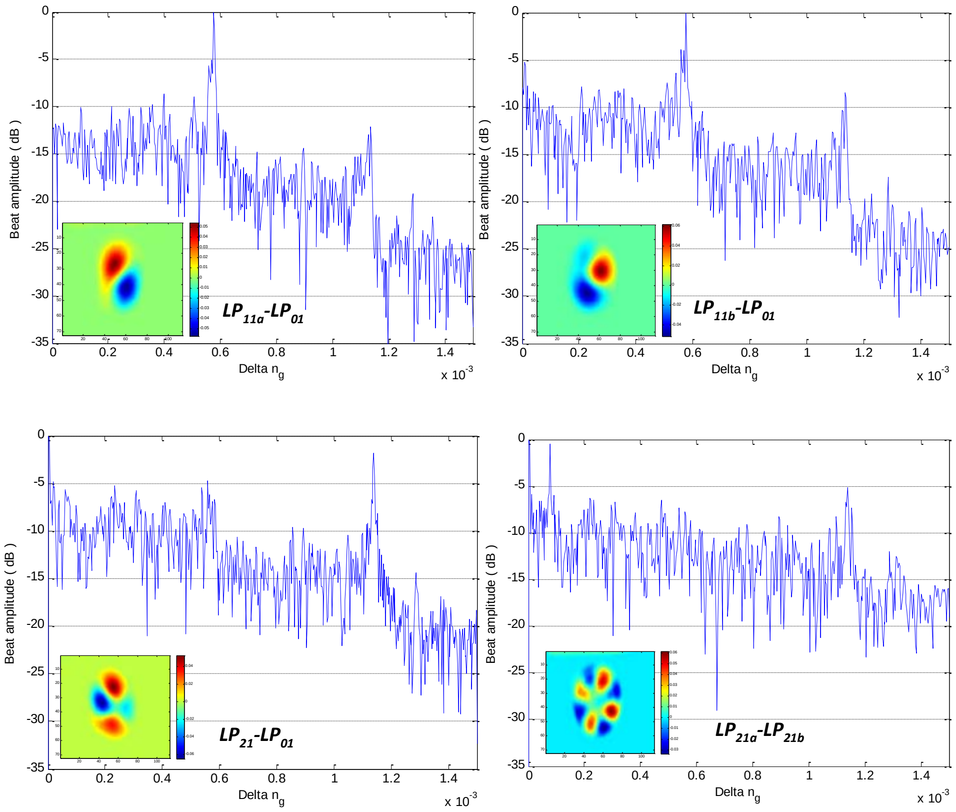

Fig. 3.17: Mode-pairs classification results using PCA method.

3.7 Summary

In this chapter, S^2 imaging technique is employed for FMF characterization. Mode interference and coupling theory are introduced in FMF, which are utilized later for data processing. Based on this S^2 imaging system, two kinds of FMF are characterized. With output intensity pattern collected under every wavelength, the filtering technique is applied. The obtained results include DMGD between FM and HOMs and their intensity as well as phase distribution. Other than these, mode coupling, including discrete and distributed coupling are obtained in TMF and four-mode fiber. To mitigate the noise, S^2 imaging system is modified, and EMI is mitigated successfully, which help to improve the characterization performance. Finally, to classify interference mode-pairs, especially for degenerate modes, PCA method is introduced, and some of the interference mode-pairs are recovered.

4 MCF and its application on torsion sensing

In last chapter, the FMF has been demonstrated with excellent performance for temperature sensing based on the mode interference. Similar to mode interference in FMF, the interaction between cores in MCF, such as core-mode coupling, can be also utilized for sensing. Thus, in this chapter, the sensing application of MCF is explored, and a novel torsion sensor based on inter-core mode coupling in seven-core fiber is proposed. The torsion sensor is designed and fabricated by tapering a seven-core fiber and splicing single-mode fibers on both ends. The waist-diameter and length of taper are optimized to achieve a good transmission spectrum. The torsion sensing experiment results show that the sensitivity of this torsion sensor increases with fiber twist angle, and the highest can reach 1 nm/^{o}. When twisting the tapered seven-core fiber in the clockwise and counterclockwise directions, the wavelength is observed to shift in the opposite directions, which demonstrates its capability for rotation direction discrimination. In addition, a batch of torsion sensors is fabricated, and experiments are repeated to discuss its performance of accuracy and stability. In theory, mode coupling dynamic and optical anisotropy are analyzed in twisted seven-core fiber to discuss the sensitivity results. This novel torsion sensor based on seven-core fiber provides a good candidate for torsion sensing in industrial applications.

4.1 Introduction

Fiber optic sensor, owing to its excellent advantages such as light-weight, low-cost, compact size, electromagnetic interference immunity, has been considered as a good sensing scheme for various applications, such as aerospace, railway, biomedicine and civil engineering. Different fiber optic sensor structures have been designed for different parameter measurements, such as temperature, strain, vibration. Among them, torsion is one of the important mechanical parameters, and its measurement is significant in the areas of robotics and structure health monitoring. For example, needle-based continuum robots are proposed for surgical interventions and shape sensors in it enable the needles to steer through the tissue to realize the accurate positioning. However, the inevitably induced torsion may interfere with the tool tip, resulting in inaccurate three-dimensional (3D) shape reconstruction [42]. Thus, an optical fiber torsion sensor is applied here to realize real-time as well as accurate torsion angle monitoring when the needle-based robot is working. Other than that, the optical fiber torsion sensor is also utilized for fatigue failure detection of wind turbines blades [43]. For torsion sensing applications, high sensitivity has always been the main concern, and various optical fiber sensing schemes are proposed. For example, long period grating (LPG) in single-mode fiber was demonstrated to be highly sensitive on torsion ratio while different high-order modes, which corresponds to different resonant wavelength on LPG spectrum, owns different sensitivities. Among these high-order modes, LP_{04} mode was demonstrated with the highest torsion sensitivity of 31.6 pm/(rad/m) [44]. Sagnac interferometer (SI) was also a frequently proposed torsion sensing scheme and SMF-based SI with low birefringence has been demonstrated experimentally with high sensitivity, which can achieve as high as 3.25nm/^{o} [45]. For MCF, there are also some structures proposed and demonstrated with excellent performance. For example, a pre-twisted helical structure on seven-core fiber with multi-mode fiber spliced on both ends was reported to be highly sensitive to torsion angle with a sensitivity of 0.118 nm/(rad/m) [46]. In summary, for these optical fiber structures for torsion sensing with high sensitivity, including LPG, SI and MCF, home-made specialty optical fibers have to be employed and the fabrication process is inevitably time-consuming and costly.

As introduced before, MCF is one of the typical optical fibers for the SDM system and has already been used in sensing communities apart from communication [8,47,48]. There are various MCFs proposed for sensing, such as twin-core fiber, three-core fiber, and they have been demonstrated with excellent performance on various parameters measurement [49]. For example, supermodes supported in SCF with isometrically arranged cores can be utilized for fiber laser design with high beam quality, which can be further used for harmonic generation [50,51]. In SCF, when the cores are arranged with small core pitch size, strong mode coupling will happen. This kind of mode coupling can be described by supermode theory. The interference of supermode in SCF has been demonstrated for high-temperature and strain sensing [52,53]. Shape sensing has always been a concern among measurands, especially in a 3D way [54]. To achieve comprehensive as well as accurate 3D shape sensing, three-core fibers with distributed fiber Bragg grating (FBG) inscribed on each core was designed, and 3D shape sensing can be realized through distributed curvature sensing. For SCF, twisted structure with distributed FBG was proposed for shape sensing, which depended on the different response of grating in outer cores on local bend and twist, which contributed to shape reconstruction [55].

In this chapter, torsion sensing experiments using the SCF-based sensor are described. The optical fiber torsion sensor is fabricated by introducing a taper structure on SCF, and the tapered SCF is spliced with SMF on both ends. Due to the reduced core pitch size, the coupling between cores is strengthened, and the corresponding coupling coefficient is highly dependent on the torsion applied on the taper. The torsion sensing experiment results show that the sensitivity increases with fiber twist, which can achieve as high as 1nm/°. In addition, rotation direction can be discriminated due to the opposite wavelength shift direction when the fiber is twisted in a clockwise and counterclockwise way. Then, batches of sensors are fabricated and then utilized for multiple torsion angle measurements in order to explain its accuracy performance. In theory, mode coupling in SCF and optical anisotropy theory are combined to discuss the tunable sensitivity performance.

4.2 Fabrication of optical fiber torsion sensor

The optical fiber torsion sensor is designed based on tapered SCF and two SMFs are spliced on both ends, which is shown in Fig. 4.1. The SCF (YOFC, China) owns cladding diameter of 150 μm, core diameter of 8 μm and core pitch size of 42 μm.

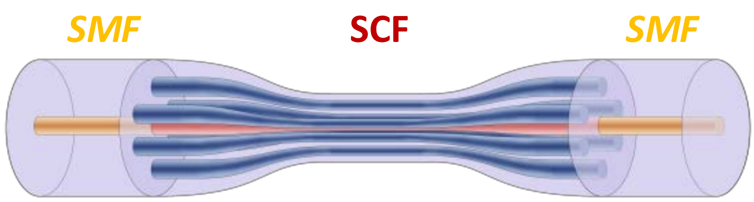

Fig. 4.1: Structure of optical fiber torsion sensor.

The taper is fabricated using CO_2 laser glass-processing machine (Fujikura, LZM-100), which is shown in Fig. 4.2. In LZM-100, both laser power and speed of motors under the left and right holders can be programmed. Thus, the size of taper on SCF, including transition length, waist diameter and length, can be optimized in order to obtain a desirable transmission spectrum for torsion sensing experiments.

During fabrication, the laser power is set firstly, and then ZL and ZR motor are confirmed with different speeds along a uniform direction, which contributes to taper structure fabrication. For the taper dimension, the waist diameter is decided by laser power while the lengths in transition and waist regions are dependent on the motor speed, V_1 and V_2. Typically, for standard taper fabrication, this LZM-100, can ensure the dimension deviation between the designed and fabricated to be within 5 μm.

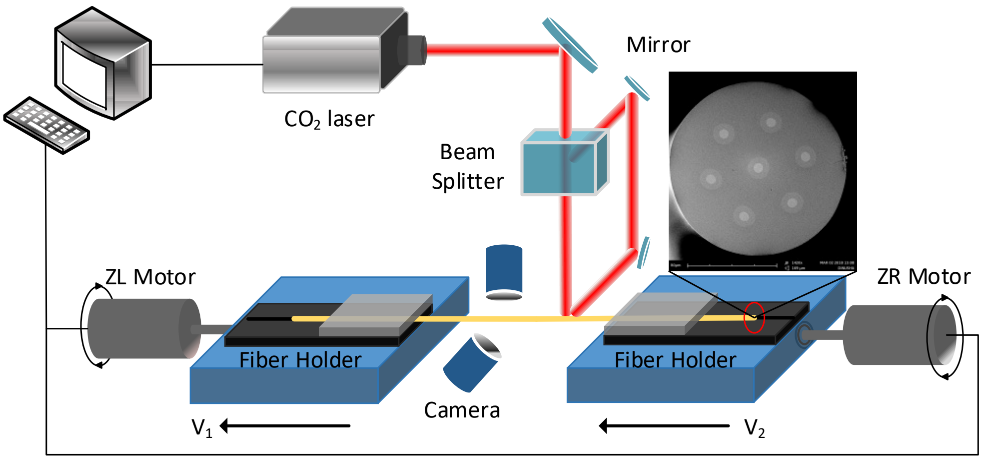

Fig. 4.2: Taper fabrication setup and process.

The taper is fabricated to strength the mode coupling between the central core and outer cores, which can be utilized for torsion sensing. To obtain a desirable optical transmission spectrum for the torsion experiment, the dimension of taper on SCF needs to be optimized. The spectrum is monitored by the setup of broadband light source (BLS) with range from 1250 nm to 1650 nm and optical spectrum analyzer (OSA, Yokogawa AQ6370D). For dimension optimization on taper structure, three parameters are taken into consideration: waist-length, waist-diameter and transition length [56]. To simplify the optimization and fabrication, we define the transition length to be 5 μm, which is a standard value for a common SMF taper design. Then, batches of tapered SCF with different waist lengths and diameters are fabricated and spliced with SMFs on both ends to monitor the transmission spectrum. For waist diameter optimization, the results are shown in Fig. 4.3. It can be seen that, with the diameter from 30 μm to 50 μm, the extinction ratio (ER) decreases from 12 dB to 5 dB, which agrees well with the theory that small core pitch size will strengthen the core-mode coupling. In the case of waist-length optimization, Figure 4.4 collects the corresponding spectrum. The spectral period decreases with the waist length. For taper waist fabrication, the requirement on short length will inevitably result in the large mismatch between designed and fabricated tapers. Thus, the length of waist here is confirmed to be 5 μm. On the other hand, for practical use of this optical fiber taper-based torsion sensor, a small waist diameter will weaken the taper strength. Therefore, the waist diameter is chosen to 30 μm. Since the coupling power between cores of SCF will affect the accuracy of further torsion sensing, the center-core alignment and splicing between SCF and SMF on both ends will be conducted before the taper fabrication.

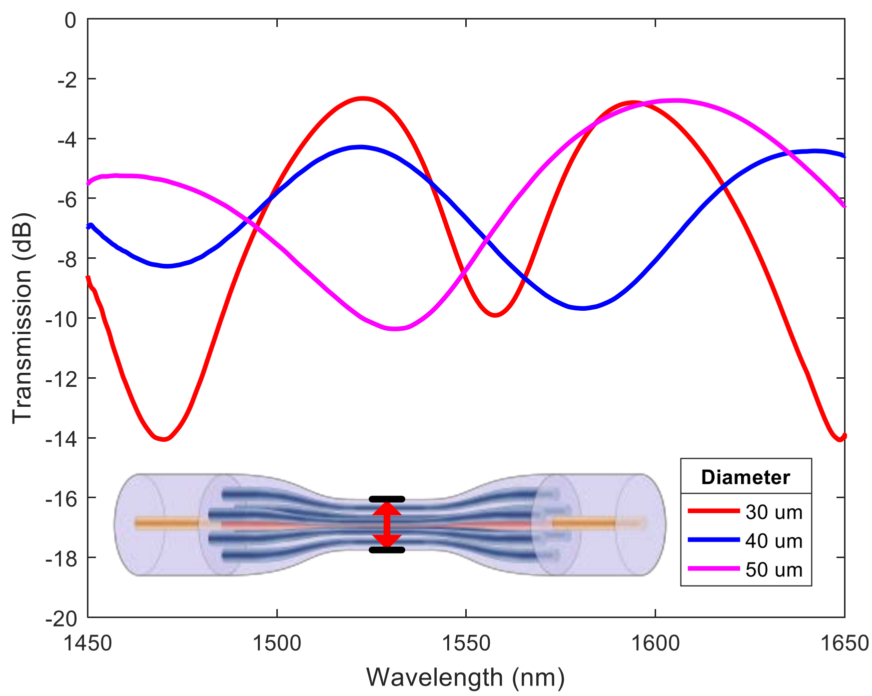

Fig. 4.3: Transmission spectra of torsion sensor under different waist diameters.

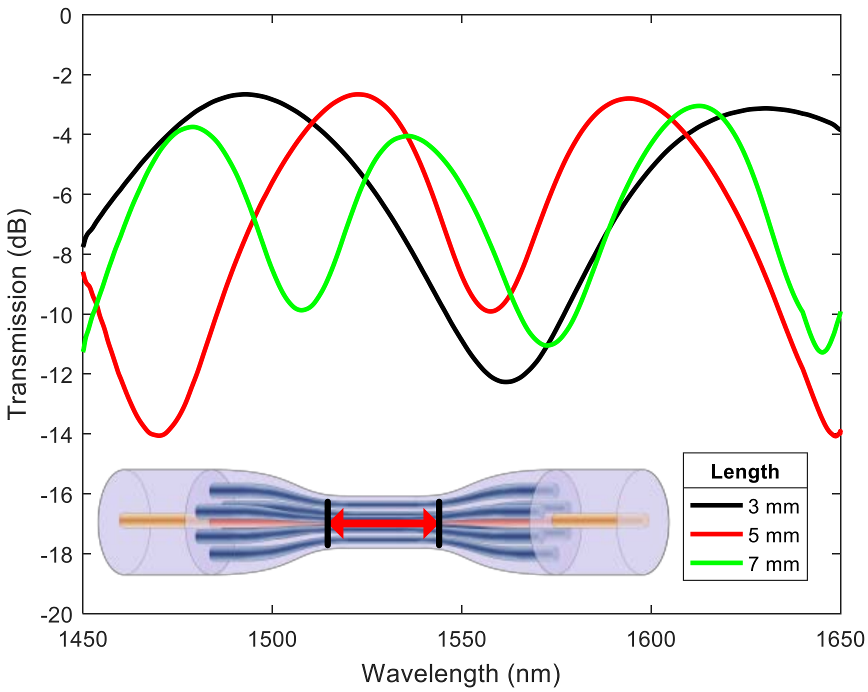

Fig. 4.4: Transmission spectra of torsion sensor under different waist lengths.

4.3 Experiment and results

The torsion sensing experimental setup is shown in Fig. 4.5. Two holders are used to rotate the sensors, in which the left holder is fixed while the right is controlled and rotated by programmed motors. The motor can rotate with a precision of 0.1°. The distance between the two holders is set to 30 mm in order to fully accommodate the tapered SCF. It is worth noted that two holders need precise axial alignment since any radial displacement may result in inaccurate data collection. Thus, prior to the experiment, two sections of SCF are placed on two holders, and the alignment is conducted with achieved alignment error under one micrometer. The practical alignment setup and the result are shown in Fig. 4.6. Then, the torsion sensor is placed between two holders. The final dimension of the torsion sensor is as shown in the inset of Fig. 4.5. The same BLS and OSA are used for spectrum monitoring and collecting under every torsion angle. The spectral range is selected from 1450 nm to 1650 nm and the resolution is set to 0.05 nm.

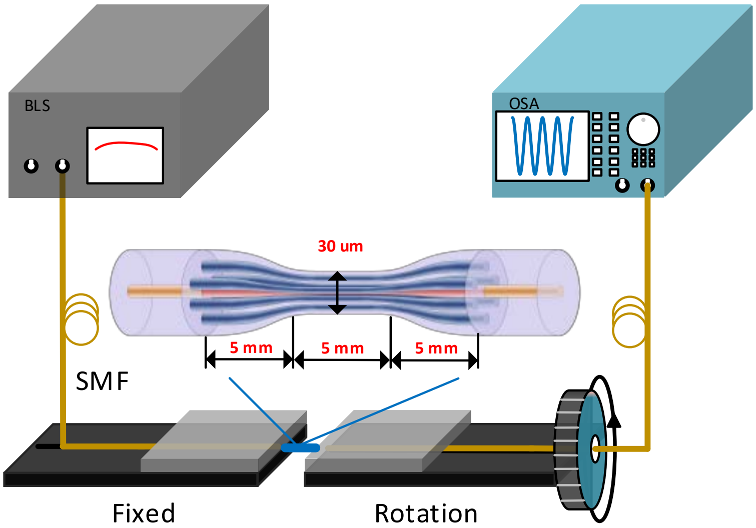

Fig. 4.5: Torsion sensing experimental setup.

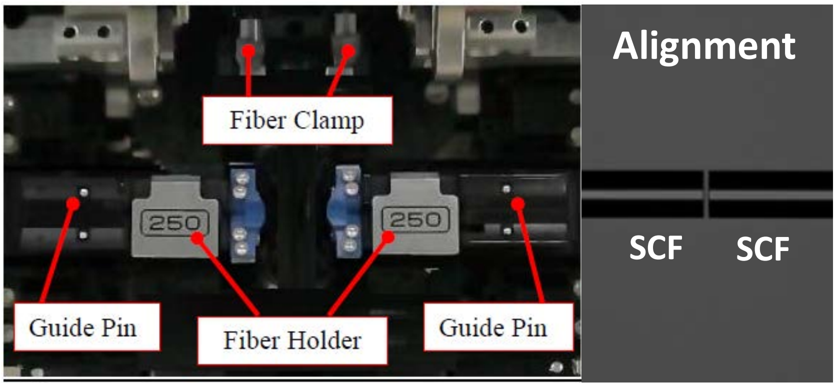

Fig. 4.6: Initial alignment between holders using SCF.

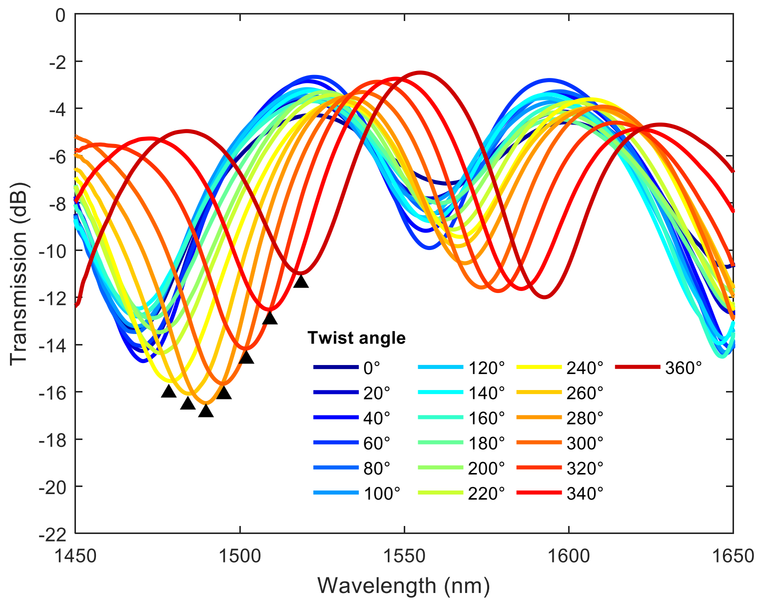

Fig. 4.7: Spectrum shift with fiber twist angles.

In the experiment, the right holder is rotated with the step of 20° from 0° to 900° and every spectrum is recorded. The spectra collected from 0° to 360° are shown in Fig. 4.7, where the spectrum shows red shift with twist angle. Then, one dip is chosen, as labeled in Fig. 4.7, and these monitored wavelengths are summarized in Fig. 4.8. It can be seen that, with fiber twist, wavelength shifts non-linearly. Under identical torsion angle increment, the amount of wavelength shift increases, meaning that the sensitivity increases with torsion angles. To discuss the sensitivity in detail, we collect all the spectra and compare them as follows. It is also worth mentioned that the curve fitting here is just the first attempt to show the trend of wavelength shift with torsion angle and the detailed discussion about this will be presented in the discussion section. Thus, it is acceptable that this fitting method may not work well in part of the sensing region such as the region from 0° to 150°.

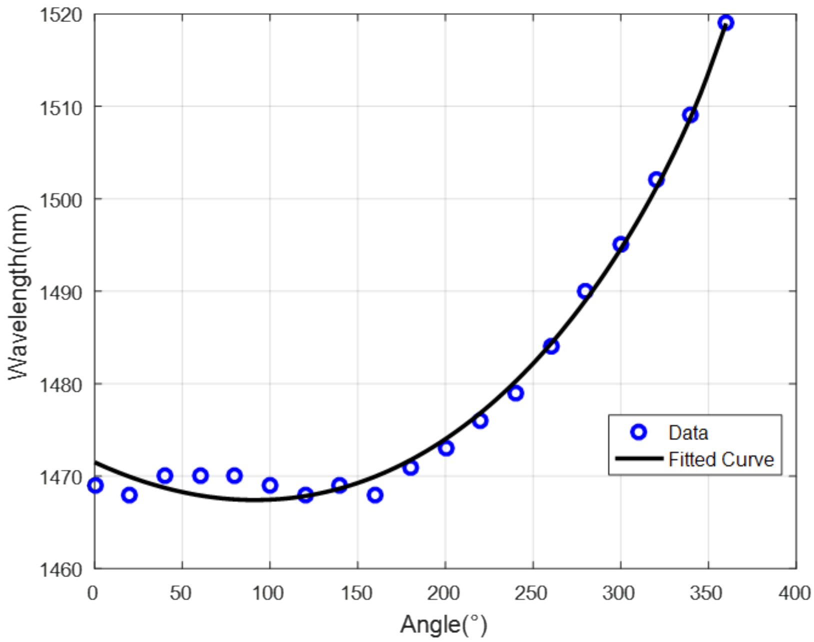

Fig. 4.8: Dip wavelength value collection under different twist angles.

4.3.1 Tunable sensitivity

Although the spectrum shifts non-linearly with fiber twist, to analyze the sensitivity performance in a wide range of twist angles, we assume the linear relationship between wavelength shift amount and twist angle within a small range. Based on that, three twist angle regions are divided with an identical range of 90° and different pre-twist angles of 160°, 360°, and 560° respectively. The spectra collected in these three regions are shown as Fig. 4.9. It can be seen that, under the same twist angle increment of 60°, the amount of wavelength shift is different and increases with the pre-twist angle, which can be illustrated by the purple arrows in Fig. 4.9. Then, based on the spectra collected, the sensitivities in all regions with different pre-twist angles can be calculated, and the results are summarized as Fig. 4.10. It can be seen that, with fiber twist angle from 0° to 900°, sensitivity increases and can achieve as high as 1.00nm/°. The inset of Fig. 4.10 illustrates the curve fitting to obtain the sensitivity. Therefore, the sensitivity of this torsion sensor can be tuned by pre-twisting the tapered SCF into different angles.

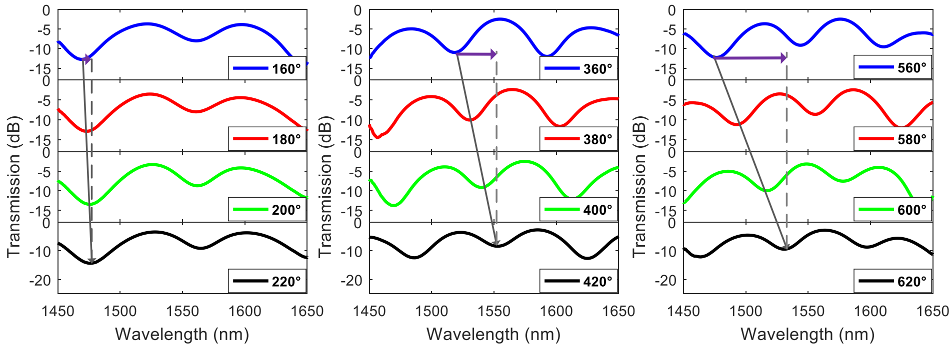

Fig. 4.9: Wavelength shift in transmission spectra when the sensor is rotated with pre-twisting angle of 160°, 360°, and 560°.

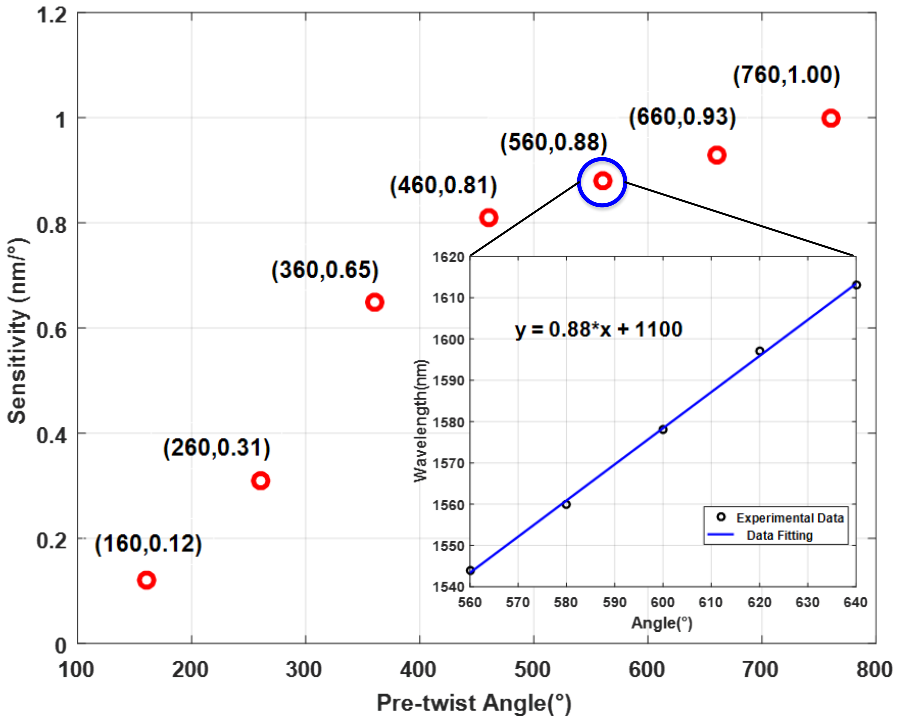

Fig. 4.10: Sensitivities of the torsion sensor in measurement ranges with different pre-twisting angles.

4.3.2 Discrimination of twisting direction

The ability to discriminate the twisting direction has always been one of the significant concerns of torsion sensors. To investigate whether this kind of optical fiber torsion sensor is capable of telling the rotation direction via spectrum monitoring, the tapered SCF, fabricated following aforementioned dimension, is initially twisted to 360° and then rotated to 540° in the clockwise (C.W) direction and 180° in the counter-clockwise (C.C.W) direction, respectively. This corresponds to 2π *rad* in total. The wavelength shift results are shown in Fig. 4.11. It can be seen that the spectrum exhibits red-shift in C.W and blue-shift in C.C.W direction, even though the sensitivity is different. To conclude, this kind of optical fiber torsion sensor can discriminate twisting direction by monitoring the wavelength shift direction.

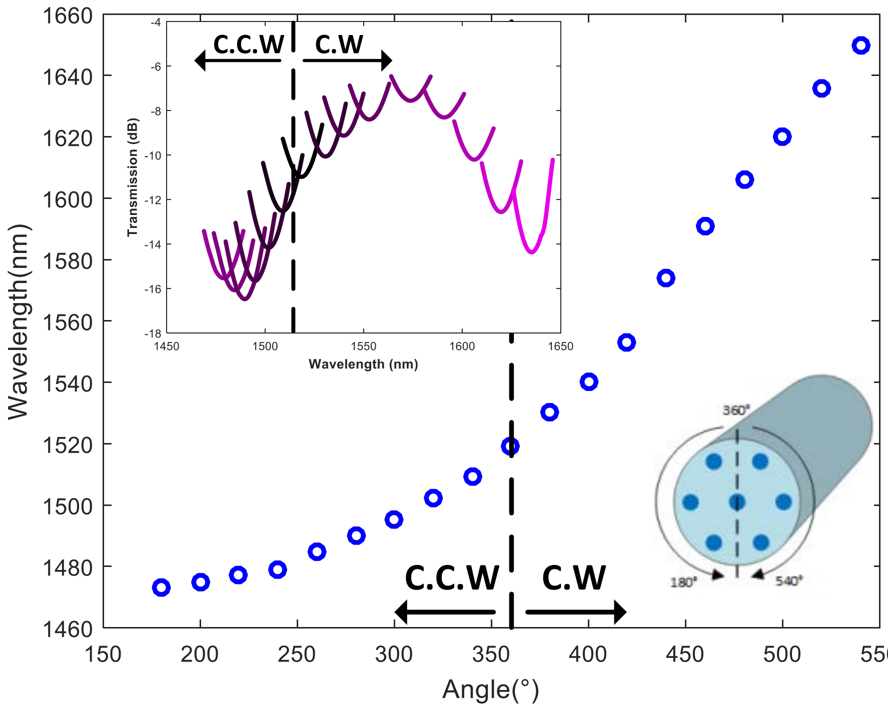

Fig. 4.11: Wavelength shift results when the tapered SCF is twisted in the clockwise (C.W) and counter-clockwise (C.C.W) direction.

4.3.3 Repeatability

Stability, as one of the parameters to access the performance of sensors, also needs discussion to demonstrate its feasibility. Thus, to obtain the stability of this optical fiber torsion sensors, batches of sensors are fabricated. The fabrication still follows the aforementioned dimensions with waist-length of 5 mm, transition-length of 5 mm and waist-diameter of 30 μm. The experiments include two parts: repeated angle measurements using one torsion sensor while batches of sensors for the same torsion angle measurement. Thus, one torsion sensor is fabricated firstly and used in twist angle measurement for three times. The wavelength monitoring results during twisting are shown in Fig. 4.12 (a). On the other hand, three sensors are fabricated and used to measure the same angle change individually, the results of which are summarized in Fig. 4.12 (b). It can be seen that, for both wavelength shift results, the maximum error is 2 nm under the twist angle around 520°, which means that the performance of this optical fiber torsion sensor is stable only if it follows the same dimension. In addition, according to the sensitivity collected in Fig. 4.10, the accuracy can be obtained as ±1° with the sensitivity of 0.85 nm/°, which demonstrates that this optical fiber torsion sensor is desirable for accurate twist angle measurement.

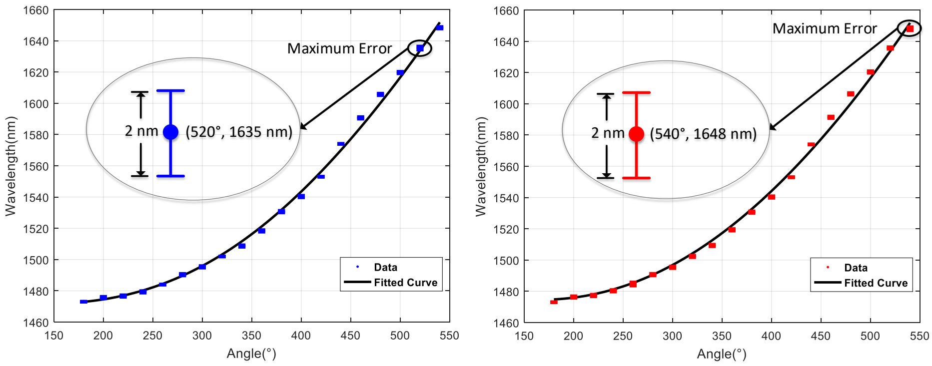

Fig. 4.12: Wavelength shift results in (a) repeating the torsion measurement using one sensor and (b) using three torsion sensors with the same taper dimension.

4.4 Discussion

4.4.1 Trench-assisted SCF and mode coupling dynamics

MCF has been considered as a standard candidate for the SDM system by employing multiple cores as transmission channels to increase the capacity. However, these channels are not perfect independent of each other, especially when the cores are close to each other, which will result in the power coupling between cores. This kind of core-mode coupling will introduce crosstalks of signals thus degrades the transmission performance. To overcome this drawback, many schemes are proposed, one of which focuses on the MCF design, such as heterogeneous MCF with non-identical cores to realize long-haul transmission with low crosstalk. Another scheme is the trench-assisted structure around every core [57]. The RI of trench is even lower than that of cladding. The schematic diagram of trench assisted MCF (TA-MCF) is shown in Fig. 4.13. This TA-MCF owns low-crosstalk between cores and large effective mode area in the case of high-density cores, which makes it an ideal candidate for SDM transmission.

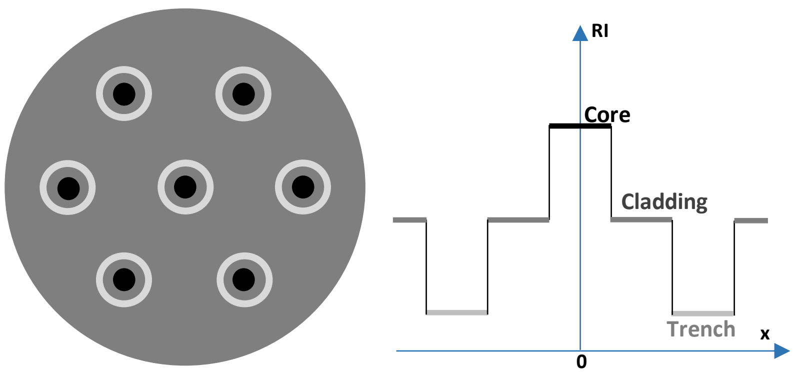

Fig. 4.13: Schematic diagram of TA-MCF and RI profile.

Based on the coupled-mode theory, the coupling between core-modes can be represented by coupling coefficient C. In TA-MCF, the crosstalk characterization between cores has been explored and the coupling coefficient $C_{p,q}$ can be expressed as follows [58]:

$$C_{p,q} = \frac{k(n_p^2 - n_{cl}^2)W_{1-p}U_{1-q}L_q\sqrt{\dfrac{\pi a_{1-q}}{2W_{1-q}D}}\exp(-W_{1-q}\dfrac{D}{a_{1-q}})}{\sqrt{n_p n_q}\,a_{1-p}a_{1-q}V_{1-p}V_{1-q}J_1(U_{1-p})J_2(U_{1-q})}\cdot \tag{4.1}$$
$$\int_0^{a_{1-p}} J_0(U_{1-p}\frac{r}{a_{1-p}})I_0[(\frac{W_{1-q}}{a_{1-q}} - \frac{P_2 - P_1 + Y_2 - Y_1}{D-r})r]\exp[\frac{(P_2 - P_1 + Y_2 - Y_1)D}{D-r}]rdr,$$

where $k=2\pi/\lambda$ is the wave number; D is the pitch size between cores; P and Y are the parameters related to the ratio between core diameter and pitch size; p and q represent two coupled cores and n_p, n_q, n_{cl} represent RI of core p, core q and cladding. It can be seen that the coupling coefficient is mostly related to the RI of cores. Change of core RI in MCF will affect the coupling between cores and then result in the output intensity variation, which can be utilized for optical fiber sensing.

For MCF, core-mode coupling dynamic is widely investigated aiming to optimize the multi-input-multi-output strategies for the SDM system. For SCF, the mode coupling dynamics is analyzed, and coupled-mode formalism is developed. For example, in SCF, due to core-mode coupling, the output intensity I of the center core and outer cores at propagation distance z can be expressed as Eq. (4.2) and Eq. (4.3), respectively.

$$I(z) = \frac{1}{7} + \frac{6}{7}\cos^2(\sqrt{7}Cz) \tag{4.2}$$

$$I(z) = \frac{1}{7}\sin^2(\sqrt{7}Cz) \tag{4.3}$$

It can be seen that the output intensity shows an oscillation relationship with the coupling coefficient C and propagation distance z. From Eq. (4.1), the coupling coefficient is dependent on transmission wavelength and RI of cores. Thus, on the one hand, under certain distance, the output intensity oscillates with wavelength, which is in accordance with the spectrum obtained experimentally (Fig. 4.3). On the other hand, any change of RI of core, including center core and outer cores, will result in the subsequent shift of coupling coefficient *C*. Eventually, the spectrum will shift with RI change, which is the basis of torsion sensing in principle.

4.4.2 Optical anisotropy in twisted optical fiber

For optical fiber, the index ellipsoid can be expressed by Eq. (4.4) using physical optics theory [59].

$$B_{ij}X_iY_j = 1 \tag{4.4}$$

In Eq. (4.4), *B* is the coefficient of optical indicatrix in optical fiber and X_i and X_j represent three axes, namely *X, Y* and *Z*. Commonly, the undisturbed optical fiber can be considered as an isotropy, homogeneous and transparent medium. Thus, it has a spherical indicatrix, following Eq. (4.5):

$$B(x^2 + y^2 + z^2) = 1, \tag{4.5}$$

where

$$B = n^{-2}. \tag{4.6}$$

However, under ambiance stress, like torsion and bending, this spherical status will be broken, and the coefficient *B* will update, which can be calculated based on photo-elastic effect. As is well known, the stress can be characterized by a second-rank tensor [σ_i, i = 1, 2, …6], where six components are independent of each other. The optical-strain, or photo-elastic effect, can be described by the equation as follows:

$$\Delta B_i = p_{ij}\sigma_j, \tag{4.7}$$

where ΔB_i is a symmetric second-rank tensor with six components, which represents the change of coefficient *B* under applied stress. p_{ij} is the stress-optical tensor, which is a fourth-rank tensor with 36 components. Due to the intrinsic isotropy of optical fiber, p_{ij} can be fully characterized by two parameters, p_{11} and p_{12}. Thus, the stress-optical tensor [p] in optical fiber can be expressed as follows [60].

$$[p]=\begin{bmatrix} p_{11} & p_{12} & p_{12} & 0 & 0 & 0 \\ p_{12} & p_{11} & p_{12} & 0 & 0 & 0 \\ p_{12} & p_{12} & p_{11} & 0 & 0 & 0 \\ 0 & 0 & 0 & p_{11}-p_{12} & 0 & 0 \\ 0 & 0 & 0 & 0 & p_{11}-p_{12} & 0 \\ 0 & 0 & 0 & 0 & 0 & p_{11}-p_{12} \end{bmatrix} \quad (4.8)$$

When the optical fiber is under torsion along the longitudinal direction, shearing stress on both ends is generated. On one end of optical fiber, this shearing stress can be decomposed into two directions, x and y, which is shown as Fig. 4.14.

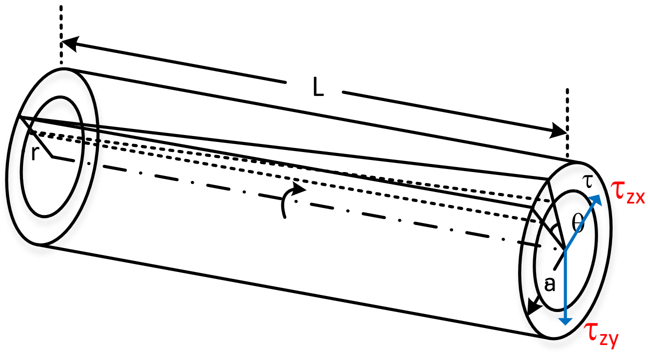

Fig. 4.14: Schematic diagram of twisted optical fiber for shearing stress analysis.

In twisted optical fiber, six components in the stress tensor will be updated as follows:

$$\begin{aligned} &\sigma_1 = \sigma_2 = \sigma_3 = \sigma_6 = 0; \\ &\sigma_4 = \mu\tau x; \sigma_5 = -\mu\tau y;, \end{aligned} \quad (4.9)$$

where τ is the torsion ratio, which can be described as $d\theta/dL$, and μ is the shearing modulus. Thus, according to Eq. (4.9) and Eq. (4.8), six components in coefficient ΔB_i in Eq. (4.7) can be obtained using following equation.

$$\begin{bmatrix} \Delta B_1 \\ \Delta B_2 \\ \Delta B_3 \\ \Delta B_4 \\ \Delta B_5 \\ \Delta B_6 \end{bmatrix} = \begin{bmatrix} p_{11} & p_{12} & p_{12} & 0 & 0 & 0 \\ p_{12} & p_{11} & p_{12} & 0 & 0 & 0 \\ p_{12} & p_{12} & p_{11} & 0 & 0 & 0 \\ 0 & 0 & 0 & p_{11}-p_{12} & 0 & 0 \\ 0 & 0 & 0 & 0 & p_{11}-p_{12} & 0 \\ 0 & 0 & 0 & 0 & 0 & p_{11}-p_{12} \end{bmatrix} \begin{bmatrix} 0 \\ 0 \\ 0 \\ \mu\tau x \\ -\mu\tau y \\ 0 \end{bmatrix} \tag{4.10}$$

Then, ΔB_i can be summarized as following Eq. (4.11).

$$\begin{aligned} &\Delta B_1 = \Delta B_2 = \Delta B_3 = \Delta B_6 = 0; \\ &\Delta B_4 = (p_{11} - p_{12})\tau\mu x; \Delta B_5 = -(p_{11} - p_{12})\tau\mu y \end{aligned}, \tag{4.11}$$

Thus, the updated coefficient B can be expressed as follows.

$$\left[B\right] = \begin{bmatrix} n_{co}^{-2} & 0 & -y\mu\tau(p_{11} - p_{12}) \\ 0 & n_{co}^{-2} & x\mu\tau(p_{11} - p_{12}) \\ -y\mu\tau(p_{11} - p_{12}) & x\mu\tau(p_{11} - p_{12}) & n_{co}^{-2} \end{bmatrix} \tag{4.12}$$

It can be seen that, the torsion, or shearing stress, will make the coefficient nondiagonal. The new three principle axes can be obtained by diagonalizing the updated tensor B. As a result, three coefficients under new axes can be obtained using eigenvalues of updated B. The obtained coefficient B are as follows:

$$\begin{aligned} &B_1 = n^{-2}; \\ &B_2 = n^{-2} - r\mu\tau\Delta p / 2;, \\ &B_3 = n^{-2} + r\mu\tau\Delta p / 2; \end{aligned} \tag{4.13}$$

where n is the RI, r is the radial distance, namely core and cladding pitch size, P_{11}-P_{12} is substituted by Δp for simplification in later expressions. Based on the relationship between B and n in Eq. (4.6). RI of three principle axes in index ellipsoid can be obtained as follows:

$$\begin{aligned} &n_1 = n; \\ &n_2 = n - n^3 r\mu\tau\Delta p / 2;. \\ &n_3 = n + n^3 r\mu\tau\Delta p / 2; \end{aligned} \tag{4.14}$$

It can be seen that, for twisted optical fiber, in radial direction, RI will experience change in three principle axis, or polarization states. This will apply on the SCF and help to analyze the torsion induced coupling change between center core and outer cores.

4.4.3 Sensitivity analysis of SCF-based torsion sensor

For the torsion sensor based on SCF in this chapter, the fiber used is trench assisted SCF (TA-SCF), and the taper structure is introduced to strengthen the coupling between center core and six surrounding cores. Thanks to the trench structure, the tapered SCF owns strong as well as stable coupling, which is sensitive to RI change of cores. Based on the optical anisotropy theory introduced above, the torsion will induce RI change in two polarization states. For SCF, to simplify the analysis, we assume that surrounding cores experience RI change while RI of center core remains unchanged due to the large ratio between core pitch size and core radius. Therefore, based on Eq. (4.14), for surrounding cores, the RI change can be expressed as follows:

$$\begin{aligned} n_\alpha &= n_{co} + \Delta p \cdot \theta \cdot r \cdot \mu \cdot n_{cl}^3 / 2L; \\ n_\beta &= n_{co} - \Delta p \cdot \theta \cdot r \cdot \mu \cdot n_{cl}^3 / 2L;' \end{aligned} \tag{4.15}$$

where α and β represent two polarization states, n_{co} is the RI of surrounding cores, θ is the torsion angle, r is the radius distance, n_{cl} is the RI of cladding, L is the length of tapered SCF. Since the surrounding cores in twisted SCF experience RI change in two polarization states α and β, core-mode coupling in SCF can be divided into two groups: group A which represents coupling between outer core-mode in α polarization state and center core-mode and group B represents the coupling between outer core-mode in β polarization state and center core-mode, which is shown in Fig. 4.15.

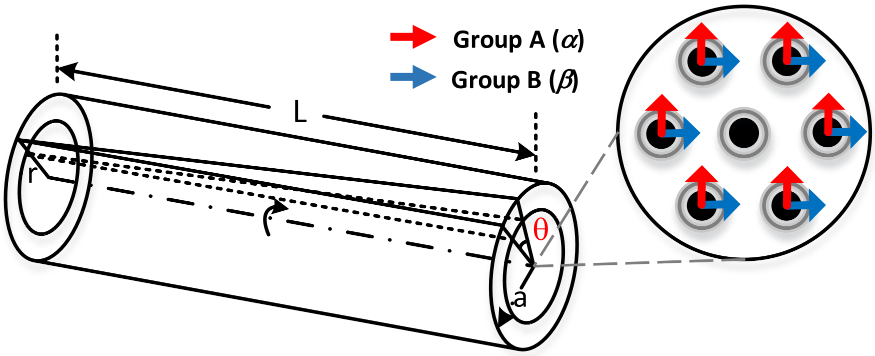

Fig. 4.15: Two kinds of core-mode coupling in twisted SCF: Group A and B.

Based on the mode coupling dynamics introduced above, for torsion sensor based on SMF-SCF-SMF shown in Fig. 4.1, center core can be selected as the output. Thus, the output intensity can be expressed as Eq. (4.2). Due to the orthogonality of two polarization states, two kinds of core-mode coupling can be calculated separately, and the total output intensity is the sum of Group A and B, and it can be expressed as follows:

$$I(z)=I_\alpha(z)+I_\beta(z)=\frac{2}{7}+\frac{6}{7}[\cos^2(\sqrt{7}C_\alpha z)+\cos^2(\sqrt{7}C_\beta z)]\approx\frac{6}{7}\cos[\sqrt{7}(C_\alpha+C_\beta)z]+\frac{8}{7}, \quad (4.16)$$

where I_α and I_β are the individual output intensity through coupling between center core and polarization state α, β in outer cores, C_α and C_β are the corresponding coupling coefficients. Since the coupling coefficient C is dependent on RI, and outer cores experience RI change in the opposite direction, the coupling in twisted SCF will change dramatically with torsion angle.

For spectrum analysis, during the torsion sensing experiment, one dip in the spectrum is selected, and the corresponding wavelength is monitored with fiber twists. Based on Eq. (4.16), for m^{th} dip, the wavelength follows the equation:

$$[C_\alpha(\lambda_m)+C_\beta(\lambda_m)]z'=(2m+1)\pi, \quad (4.17)$$

where λ_m is the monitored dip wavelength, z' is the substitution of $\sqrt{7}z$ for simplified expressions later. To obtain C_α and C_β in a simple way, based on Eq. (4.1), C can be simplified as $kn^{3/2}{}_{\alpha,\beta}$. Then, the monitored wavelength satisfies:

$$\lambda_m = \frac{2z'}{2m+1}(n_\alpha^{3/2} + n_\beta^{3/2}). \tag{4.18}$$

Then, the derivative of λ_m with respect to θ is performed for sensitivity analysis. Thus, Eq. (4.18) with derivative on both ends evolves as follows:

$$\frac{d\lambda_m}{d\theta} = \frac{2z'}{2m+1} \cdot \frac{3}{2}(\sqrt{n_\alpha}\frac{dn_\alpha}{d\theta} + \sqrt{n_\beta}\frac{dn_\beta}{d\theta}). \tag{4.19}$$

Since the change of RI under torsion in twist optical fiber is small, we assume $n_\alpha = n_\beta$. Based on Eq. (4.15), the sensitivity can be eventually obtained as follows:

$$\frac{d\lambda_m}{d\theta} \approx \frac{3\sqrt{2}z'}{2m+1}(\Delta p \cdot r \cdot \mu \cdot \frac{n_{cl}^3}{2L})^{3/2} \cdot \sqrt{\theta}, \tag{4.20}$$

where z', m, Δp, r, μ, L, n_{cl} is introduced above and also remains unchanged with fiber twist. Eq. (4.20) reveals that the sensitivity increases with fiber twist angle, and the sensitivity is proportional to the root square of the torsion angle. Based on the summarized sensitivities shown in Fig. 4.10, curve fitting is performed to estimate the relationship between the sensitivity and torsion angle, the result of which is shown in Fig. 4.11. It can be seen that the obtained curve fitting equation agrees well with Eq. (4.20). Thus, it is demonstrated that the mode coupling dynamics as well as optical anisotropy theory in SCF can successfully explain the sensitivity performance of this torsion sensor. Also, it can also be understood that when high-level tension is applied to the twist region, the SCF will be more sensitive to additional torsion.

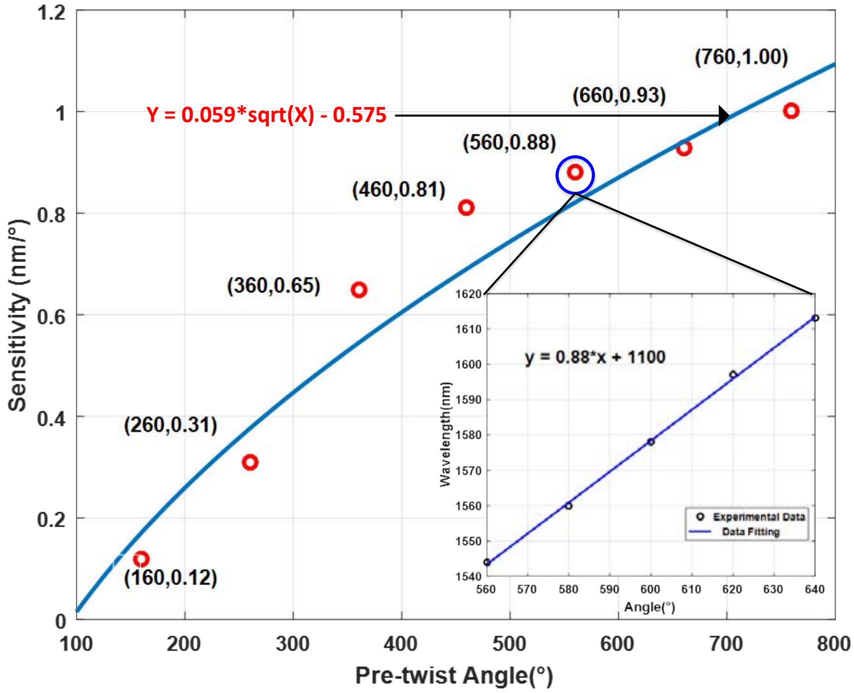

Fig. 4.16: Curve fitting on sensitivity with respect to pre-twist angle.

To estimate the range of application of Eq. (4.20) in a quantitative way, specific value of every parameter is collected. For example, the common RI change δn induced by torsion for twisted optical fibers is 10^{-4}-10^{-5}. This also help with the above assumption $n_\alpha \approx n_\beta$. Based on the dimension of SCF and its based torsion sensor, $r=42\ \mu m$, $L=30\ mm$, $n_{cl}{\sim}1.444$ [61]. Typical value regarding torsion on optical fibers: $\Delta q{\sim}10^{-11}\ m^2/N$, $\mu{\sim}2{\cdot}10^6\ N/m^2$. Therefore, substituting all of them on Eq. (3.20), the torsion range $\delta\theta$ is 200°-2000°, which demonstrates that with the torsion angle from 200° to 2000°, the sensitivity performance will follow Eq. (4.20) or Fig. 4.11. This agrees well with the experimental results. From Fig. 4.11, the torsion sensor based on tapered SCF can achieve tunable sensitivity from 0.12 nm/° to 1.00 nm/° under the pre-twist angle from 160° to 760°. This performance can be explained using mode coupling dynamics as well as optical isotropy theory in twisted optical fiber. For practical application, based on different requirements on sensitivity, the torsion sensor can be pre-twisted to corresponding angles following Eq. (4.20).

In summary, this kind of torsion sensor owns many excellent advantages such as easy fabrication, low-cost, tunable sensitivity in a large range, the capability for discriminating the rotation direction and stable performance. As mentioned in the introduction of this chapter, there are various optical fiber torsion sensors based on different specialty optical fibers, such as suspended twin-core fiber and SI interferometers. In terms of twist range, sensitivity, ease of fabrication and mechanical strength, the comparison between tapered SCF and other schemes is shown in Table 4.1. For the practical deployment of sensors, environmental factors, such as ambient temperature, should be considered. For our torsion sensor, in the taper region, the optical energy in the cladding area is strong, which makes the sensor sensitive to ambience, such as temperature. Thus, this torsion sensor may work well in the stable environment, which is also the limitation for practical applications. Or, a specific transducer can be designed to protect the torsion sensor from ambience variation.

Table 4.1 Comparisons between tapered SCF and other torsion sensing schemes

Type	Sensitivity	Range	Mechanical strength	Ease of fabrication	Direction Discrimination
Our sensor	0.12-1.00 nm/°	160°-940°	High	Easy	Yes
LPG	2.80 nm/°	0°-160°	High	Hard	No
SI	3.25 nm/°	180°-270°	Medium	Normal	No
Helical MCF	3.90 nm/°	0°-180°	Low	Hard	Yes
FBG-PDL [62]	0.955 dB/rad	0°-180°	Medium	Normal	-
Suspended-TCF [63]	$1.2 \cdot 10^{-2}$ dB/°	0°-90°	Medium	Hard	-

4.5 Summary

In this chapter, the application of MCF on torsion sensing is introduced. The torsion sensor is based on conventional sandwich structure: SMF-MCF-SMF. The MCF used here is SCF with trench assisted. Tapered structure is fabricated on SCF to strengthen coupling between center-core and outer-cores. For the taper dimension, both length and diameter of the waist are optimized experimentally. The taper on SCF is confirmed with transition length, waist diameter and waist length of 5 mm, 30 μm and 5 mm. Based on this, tapered SCF is fabricated and the torsion sensing experiment is performed. The results show that the spectrum shows red shift with torsion angles. For further discussion, with the torsion angle from 100° to 900°, sensitivity increases from 0.12 nm/° to 1.00 nm/°, which means that the sensitivity is tunable with different pre-twist angles. Then, rotation direction is demonstrated to be discriminated by monitoring the wavelength shift direction. The stability performance is also discussed through repeated experiments and the accuracy can achieve ±1°.

In theory, the mode coupling dynamics in SCF is introduced, including the mode coupling coefficient and output intensity from the center core in SCF. In addition, optical anisotropy in twisted optical fiber is analyzed in detail and then applied to SCF for discussion on sensitivity performance. The simulation results agree with the experiments, which demonstrates the feasibility of this theoretical analysis on sensitivity performance. At last, a comparison between tapered SCF-based torsion sensor and other schemes is shown to highlight the advantages in terms of torsion range, sensitivity, rotation direction discrimination and mechanical strength. To conclude, SCF can be a promising candidate for torsion sensing applications such as structural health monitoring and robotics, and MCF also shows its potential in the optical fiber sensing community.

5 Non-invasive vital signs monitoring based on FMF and MCF sensors

In chapter 3 and 4, the mode interference in FMF and core-mode coupling in MCF are utilized for temperature and torsion sensing and they show excellent performance. Thus, the interaction between modes in FMF or cores in MCF can be potentially used for more sensing applications. Chapter 5 shows the application of MCF and FMF sensors on non-invasive vital signs monitoring, including respiration and heartbeat. Firstly, a twin-core fiber-based sensor for vital signs monitoring is introduced. The sensor structure, experimental setup and vital signs monitoring results are presented, and supermode interference within the twin-core fiber is utilized for curvature sensing. Then, in-line optical fiber interferometers using SCF and FMF for vital signs monitoring are introduced.

5.1 Introduction

5.1.1 Vital signs monitoring

The worldwide aging population, one of the current social crises, places a heavy burden on individuals and the society in terms of caregiving and medical expenses. With the corresponding change of modern medicine trends from treatment to prevention, daily assessment and monitoring of the health condition for the elderly become necessary to prevent and control disease development, especially some chronic and senile diseases [64]. Vital signs, such as respiration, heartbeat, body temperature and blood pressure, are the main health indications of human body functions, which are shown in Fig. 5.1 [65]. Good monitoring of basic vital signs can help to assess the physical health condition or even identify specific diseases in the early stage [66]. Thus, vital signs monitoring for aging people becomes promising and urgent for the health trend analysis and disease prevention. It is worth noted that, according to the world market report of telehealth, chronic obstructive pulmonary disease (COPD) and congestive heart failure (CHF) occupy 49% and 12% among senile diseases, indicating the importance of respiration and heartbeat monitoring. Respiration rate (RR) is a critical vital sign reflecting the physiological function of lungs: inflowing of oxygen and removal of carbon dioxide, and abnormal RR is directly related to many symptoms like asthma and anemia. Heart rate (HR) represents the cardiac cycles from pumping newly oxygenated blood to pulling back deoxygenated blood through the whole body [67], and it is widely used to assess human physical and mental states [68]. Measurement of these two parameters is the main focus of the current vital signs monitoring.

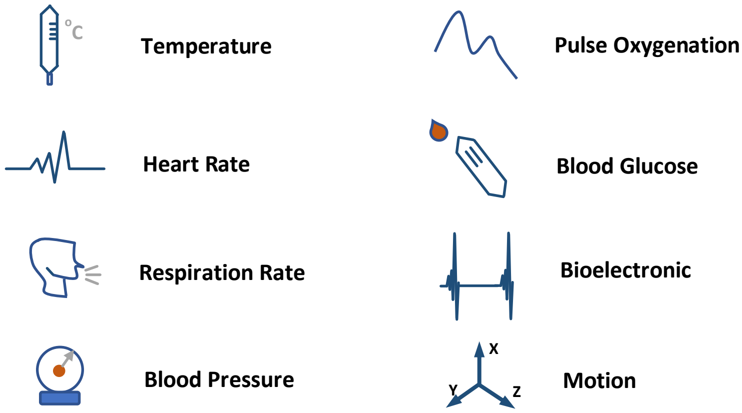

Fig. 5.1: Human basic vital signs.

5.1.2 Wearable devices for vital signs monitoring

One of the most popular vital signs monitoring techniques is wearable devices, and various sensing schemes are utilized for such monitoring purposes [69]. Currently, for HR monitoring, there are three main sensing techniques, which are based on electrical, optical and pressure signals. Electrocardiography (ECG) is used to assess the human cardiovascular system via electrical signal picked from heart muscles, and HR can be obtained from the R wave-to-R wave (R-R) interval of ECG signal. Conventional ECG data acquisition requires 12 leads attached to the skin [70] while currently developed techniques only need two electrodes in a band-aid form [65]. The method using optical [71] and pressure [72] sensors for HR measurement is called plethysmography, which is based on the distention of arteries and arterioles in the subcutaneous tissue due to heart pumping blood. The light-emitting diode and photodetector used in optical sensors capture the light absorption peaks [73] to obtain HR by calculating the interval between two systolic peaks while pressure sensors pick up the pulse signals in the same way to calculate HR [74]. For RR measurement, sensors can respond in two ways: expansion and contraction of the chest during breathing and flow of breath. Many conductive and dielectric materials are sandwiched between substrates wrapped tightly around the body, which can detect the chest movement to obtain RR [75]. For breath flow detection, the temperature sensors placed near the nose together with the acoustic sensors on the neck can measure RR with high accuracy [76,77]. In summary, the primary advantages of these wearable devices are the capability for continuous vital signs monitoring during normal daily life and also the data can be acquired in any circumstances, which provides an opportunity for pneumonic and cardiovascular performance assessment under various settings. However, all these sensing schemes, regardless of HR or RR monitoring, require close contact with the body, which is conspicuous and also inevitably discomforts the users, especially the elderly. Moreover, to monitor HR and RR simultaneously, more than one sensor has to be employed and placed in different locations of the body, which is not convenient and user-friendly. The summary of wearable sensors for respiration and heartbeat is shown as Fig. 5.2.

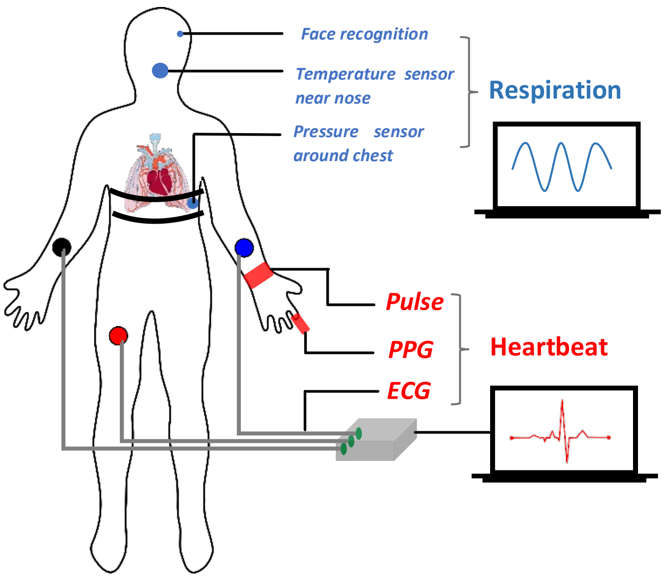

Fig. 5.2: Wearable sensors for heartbeat and respiration monitoring.

5.1.3 Non-invasive vital signs monitoring

To overcome the drawbacks of wearable devices mentioned above, non-invasive vital signs monitoring techniques are desirable and have drawn much attention from researchers with various backgrounds. Different sensing schemes are proposed in recent years. For example, in 2018, Liu et al. proposed to track vital signs by using existing off-the-shelf Wi-Fi signals and developed algorithms making use of the channel information in both time and frequency domain to estimate both HR and RR during sleeping, which is shown in Fig. 5.3 [78]. Another reported wireless sensing scheme is Doppler radar. Nosrati et al. realized vital signs monitoring in a short range by using a concurrent dual-beam phased-array Doppler radar and MIMO beamforming technique [79]. In addition, the near-field coherent sensing method was proposed for the first time for vital signs monitoring. It only required passive tags placed at the chest and wrist area, retrieving not only HR and RR but also blood pressure and breath effort through the collected multiplexed far-field backscattering waveforms [80]. These non-invasive vital signs monitoring schemes are comfortable to the users and superior to most wearable devices. However, these systems or techniques are complex and costly, which are not ideal for practical applications, especially daily monitoring. On the other hand, the signal detection is somewhat limited to space and distance, resulting in unstable performance in long-term services.

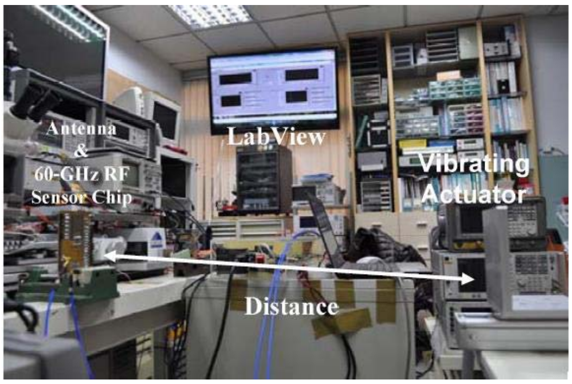

Fig. 5.3: Wi-Fi signal based vital signs monitoring system.

5.1.4 Optical fiber vital signs monitors

Optical fiber sensors, owing to the advantages of highly sensitive, low cost, lightweight, flexible and stable, have been used in a wide range of applications, including vital signs monitoring. Optical fiber sensors for breath monitoring is to detect the pressure change induced by movement of chest when breathing on the bed while HR is based on the Ballistocardiogram (BCG) characterization, which is the recoil forces of the body in reaction to cardiac ejection of blood into the vasculature [81]. The standard BCG waveform is shown in Fig. 5.4. The pressure changes and body movement are directly related to RR and HR and can be detected simultaneously as well as non-invasively by optical fiber sensors embedded in a mattress. One kind of optical fiber sensors proposed recently utilized the amplified bending loss in optical fibers induced by breath and heartbeat [82]. This sensing scheme can realize HR and RR monitoring, but the fabrication possess is very complicated, and the sensitivity is too low to realize accurate vital signs measurement, especially BCG signals.

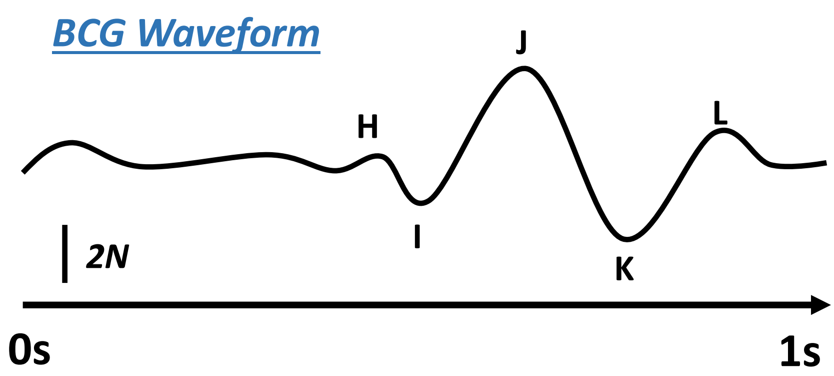

Fig. 5.4: Standard BCG waveform.

5.1.5 FMF and MCF

As one kind of MCF, twin-core fiber (TCF), with two cores in a single optical fiber, is a widely-used specialty optical fiber for sensing [83,84]. For different sensing applications, many different structures, or even materials, are applied to standard TCF. For example, a TCF with dual cores in the symmetrical location of the optical fiber is proposed as one kind of Mach-Zehnder Interferometer (MZI) for temperature as well as strain sensing [85,86]. In contrast, an asymmetrical TCF with one core located in the center and the other positioned besides is fabricated for high-temperature measurements and RI monitoring in the form of both MZI and Michelson interferometers, respectively [87]. Other than the standard TCF, the suspended TCF using air-hole structure is also proposed [88]. Due to the birefringence of fiber cores, MZI is formed under polarized light, which can be used for curvature [89] and temperature sensing [90,91]. In addition, the twin-core photonic crystal fiber (TC-PCF) is designed and fabricated for strain, bending and pressure sensing [92–94]. Apart from various structures, materials can combine with TCF for sensing with excellent performance. For example, gold films are plated on the end of the frustum wedge TCF for surface plasmon resonance (SPR) sensing [95].

In this chapter, a novel sensing scheme is introduced by using FMFs and MCFs to realize non-invasive, convenient, simultaneous and accurate vital signs monitoring. Firstly, the TCF-based sensor follows SMF-TCF-SMF sandwich structure and the offset distance between SMF and TCF as well as the length of TCF are investigated, and the optimized options are obtained based on preliminary vital signs monitoring results. In the experiment, the TCF is packaged under a mattress to achieve non-invasive vital signs monitoring. As a result, thanks to its high sensitivity, both breath and heartbeat signal can be simultaneously obtained. In addition, reference breath and heartbeat signals are collected for comparison, which verifies the ability of TCF-based sensors for accurate HR and RR monitoring. For further applications, this TCF-based vital signs monitoring system is utilized to characterize the human post-exercise physical recovery process in terms of both amplitude and frequency of heartbeat and breath signals. Other than TCF, two kinds of FMFs, including TMF and four-mode fiber, and SCF, are also proposed for vital signs monitors design and fabrication. Good vital signs monitoring performance is achieved. Owing to the advantages of easily fabricated, non-invasive, high-sensitive and accurate signal detection, the FMF and MCF-based sensors can be potential and promising candidates for vital signs monitoring.

5.2 Twin-core fiber and sensor fabrication

Cross-section of the TCF used for vital signs monitoring is shown as Fig. 5.5 (a). It can be seen that one core locates in the center while the other one positions apart. The dimension of TCF is also shown in Fig. 5.5 (a). The diameter of cladding and core is 125 μm and 6 μm, respectively, and the distance between the two cores is 10 μm.

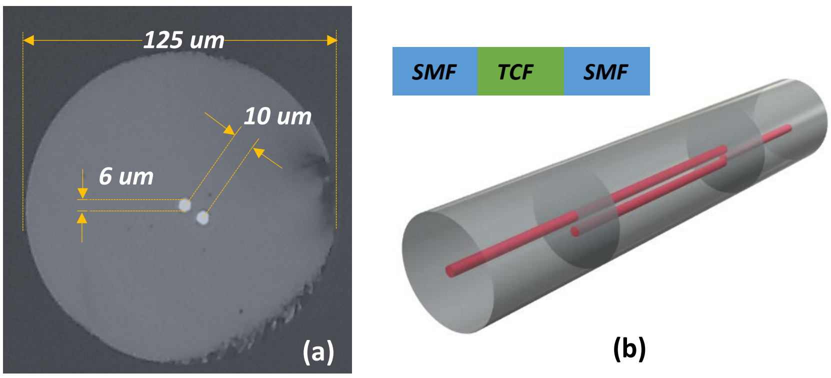

Fig. 5.5: Cross-section of TCF and its dimension (a) and sensor structure (b).

The sensor structure follows the conventional sandwich structure: SMF-TCF-SMF, which is shown in Fig. 5.5 (b). According to the coupled-mode theory, two cores in TCF are so close to each other that power exchange between cores will happen. The input SMF and TCF is firstly aligned and then spliced together following basic SM-SM splicing mode. Then, in TCF, power exchange, or mode coupling, takes place, where part of power in center core will couple to another core and couple back after a propagation distance of coupling length. The coupling length depends on the parameters of TCF, including core diameter and RI difference between the core and cladding. This kind of mode coupling can be fully characterized by the supermode theory. At the output end, another SMF is used to collect the light, where the offset distance between SMF and TCF will determine the power ratio between supermodes supported in TCF. The power exchange is schematically described in Fig. 5.6. This SMF-TCF-SMF has been demonstrated with an excellent output optical spectrum due to mode coupling, which is shown as the inset of Fig. 5.6.

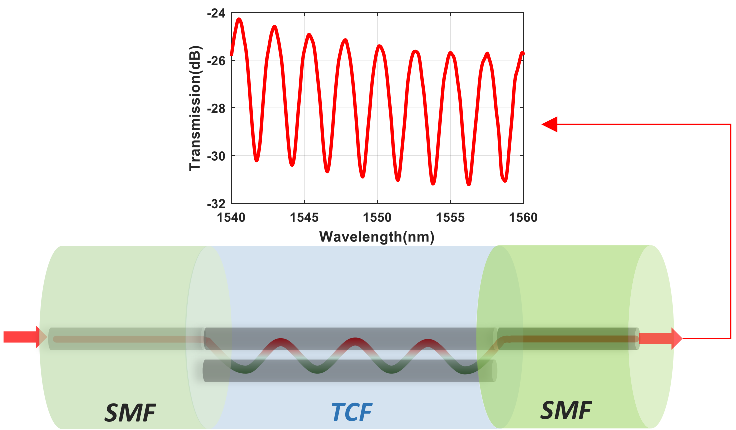

Fig. 5.6: Power exchange in SMF-TCF-SMF structure and corresponding output optical spectrum.

Aiming to obtain desirable performance for vital signs monitoring, the dimension of the TCF-based sensor needs optimization. As mentioned above, for this TCF-based sensor, offset distance between output SMF and TCF reveals the power ratio between supermodes. In other words, the ER of the output spectrum, which is one of the most important parameters for optical fiber sensors, depends on the offset distance. Thus, firstly, the output spectra under different offset distances between output SMF and TCF need to be analyzed experimentally. Thus, spectra are monitored and collected by BLS and OSA. Prior to offset, two cores in TCF and a single core in SMF require the location on the same plane so that the later offset distance adjustment can be performed accurately. This operation requires an end-view of TCF and SMF initially, which can be implemented by the splicer (Fujikura, LZM-100). Then, in the same splicer, TCF is fixed, and SMF is tuned along the line where two cores are connected, and the spectra are collected by the OSA. The results are shown in Fig. 5.7. It can be seen that, with the SMF aligned from the center core to the outer core, the ER in the spectrum increases from 2 dB to 5 dB until the fringe disappears due to over-offset. In order to achieve high sensitivity for this sensor, the offset distance between SMF and TCF is finalized with achieved ER around 5 dB.

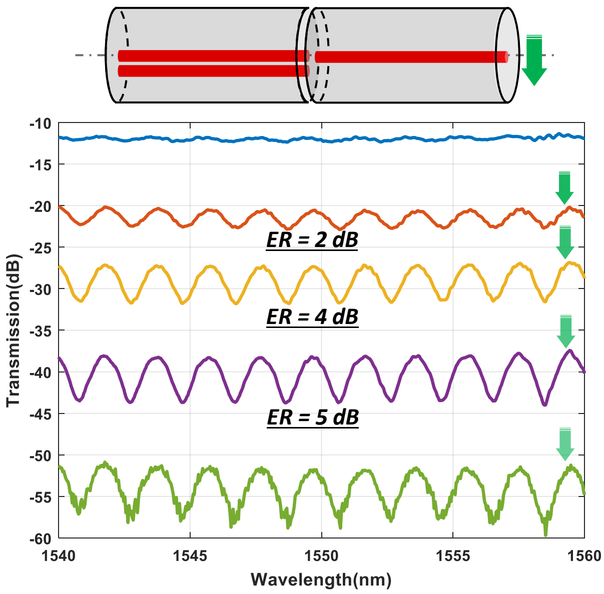

Fig. 5.7: Spectra under different offset distances between SMF and TCF.

Apart from offset distance, the length of the TCF also needs optimization. For optical fiber sensing, high sensitivity performance commonly means a large amount of spectrum shift induced by parameter variation. Meanwhile, the spectrum should not shift over the fringe period to avoid error. Thus, to adequately monitor vital signs signals, the fringe period in the spectrum needs to be optimized. Based on the coupled-mode theory, the fringe period depends on the length of TCF. Therefore, output spectra are recorded with different lengths of TCF, and results are collected and shown in Fig. 5.8. It can be seen that, the period or free spectrum range (FSR) increases proportionally from 1.8 nm to 4.8 nm when the length decreases from 1.0 m to 0.4 m. This result agrees well with the coupled-mode theory.

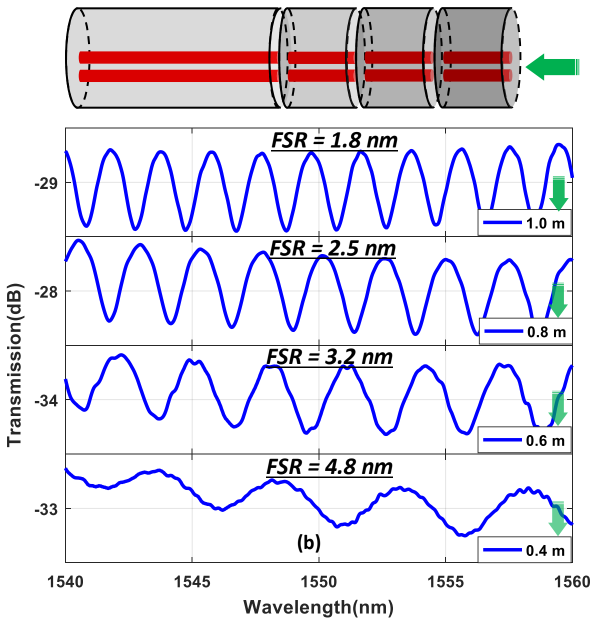

Fig. 5.8: Spectra collection under different lengths of TCF.

As mentioned above, for non-invasive vital signs monitoring using optical fiber sensors, the chest rise-and-fall due to respiration will change the pressure periodically on the sensor, and heartbeat detection is based on the detection of BCG signal. Therefore, it can be concluded that the amplitude of respiration is larger than that of the heartbeat. Both respiration and heartbeat, for the response on optical fiber sensors, will introduce the wavelength shift on the spectrum. Monitoring on the shift amount and frequency can help to achieve vital signs signals recovery eventually. Thus, wavelength shift induced by vital signs signals needs to be measured, especially the respiration with higher signal amplitudes, which will help to identify the length of TCF according to the results in Fig. 5.8. To identify the length of TCF, a preliminary experiment is conducted, and the setup is shown in Fig. 5.9 (a). The sensor is a Michelson interferometer using TCF with one end filmed by gold. The other end is spliced with SMF with specific offset distance mentioned above. In principle, light propagates through two cores, reflects at the end of TCF and then assemble back together in the input end. Two cores can be seen as the reference arm and sensing arm, and any change on the length of cores will induce the wavelength shift in the output spectrum. The spectrum is monitored by an interrogator (Micron optics, sm130) with scanning frequency up to 2 kHz, which is commonly used in FBG-based optical fiber sensing experiments. The sensor, especially the TCF, is attached on a mat under the mattress, which realizes non-invasive vital signs monitoring. The subject lays on the bed, and the interrogator records the wavelength shift results. The results are collected in Fig. 5.9 (b). It can be seen that the wavelength fluctuates from 1551.85 nm to 1552.15 nm within 1 min, which corresponds to the respiration signal. Thus, the amount of wavelength shift induced by respiration is ~0.3 nm. To measure vital signs signals with high accuracy and low error rate, the sensor should work on the quasi-linear and sensitive region in the spectrum, namely around the center point. Thus, according to the measurement result above, the operation region in the spectrum of the sensor is defined to 0.9 nm, which means that the length of TCF is 2 m based on the results in Fig. 5.8.

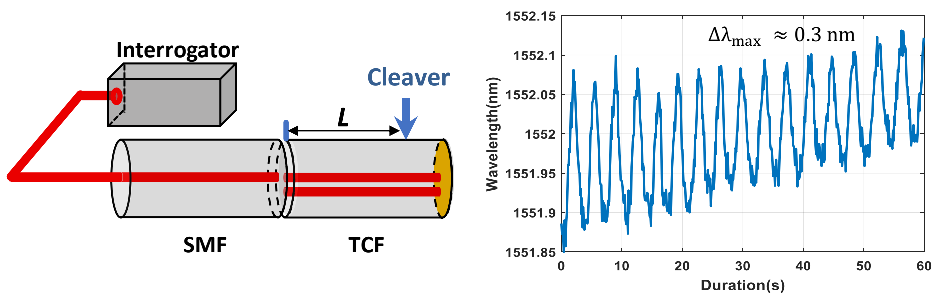

Fig. 5.9: Preliminary experimental setup for vital signs measurement (a) and obtained wavelength shift results (b).

5.3 Vital signs monitoring system

The TCF-based sensor for vital signs monitoring is fabricated with the dimension optimized above: specific offset distance with ER of ~5 dB and TCF length of 2 m. Then the sensor is sandwiched between two plastic substrates, which is placed under the mattress to realize non-invasive vital signs signals collection, as shown in Fig. 5.10 (a). a tunable laser source (TLS) is used as the light source, and a photodetector (PD) is used to convert the light intensity change induced by respiration and heartbeat to electrical signals. A data acquisition (DAQ) card is used for data collection with a sampling rate of 1 kHz, and a computer is for waveform display and further data processing. It is worth noted that, before data collection, the wavelength of TLS needs to be adjusted in order to make the sensor work at the sensitive and linear region. Thus, the wavelength is scanned firstly, as shown in Fig. 5.10 (b), and then fixed at *A* point. Actually, later center points can also be used as the operation wavelength.

To demonstrate the accuracy of the TCF-based sensor for vital signs monitoring, reference signals are necessary. According to the respiration reference signal, a camera is used to record the rise-and-fall of the chest due to respiration. The obtained video can be processed to recover the whole breath process timely. For the heartbeat reference signal, a commercially available device (Sparkfun, AD8232) is applied to acquire ECG signals, which is commonly used for HR calculation.

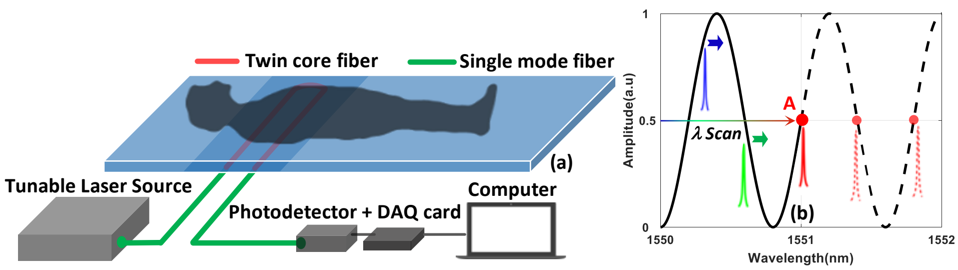

Fig. 5.10: Vital signs monitoring experiments, including the setup (a) and initial wavelength

scanning (b).

5.4 Vital signs monitoring results

To recover vital signs signals, many kinds of data processing methods were proposed in the past. Among them, the filtering technique is the most widely used one by taking advantage of the intrinsic difference in frequency and amplitude between respiration and heartbeat. Conventional filtering schemes are applied here, where two lowpass filters are utilized with different cut-off frequencies. The diagram of data processing is shown in Fig. 5.11. In order to get accurate HR and RR based on the raw data from TCF-based sensors, the details of respiration and heartbeat waveform, namely the peaks in BCG signals, need to be recovered. A highpass (HP) filter is firstly used for respiration signal recovery, and the cut-off frequency (F_c) is set to 0.5 Hz. For the heartbeat signal, it has been investigated that, to recover the J peak in BCG signal shown in Fig. 5.4, the interval of which is commonly used for HR calculation, the digital lowpass filter should work under F_c no lower than 25 Hz [96]. Thus, F_c of the second lowpass filter here for BCG recovery is set to 30 Hz. About the reference signal, the recorded video is edited to extract every time point of rise-and-fall of the chest while the ECG signal is recorded simultaneously following the standard procedure. The ECG signal collection is shown in Fig. 5.12.

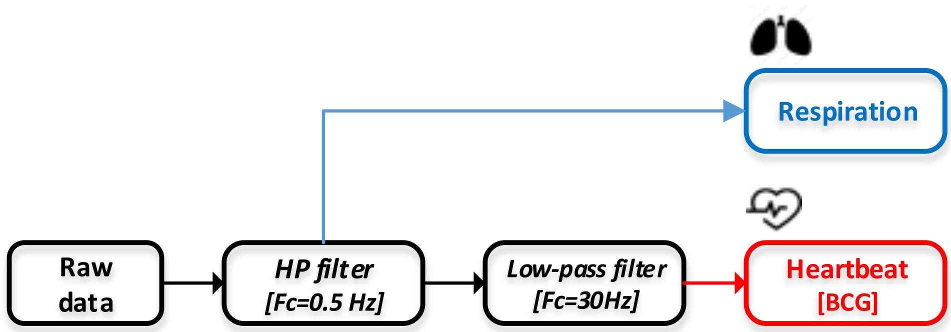

Fig. 5.11: The filtering technique to recover respiration and heartbeat signals.

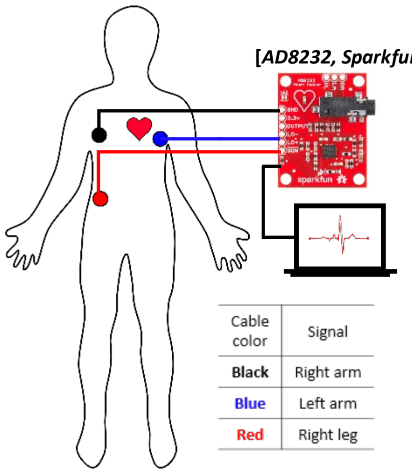

Fig. 5.12: Typical sensor placement for ECG monitoring device.

5.4.1 HR and RR monitoring

Figure 5.13 shows the recovered respiration and heartbeat waveform and the corresponding HR and RR. The blue line in Fig. 5.13 (a) represents the respiration signal from the TCF-based sensor, and the red stem line represents the moment where the chest rises to its highest level. It can be seen that every peak in the respiration waveform matches well with reference. The obtained HR is 10 beats per minute (bpm). According to the heartbeat signal, similarly, the blue line depicts the BCG waveform while the red line is the reference ECG signal. As introduced above, *J* peak in BCG signal and *R* peak in ECG signal are commonly used for HR calculation. From the results, we can see that the J-J interval is equal to the R-R interval. BCG signals within one minute are collected, and HR can be obtained from the number of peaks. The calculated HR is 65 bpm. Thus, both respiration and heartbeat waveform can be recovered from raw data by the filtering technique, and both HR and RR can be obtained from the number of peaks in respiration and BCG waveform within one minute, respectively.

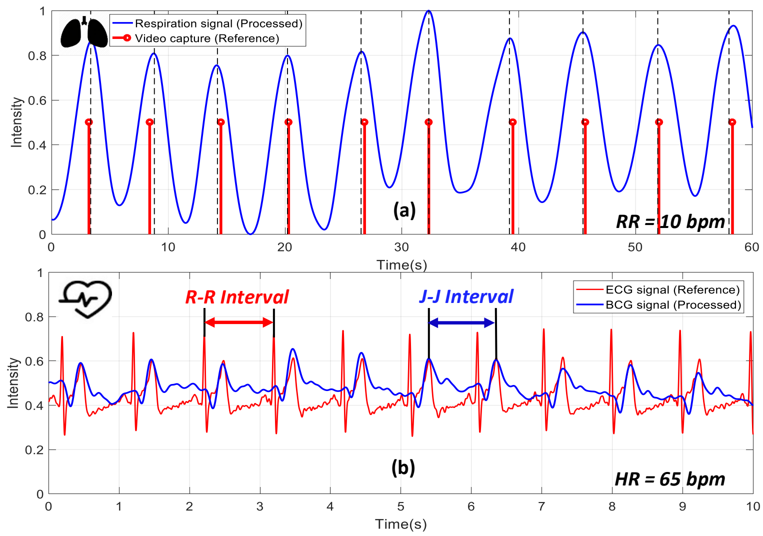

Fig. 5.13: Vital signs monitoring results, including the waveforms of respiration (a) and heartbeat signals (b) and calculated RR and HR.

5.4.2 Post-exercise physiological activities characterization

The sympathetic nervous system (SNS) and parasympathetic nervous system (PNS), as two subsystems of the human autonomic nervous system (ANS), play a key role in the central nervous working system. The dynamic interaction between SNS and PNS affects many kinds of human physiological activities, like heartbeat, respiration and perspiration [97]. Assessment of autonomic nervous function generally relies on these physiological activities analysis, which can help to detect various disorders or even prevent specific diseases. Heart rate variability (HRV) is widely used for physiological activities characterization thanks to its excellent advantages of non-invasive monitoring [98]. Generally, for HRV analysis related experiments, static exercise can be a desirable candidate since it is considered as a convenient and non-invasive protocol to modulate the timing interval of heart, or hemodynamics, where monitoring of the heartbeat data after exercise is necessary [99]. As mentioned above, the R-R interval in BCG signals can be used for HR calculation. Furthermore, it is also recommended as the HRV analysis standard officially.

In this section, since the TCF-based sensor has been demonstrated with excellent performance on vital signs monitoring based on the aforementioned results, the HRV analysis is performed on the heartbeat data collected after exercise. With the standard experiment procedure for HRV analysis, the subject is selected in good health condition and confirmed with no history of cardiopulmonary disease. Also, the subject is required to be free from alcohol and caffeine for 24 hours before the experiments. During the experiment, the subject is told to do a burpee exercise about one minute to increase the heartbeat rate and amplitude and lay right on the mattress, under which the sensor is placed. The experimental setup is the same as Fig. 5.10 (a) and the raw data are collected within 4 minutes during the rest of the subject. Following the same filtering techniques above, the obtained HRV analysis results are shown in Fig. 5.14. It can be seen that along the recovery process of the subject, the heartbeat ratio decreases continuously from 100 bpm to 69 bpm. Similarly, respiration results are collected in Fig. 5.15 and shows the same trend as the heartbeat. To summarize, HRV is performed successfully based on the TCF-based vital signs monitoring system thorough post-exercise physiological activities characterization.

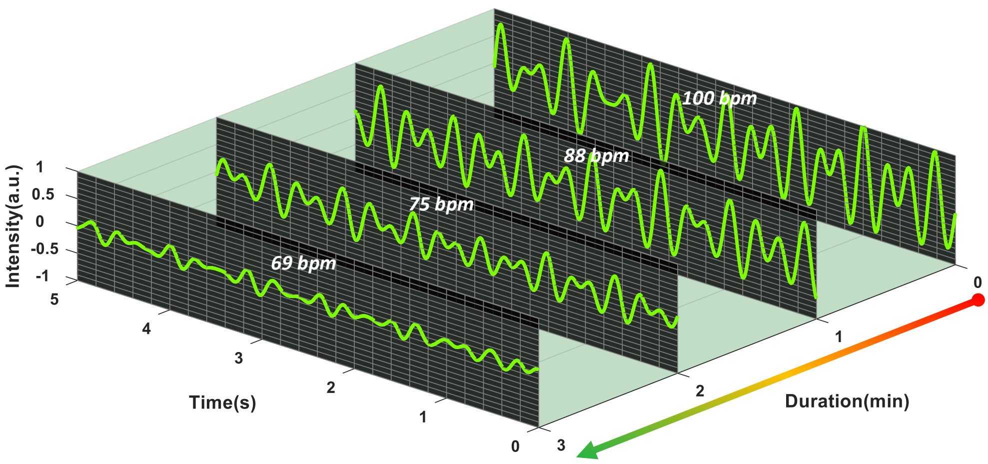

Fig. 5.14: Heart rate variability analysis results using TCF-based vital signs monitoring system.

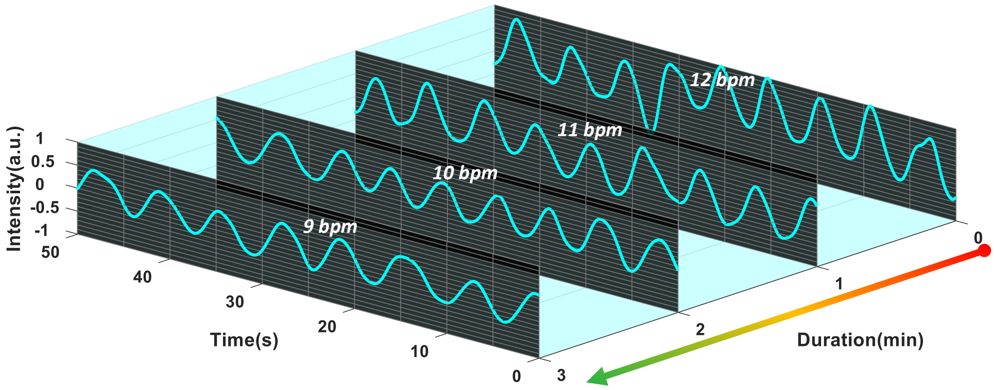

Fig. 5.15: Respiration rate variability analysis results using TCF-based vital signs monitoring system.

5.5 Principle and discussion

5.5.1 Supermode interference and curvature sensing

MCF is considered as a promising candidate for the SDM transmission and undoubtedly employed in future optical fiber communication network. With every core as an independent signal transmission channel, the capacity of the transmission network can be improved dramatically. However, the cores are not fully isolated, and the power exchange may happen between cores, especially when the cores are very close to each other. To characterize this kind of power exchange in a theoretical manner, supermode theory is introduced [100]. Supermodes are the eigenmodes in composite waveguides structures, the typical one of which is MCF. As is well known, in the multimode fiber, the eigenmodes are orthogonal to each other, and their superposition represents actual field distribution in optical fibers. In the same way, supermodes are a series of eigenmodes in MCF, and they can also generate the mode interference. Uniquely, supermodes are used for power exchange characterization in MCF.

In coupled mode theory, two kinds of orthogonal supermodes are supported in the TCF, symmetric and antisymmetric supermodes. They own different propagation constants and mode field distribution. The modal electrical field distribution of symmetric and antisymmetric supermodes can be obtained using COMSOL. Detailed parameters of TCF is shown in Table 5.1, and the calculated distribution of the electrical field of the two supermodes is shown in Fig. 5.16.

Table 5.1 Parameters of TCF for modal electrical field distribution of supermodes in COMSOL

Name	Value	Description
N_cladding	1.444	RI of cladding
N_core	1.450	RI of core
Dia_cladding	125 μm	Diameter of cladding
Dia_core	6 μm	Diameter of core
P	10 μm	Core pitch size in TCF
λ	1.55 μm	Wavelength

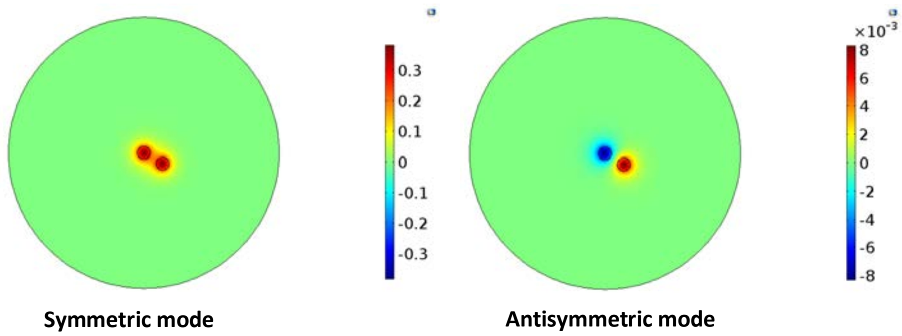

Fig. 5.16: Electrical field distribution of symmetric and antisymmetric modes.

For the TCF, the interference between the symmetric and antisymmetric mode also occurs due to their different propagation constants. The interference can be expressed as follows:

$$I = I_s + I_\alpha + 2\sqrt{I_s I_\alpha}\cos\left(\frac{2\pi}{\lambda}(n_s - n_\alpha)L\right) \tag{5.1}$$

where I is the output intensity, I_s and I_α are the individual intensity of symmetric and antisymmetric mode, L is the length of TCF, n_s and n_a are the RI of the two supermodes and λ is the optical wavelength. The simulation of supermodes interference is shown in Fig. 5.17. This kind of interference in TCF has been widely investigated for optical fiber sensing, such as temperature, strain and curvature. In this chapter, a curvature sensing experiment is performed to interpret the vital signs monitoring performance.

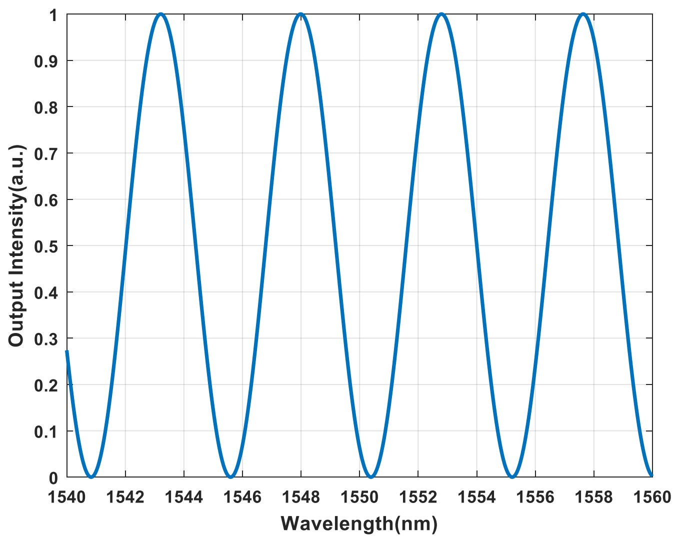

Fig. 5.17: Simulated optical spectrum based on the supermodes interference.

For curvature measurement using TCF, a theoretical model is established first, and experiments are conducted. The schematic diagram of bent TCF is shown in Fig. 5.18 (a). R represents the bending radius and X is the bending direction. In the TCF under bending, one core is in tension while the other one is in compression, which will induce RI change of two cores in the opposite direction. The RI of two cores follows the equation [101]:

$$n'(x) = n(x)(1 + \frac{1}{R}x) = n(x)(1 + Cx), \tag{5.2}$$

where $n(x)$ and $n'(x)$ are refractive index profile when TCF is straight and bent, respectively and C is the curvature. Based on the supermode theory in TCF, the effective RI of supermodes is very sensitive to RI change of two cores, especially in the opposite direction. Thus, under the bending of TCF, RI of two supermodes n_s and n_a will experience dramatic change. This will introduce a large wavelength shift in the spectrum.

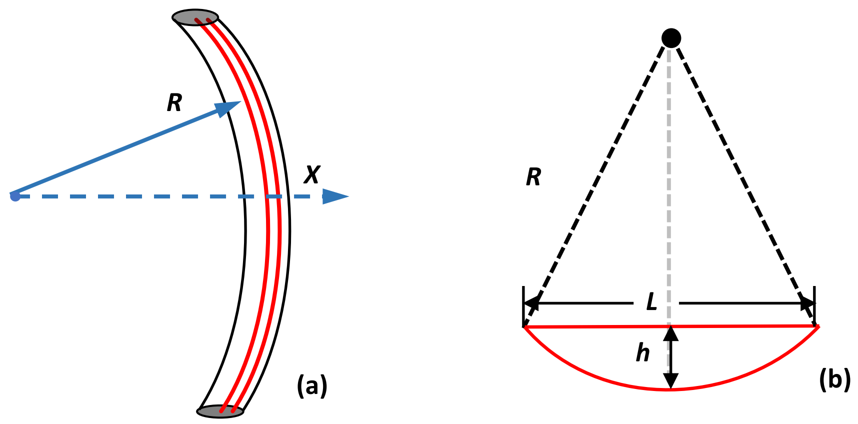

Fig. 5.18: Model of bending TCF (a) and curvature calculation in sector (b).

The sensing experimental setup is shown in Fig. 5.19, in which the BLS and OSA are used for spectrum monitoring. The sensor structure still follows Fig. 5.5 with an optimized dimension. The right holder is fixed, and the left translation holder moves along x-direction. It is worth noted that, before spectrum collection, orientation of two-core is labeled from microscopy and two holders are rotated to make sure that the bending direction and two cores are in one plane. During the experiment, the translation stage moves towards the fixed stage with a step of 1 mm and the height change in the central point between the straight and bending fiber is recorded. Then, corresponding spectra are collected. The curvature C can be calculated from the gap between stages and the height change h, as shown in Fig. 5.18 (b) and Eq. (5.3) as follows:

$$C = \frac{1}{R} = \frac{8h}{L^2 + 4h^2}. \tag{5.3}$$

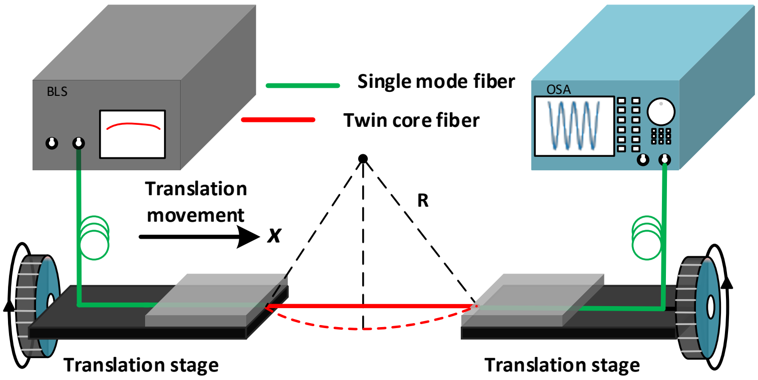

Fig. 5.19: Curvature sensing experimental setup.

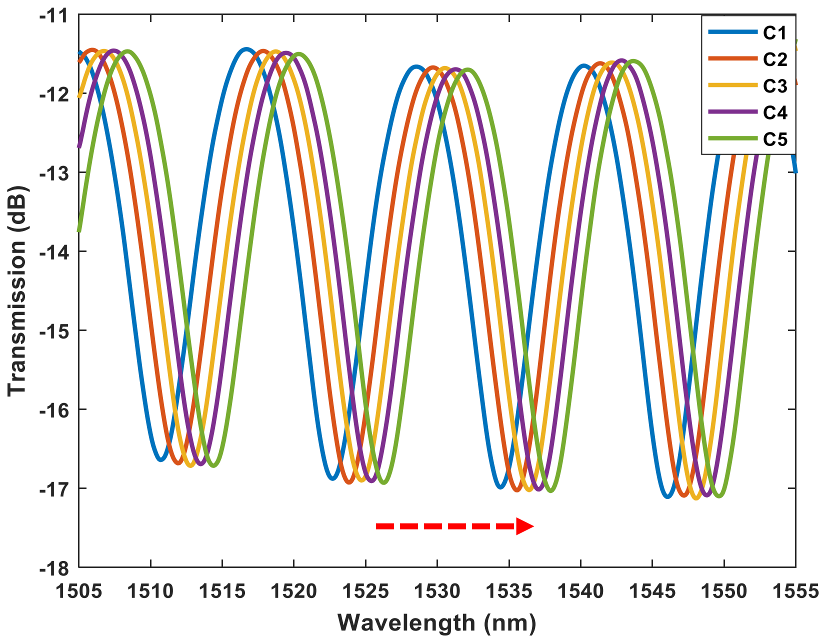

Fig. 5.20: Red-shift in spectrum with curvature increases from C1 to C5.

The curvature measurement results are illustrated in Fig. 5.20. With curvature increases from C1 to C5, the spectrum shows red-shift. One dip in the spectrum is monitored and the wavelength shifts under corresponding calculated curvatures are collected in Fig. 5.21. It can be seen that the amount of wavelength shift increases linearly with curvature. A curve fitting method is applied here, and obtained sensitivity can achieve 18 nm/m^{-1}, which is very high among current curvature sensors. This high sensitivity also explain the reason why this kind of TCF-based sensor can achieve excellent performance on vital signs monitoring.

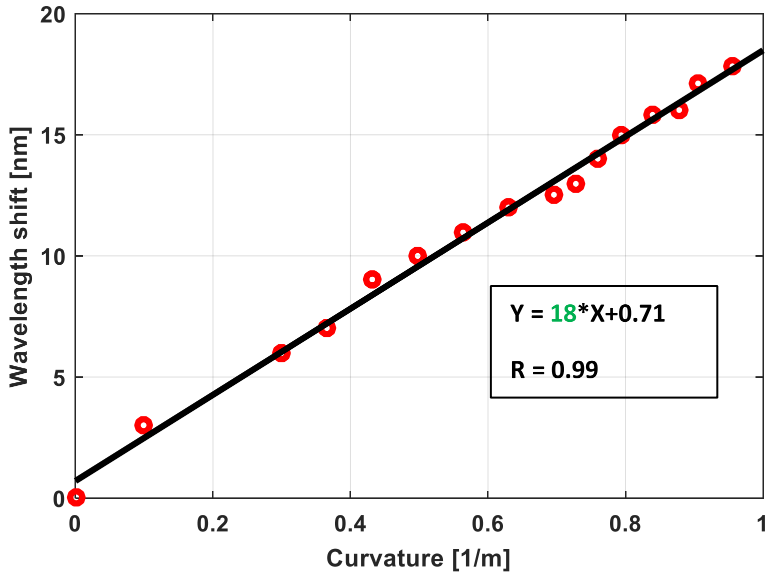

Fig. 5.21: Wavelength shift under every curvature and curve fitting to obtain sensitivity.

In addition, curvature sensing experiments are further performed under different axial orientation angles of TCF, as shown in Fig. 5.22. For example, with an orientation angle of 0°, meaning that the bending direction (red arrow) is along the two-core direction, the wavelength shift is recorded under curvature from 0 m^{-1} to 1 m^{-1}. The achieved sensitivity under this orientation angle is as high as 18 nm/m^{-1}. This may stand out among current curvature sensors. Then, the TCF is rotated axially to 120° on both ends, and the same experiment is conducted. In summary, with the fiber twist angle of 0°, 120°, 240°, 360°, the sensitivity can achieve 18 nm/m^{-1}, -7.5 nm/m^{-1}, -13 nm/m^{-1}, 18 nm/m^{-1}, respectively. This sensitivity difference is due to the different arm's length change in different orientations under identical curvature, which can be analyzed using the bending model. Therefore, it can be concluded that high curvature sensitivity of TCF interferometer contributes to its excellent performance on vital signs monitoring.

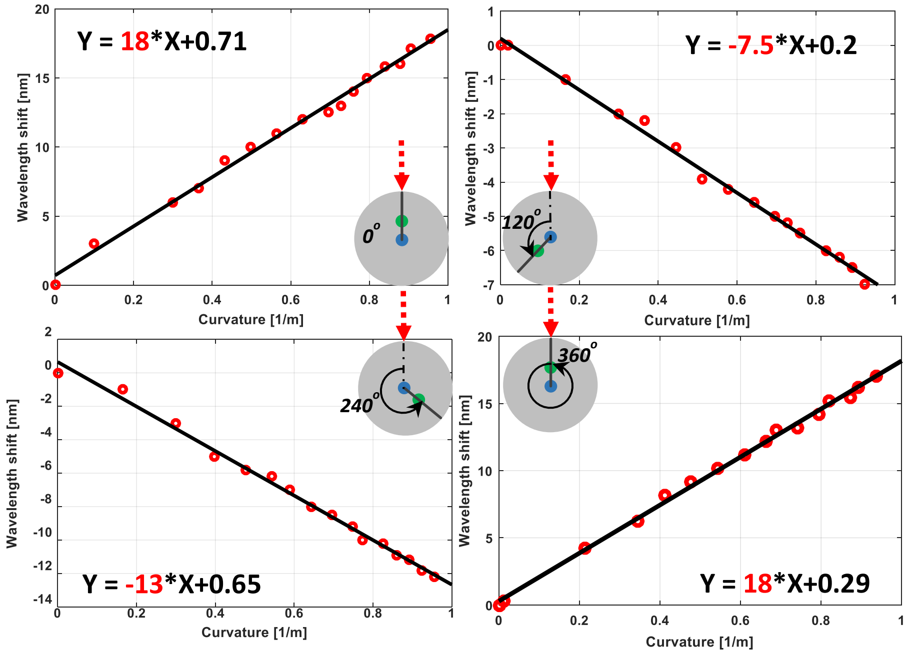

Fig. 5.22: Curvature sensing results under different axial orientation angles.

5.5.2 HR and RR monitoring

As demonstrated above, the TCF-based sensor shows high sensitivity performance on curvature measurement. A large spectral shift may happen under small changes on curvature, which means that if the experiment is conducted using a single wavelength laser, the output intensity will show large changes. For a monitored dip wavelength λ_m, based on Eq. (5.1), the output intensity I_m follows the equation:

$$I_m = \frac{\delta \cdot (n_s - n_\alpha) \cdot L}{2m+1}, \tag{5.4}$$

where δn is the RI difference between symmetric and antisymmetric modes, L is the length of TCF, m is an integer according to monitored wavelength λ_m and σ is a constant for simplification on later expressions. Therefore, based on the geometrical relationship in the sector shown in Fig. 5.18 (b), optical output intensity with respect to curvature can be expressed as follows:

$$\frac{dI_m}{dC} = \frac{dI_m}{dL} \cdot \frac{dL}{dC} = \frac{-\sigma \cdot \Delta n}{2m+1} \cdot \frac{L}{C}. \tag{5.5}$$

Thus, with the curvature C_0 and arc length L_0, dI_m/dC, which becomes actually a constant, is represented as α. Since the TCF-based sensor locates under the mattress, in our case, C_0 is way smaller than L_0, meaning that the sensitivity is very high for vital signs monitoring. When TCF is embedded under the mattress, vital signs signal, no matter breath (B) and heartbeat (H), will impose force change on the sensor, which will react in the way of curvature change. For its time-dependent response analysis, it is assumed that curvature (C) of TCF induced by vital signs relies proportionally on the force (F) generated from chest and heart movement. This can be expressed as follows:

$$\frac{dC_{(B,H)}}{dt} = \rho \cdot \frac{dF_{(B,H)}}{dt}, \tag{5.6}$$

where t is the time and ρ is a constant, C is the curvature and F is the force. Thus, combined with Eq. (5.5), the optical intensity change with vital signs signals can be expressed as:

$$\frac{dI_{m(B,H)}}{dt} = \frac{dI_m}{dC} \cdot \frac{dC}{dt} = \alpha\rho \cdot \frac{dF_{(B,H)}}{dt}, \tag{5.7}$$

where α and ρ are the constants introduced above. Thus, it can be seen that the output intensity is directly related to the force change induced by vital signs. According to current measurement on vital signs signals, BCG signal owns a amplitude of 4 Newton within 1s [81]. As is well known, the force change induced by chest fluctuation during inhale and exhale process will introduce larger force change on mattress than heartbeat, which helps to identify breath and heartbeat intuitively from obtained electrical signal.

5.6 FMF and SCF-based vital signs monitors

In this section, FMF and CCF were proposed for contactless vital signs monitoring. The sensor structure is based on conventional SMF-FMF/MCF-SMF in-line interferometers. For FMF, SMF is spliced on both ends with an optimized distance. Two kinds of FMF are investigated, including TMF and four-mode fiber, and they are packaged as a mattress under the bed to achieve contactless monitoring. Vital signs monitoring experiment is conducted, and results show that both two kinds of FMF-based sensors can achieve simultaneous HR and RR monitoring with acceptable accuracy. Other than FMF, the SCF is also utilized. The corresponding in-line interferometer is also designed and fabricated, and the same packaging and the following experiments show good vital signs monitoring results. In theory, the beam propagation method is utilized for mode excitation simulation in FMF. Based on FMF and SCF, both HR and RR can be monitored simultaneously in a contactless way with acceptable accuracy and stable performance, which makes the FMF and SCF promising candidates for vital signs monitoring in low-resource settings.

The FMF-based in-line interferometer is shown as Fig. 5.23. Traditional sandwich structure, SMF-FMF-SMF, is utilized and offset between SMF and FMF is used for modes excitation, especially the high-order modes. Two kinds of FMF are investigated, including TMF and four-mode fiber, which are both from OFS, Furukawa. FMF with the enlarged core can support more than one mode in a single optical fiber. The modes supported in FMF, namely LP_{01}, LP_{11}, LP_{02} and LP_{21}, are shown in Fig. 5.23.

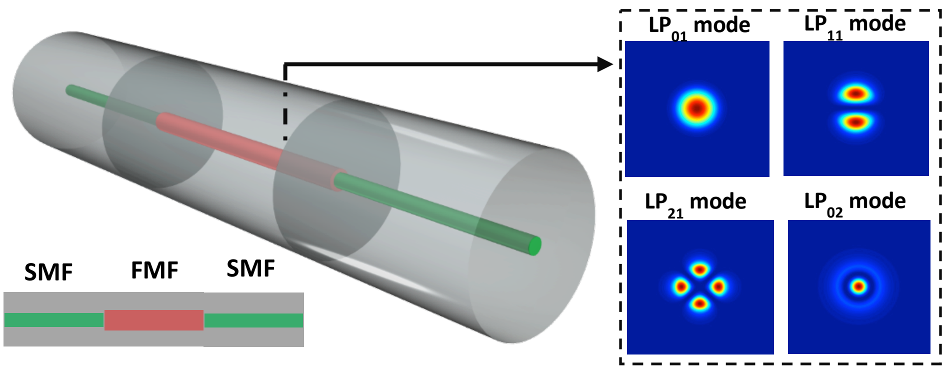

Fig. 5.23: Schematic diagram of FMF-based in-line interferometer and the modes supported in FMF.

For modes excitation, due to the mode field mismatch between LP_{01} mode in SMF and high-order modes in FMF in offset structure, modes can be excited with different power ratios under different offset distances. As a result, the spectral extinction ratio (ER) changes with SMF shifts away from the FMF in the center line. Since the sensitivity of this FMF-based interferometer is directly determined by the ER of the optical spectrum, the discussion on ER under different offset distances between SMF and FMF is performed experimentally. The experimental setup is shown in Fig. 5.24 (a) and results of TMF are shown in Fig. 5.24 (b). The broadband light source (BLS) ranging from 1550 nm to 1600 nm and optical spectrum analyzer (OSA, AQ6370D, Yokogawa) are utilized for optical spectrum monitoring. Two splicers (Fujikura FSM-100P, FSM-50s) are used for identical offset distance control between FMF and input/output SMF, as shown in the inset of Fig. 5.24 (a). SMF and FMF are aligned firstly, and the position of FMF on the holder is altered along the downward direction, as shown in Fig. 5.24 (a). In the meantime, the optical spectrum under every offset distance is collected. The results are shown in Fig. 5.24 (b). It can be seen that, with FMF away from SMF, the ER increases until the interference disappears due to high loss.

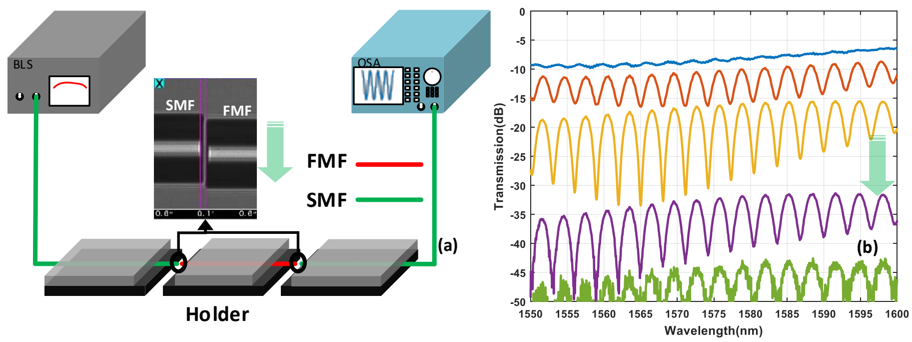

Fig. 5.24: Discussion on ER versus offset distance between SMF and FMF (a) and the results of TMF (b).

Based on the results in Fig. 5.24, ER as well as insertion loss variation with offset distance are obtained and summarized as Fig. 5.25 (a). The ER increases firstly and remains unchanged while insertion loss increases with off-core distance. Apart from the discussion on ER and insertion loss with offset distance, the spectral periods under different lengths of TMF are considered. The results are shown in Fig. 5.25 (b), in which the period increases proportionally with length decreases from 0.8 m to 0.4 m. This trend agrees with the traditional theory about optical fiber interferometers. Based on the results above, considering spectral ER, insertion loss and period, the offset distance is confirmed with achieved ER around 12 dB and the loss of -20 dB. The length of the TMF is around 1 m.

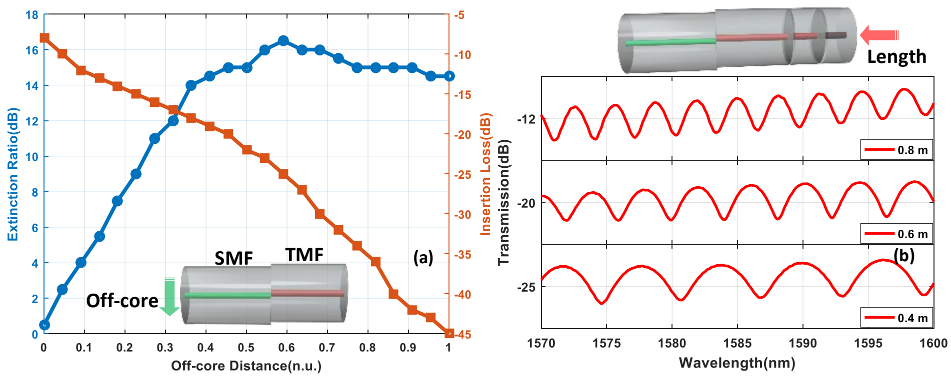

Fig. 5.25: Extinction ratio and insertion loss variation with off-core distance (a) and spectrum under different length of TMF (b).

Other than TMF, the four-mode fiber is also utilized for in-line interferometer fabrication. The structure still follows the TMF-based interferometer above, and experiments, as well as corresponding discussion, are also conducted in the same way. The optical spectrum under different offset distances between SMF and four-mode fiber and the summarized ER as well as insertion loss results are shown in Fig. 5.26. Different from the unique interference between LP_{01} mode and LP_{11} mode in TMF, more than one mode pair exists in four-mode fiber, which results in different trends of ER variation with offset distance. For example, the ER decreases initially to 2 dB with offset distance and then increases back to 20 dB with the following decline to 10 dB. The inset shows the spectrum under the ER of 2 dB, where the interference occurs with additional frequencies. Based on the results obtained, for the four-mode fiber interferometer design, the achieved ER is 14 dB with an insertion loss of -25 dB.

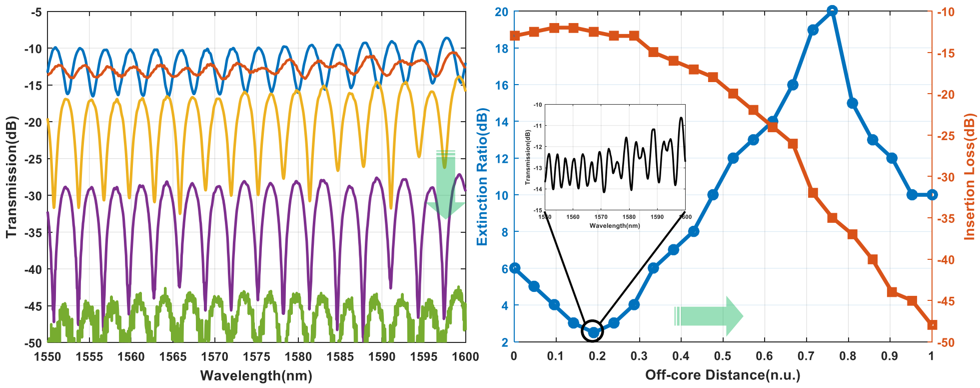

Fig. 5.26: Optical spectrum with offset distance and the summarized ER and insertion loss results.

MCF, with more than one core in a single optical fiber, can also be for in-line interferometer design. Different from the mode interference in FMF, every core in MCF can interfere with each other, which is called as core-mode interference. This core-mode interference exists in many kinds of MCF. For SCF, the interference between center core-mode and outer core-modes is employed. As shown in Fig. 5.27 (a), a multi-mode fiber (MMF) is sandwiched between SMF and SCF to enlarge the optical field in order to excite all the core-modes in SCF. Also, the same MMF is used in the output end to collect the light into SMF. Then, the output spectrum of the SCF interferometer is shown in Fig. 5.27 (b). In the interference spectrum of the SCF interferometer, the ER is 3 dB.

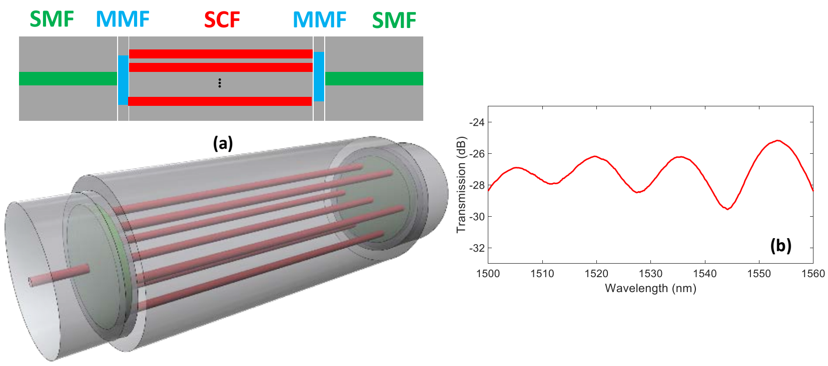

Fig. 5.27: Schematic diagram of SCF in-line interferometer (a) and the obtained optical spectrum (b).

Following the filtering process introduced in the TCF-based section, for FMF interferometers, the vital signs signals are recovered and corresponding HR as well as RR are obtained. The results are shown in Fig. 5.28 and Fig. 5.29. Fig. 5.28 shows the recovered respiration and heartbeat signals using the TMF interferometer while Fig. 5.29 shows the results regarding four-mode fiber.

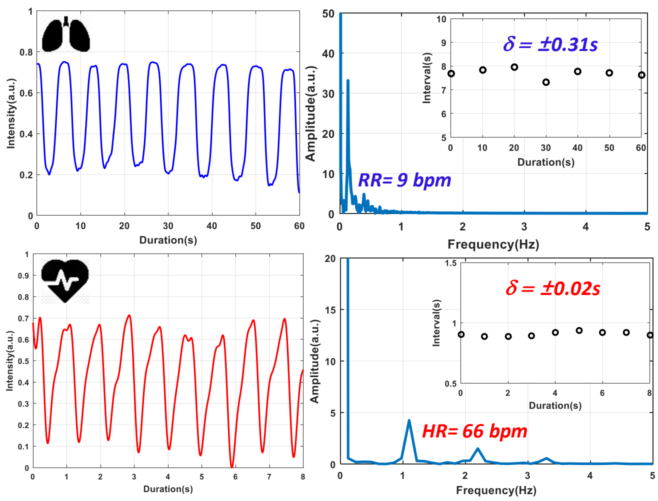

Fig. 5.28: Vital signs monitoring results using TMF.

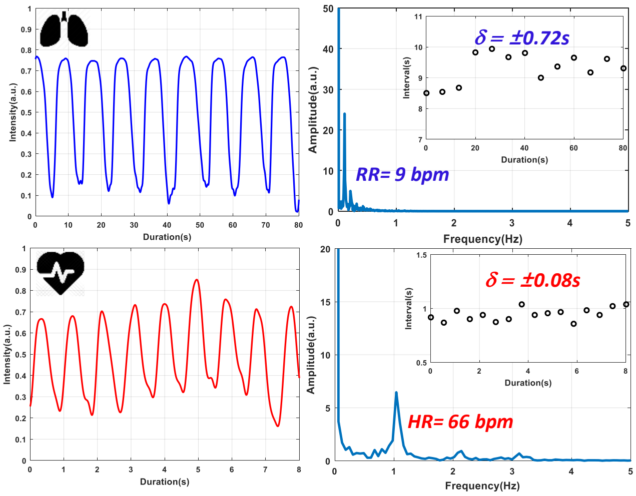

Fig. 5.29: Vital signs monitoring results using four-mode fiber.

To obtain HR and RR results, based on the recovered respiration and heartbeat signals, the Fourier transform is applied. Then, according to the obtained peak frequency, HR and RR can be calculated in the unit of bpm. Furthermore, the intervals between peaks in recovered respiration and heartbeat signals are collected and summarized to get the error δ. For example, for breath signal of TMF within one minute, which locates at the upper region in Fig. 5.28, the RR calculated is 9 bpm, and the breath interval error δ is 0.31 s. Similarly, for breath signal of four-mode fiber, the obtained RR is also 9 bpm and interval error δ is 0.72 s. The heartbeat results still follow the same analysis method, and the results show that HR obtained from TMF and four-mode fiber are both 66 bpm, and their heartbeat interval errors are 0.02 s and 0.08 s, respectively. It can be seen that, both HR and RR results locates in the normal range and the interval errors are small enough to guarantee the accuracy for HR and BR estimation, which demonstrates the feasibility of FMF and MCF in-line interferometers for simultaneous as well as accurate vital signs monitoring in a contactless manner.

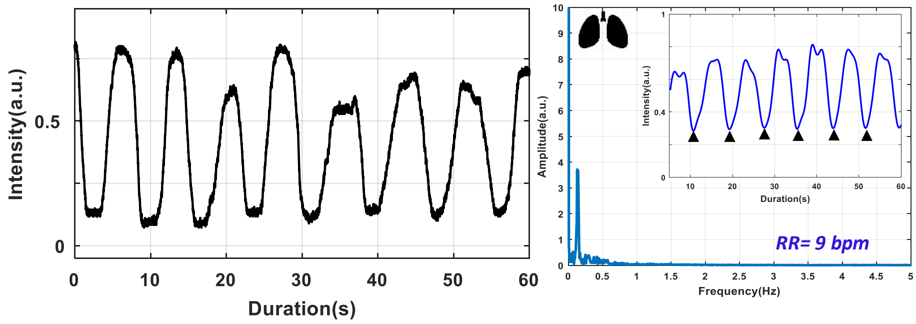

Fig. 5.30: Vital signs monitoring results using SCF interferometer.

For the SCF interferometer, the lowpass-filtered waveform can be used for RR calculation, as shown in Fig. 5.30, while the filtered heartbeat results fail to be utilized to calculate HR. This may due to the weak interference between center core-mode and outer core-modes under large core pitch sizes.

In summary, the performance of FMF and MCF on vital signs monitoring is compared in terms of complexity, extinction ratio, insertion loss, sensitivity and vital signs signals. The results are shown in Table 5.2.

Table 5.2 Performance comparison of FMF and MCF on vital signs monitoring.

Optical fiber	Complexity	Extinction ratio	Insertion loss	Sensitivity	Vital signs signals
Two mode fiber	Low	12 dB	-20 dB	Medium	HR and RR
Four-mode fiber	Low	14 dB	-25 dB	Medium	HR and RR
Twin core fiber	Medium	5 dB	-30 dB	High	HR and RR
Seven core fiber	High	3 dB	-28 dB	Low	RR

As introduced above, the offset structure between SMF and the FMF is introduced to excite high-order modes in the input end of FMF. This is due to the mode electrical field mismatch between the fundamental mode in SMF and high-order modes in FMF. The mode excitation ratio calculation follows conventional overlap integral [102], which can be expressed as follows:

$$F_{i,j}=\frac{\int_{-\infty}^{+\infty}\int_{-\infty}^{+\infty}I_i(x,y)I_j(x,y)dxdy}{\int_{-\infty}^{+\infty}\int_{-\infty}^{+\infty}I_i(x,y)dxdy\int_{-\infty}^{+\infty}\int_{-\infty}^{+\infty}I_j(x,y)dxdy}, \tag{5.8}$$

where I_i can be the intensity distribution of input fiber mode and I_j can be the excited mode. To discuss the offset impact on mode excitation theoretically, the beam propagation method is utilized. The models of FMF are established, including TMF and four-mode fiber, then offset distance between cores in SMF and FMF is tuned and the excitation result of every mode can be obtained from the monitors set on the output end of FMFs. The results are shown in Fig. 5.31. It can be seen that, for TMF as shown in Fig. 5.31 (a), the LP_{01} mode intensity decreases with offset distance while LP_{11} mode intensity increases to the highest level under offset distance around 5.5 μm, and decreases until the interference disappears. The ER is dependent on the intensity ratio between two modes, and it can reach the highest level when the power level of two modes are identical. Thus, from the simulation results, the ER should increase firstly and then remain unchanged, which agrees well with the experiment results shown in Fig. 5.25. For four-mode fiber, the results are shown in Fig. 5.31 (b).

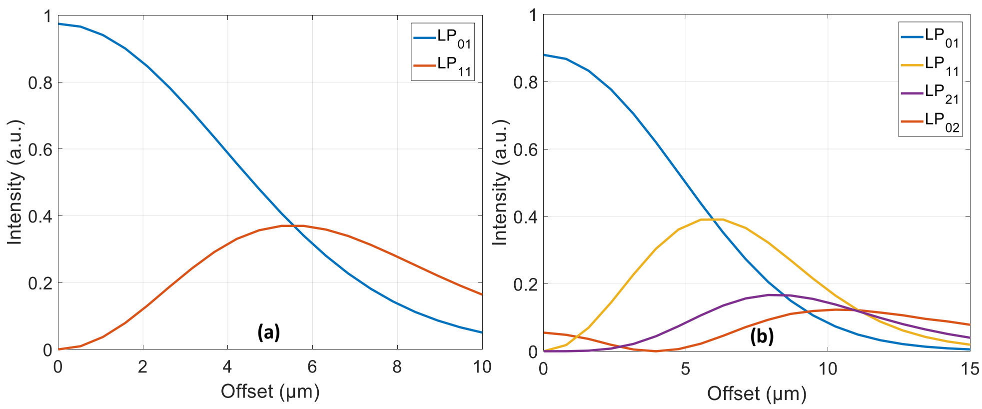

Fig. 5.31: Simulation on mode excitation under different offset distance between SMF and TMF (a)/four-mode fiber (b).

In summary, FMF and SCF based in-line interferometers are proposed for contactless vital signs monitoring, including HR and RR. The FMF interferometer is designed with FMF sandwiched between the SMF, and the offset between SMF and FMF is applied for mode excitation in order to form mode interference. Two kinds of FMF are investigated, including TMF and four-mode fiber, and the optical spectra under different offset distances are collected. The dimension of the interferometer is optimized, considering the ER and insertion loss with offset distance. For SCF interferometers, SCF is utilized and desirable optical spectrum is obtained for vital signs monitoring. FMF and SCF interferometers are packaged under the mattress to perform vital signs monitoring experiments. The filtering technique is applied to the collected raw data and reasonable cut-off frequencies are selected. For FMF, both respiration and heartbeat signal are recovered successfully, and HR and RR are obtained with acceptable accuracy. On the other hand, the SCF-based can detect RR. Theoretically, mode excitation is simulated in FMF, which agrees well with the experiment results. In conclusion, FMF and MCF for contactless vital signs monitoring are demonstrated successfully, which shows their potentials on future healthcare applications.

5.7 Summary

In this chapter, the healthcare applications of FMF and MCF sensors are explored, and non-invasive vital signs monitoring is achieved. The FMF and MCF sensor structure follow traditional in-line interferometers with SMF spliced on both ends. For TCF, the offset distance between SMF and TCF and length of TCF are firstly optimized experimentally. Then the filtering technique is applied to the data collected and the obtained results show excellent performance, including HR and RR monitoring. Furthermore, post-exercise physiological activities are successfully characterized using HRV analysis based on the TCF sensor. Theoretically, supermode interference in TCF is discussed, and curvature sensing experiments are conducted to analysis the excellent vital signs monitoring performance. Other than TCF, FMF and SCF are also employed to achieve non-invasive vital signs monitoring. The TMF and four-mode fiber-based in-line interferometers can both simultaneously detect HR and RR while the SCF-based can realize RR monitoring. In conclusion, FMF and MCF sensors can be promising candidates in future healthcare applications.

6 Mach-Zehnder Interferometer for remote activities monitoring and myocardial contractility assessment

In last chapter, in-line interferometers based on FMF and MCF are utilized for vital signs monitoring. This first attempt shows the potential of optical fiber sensors on healthcare related sensing applications. In this chapter, healthcare applications of optical fiber sensors are further explored. Firstly, a traditional optical fiber Mach-Zehnder Interferometer (MZI) for remote activities monitoring for the Alzheimer's disease and related dementia caregiving is introduced, including the optical fiber sensor layout, circuit fabrication and Wi-Fi network deployment. Other than that, the application of this optical fiber MZI on myocardial contractility assessment is described.

6.1 Introduction

6.1.1 Alzheimer’s disease and related dementia caregiving

Among various types of dementia, Alzheimer’s disease is the most common form, and the number of elderly living with Alzheimer’s disease and related dementia (ADRD) has been rising worldwide [103]. Early signs and symptoms of ADRD include memory loss, difficulty completing familiar tasks, trouble understanding visual images and spatial relationships and so on [104]. Among them, sleep/wake cycle disturbance (SWD) is a prominent and often highly disruptive behavioral symptom associated with ADRD, and epidemiological studies reported that up to 45% of patients living with ADRD have SWD [105]. The main sleep disorders include micro-architectural sleep alterations, nocturnal sleep fragmentation and decrease in nocturnal sleep duration [106]. Patients suffering from SWD may roll on the bed, sit up occasionally or even leave the bed during the night. This will cause unpredictable outcomes at home or in the assisted living facility. Therefore, caregiving for ADRD patients becomes necessary as well as urgent, especially during the nighttime. This creates a growing demand of caregivers [107]. Furthermore, the number of ADRD patients in developed countries is expected to increase significantly due to their aging population. This exacerbates much pressure on caregivers as current sociodemographic trends indicate that the number of caregivers for ADRD patients is expected to decline in the upcoming decades [108]. On the other hand, long-term nighttime care service causes depression, become burdensome, worsen immune system function and increase mortality in caregivers. These will obviously diminish care quality. Consequently, there is an imminent need to alleviate the “care-gap” pressure, and various technologies are proposed aiming to supplement ADRD caregiving [109,110].

6.1.2 Remote activities monitoring system for ADRD caregiving

Remote activity monitoring (RAM) systems to help caregivers to improve person-centered outcome for ADRD patients are drawing attention in both research and industrial communities. Clinical trials are being conducted to evaluate the impact of the different kinds of RAM systems [111–113]. Large-scale randomized controlled trials (RCTs) are conducted to test the effectiveness of a night monitoring system based on bed sensors and home exit sensors [114]. The evaluation results are promising, for example, a 12-month period RCT comparing the RAM group (26 dyads) with the control group (27 dyads) found that RAM users are 85% less likely to suffer from the nighttime harm.

Nighttime monitoring is a crucial aspect of RAM system for ADRD patients and bed sensors play a key role among the sensor network in recognition of patients' activities, such as on bed/sit on bed/off bed [115]. The sensors alert any abnormal activity of the patients to the caregivers in real-time. Current bed sensors include video, wearable apparatus and electrical pressure sensors. ADRD patient monitoring using video for direct behavioral observation requires all-night constant monitoring from caregivers, and it also introduces the ethical issue of privacy [116]. The traditional wearable apparatus, wrist actigraphy, is used as a reliable procedure to record the sleep/awake alteration in ADRD patients but the wearable monitoring discomfort the users, especially for patients at the advanced stage of illness [117]. Non-wearable electrical sensors, such as capacitive or piezoelectric sensor array, can recognize the different sleep states, but also can monitor the vital signs of patients [118]. However, the most critical problem of these sensors is that the effective sensing area of each sensor is limited to several cm^2 and that an insufficient number of sensors are used to cover a single bed. As a result, the recognition error rate is too high to be reliable for practical long-term care services.

6.1.3 Optical fiber sensors in RAM system

Optical fiber sensors, owing to their many advantages such as the ability to measure a wide range of parameters, no electrical power needed to power the sensors, and immunity to electromagnetic interference, have drawn increasing attention in many industries. Optical fibers configured as Mach-Zehnder Interferometers (MZI) are very sensitive to perturbation of the surrounding environment, thus are widely used for various parameters measurement [119,120].

In this chapter, we proposed a nighttime monitoring system based on an optical fiber MZI for ADRD caregiving. The RAM system is composed of an MZI based bed sensing unit, the corresponding integrated circuit for signal processing as well as wireless result output and network infrastructure for deployment. The MZI is easily fabricated and embedded under the mattress, which makes the activity monitoring noninvasive. Combined with an electrical sensor, wherever patients sit or sleep on the bed, four activities, on/sit/off the bed/body movement, can be recognized with a low error rate in long-term monitoring. Other than the activity recognition, vital signs, including respiration and heartbeat rate can also be obtained, which may help to identify the illness stage of ADRD patients. All the components, including the laser source, detector, the processor and Wi-Fi chip, are packaged together and attached aside the bed. The power consumption of every component is analyzed, and the activity decision and output algorithm are optimized for power saving under normal working conditions. For the upcoming deployment in a local ADRD caregiving house, stability test is also conducted, the result of which shows the stable performance of our RAM system. To the best of our knowledge, this is the first time that optical fiber MZI is adopted in the RAM system. The advantages of non-invasive monitoring, easy fabrication and production, stable and accurate activity recognition, low-cost and low power consumption make this optical fiber MZI based RAM system promising for ADRD caregiving. Other than activities monitoring, with detailed BCG signal detection, the MZI-based cushion can also realize myocardial contractility assessment combined with ECG signal. The pre-ejection period is characterized in order to demonstrate the feasibility of MZI on heart function measurement.

6.2 RAM system

The schematic diagram of the RAM system is shown as Fig. 6.1. In the caregiving room, the bed sensor is placed under the mattress, which enables non-invasive monitoring of patients. The Wi-Fi router is used to receive the messages from multiple bed sensors and then send the activity messages of every patient timely to the central monitoring console in the monitor room. Therefore, caregivers in the monitor room will be informed of the activity of every patient, the corresponding icons of which are also designed. The bed sensor is composed of an optical fiber MZI and an electrical pressure sensor. The MZI is easily fabricated by splicing two 1x2 couplers working on 1550 nm to form the reference arm and sensing arm, the length of which are both 2 m. The MZI is rectangularly attached on a mat, which is placed under the mattress. In addition to the MZI part, the laser source and photodetector are integrated together with the laser driver, regulator and processor. The laser driver is used to tune and stabilize the current input of the laser source while the regulator is used as the smart switch for laser and detector. Combined with an electrical pressure sensor, the regulator can realize automatic on/off of system thus decreases the power consumption with our designed algorithm. The power consumption of these components and the algorithm will be discussed later in this chapter. The processor (ESP32, Espressif) used here is a widely-used IoT device, which is integrated with a complete standalone microprogrammed control unit (MCU) and a hybrid Wi-Fi & Bluetooth chip. Our proposed activity recognition algorithm can run successfully on the MCU, and the Wi-Fi module takes in charge of the communication within this wireless network. Both the PC and smartphone can receive notifications through serially connected routers. Due to the advantages of high efficiency in terms of both latency and bandwidth than TCP, as a widely-used connectionless protocol, user datagram protocol (UDP) is adopted within the Wi-Fi network. The ESP32, Wi-Fi router and center monitoring console can communicate with stable performance.

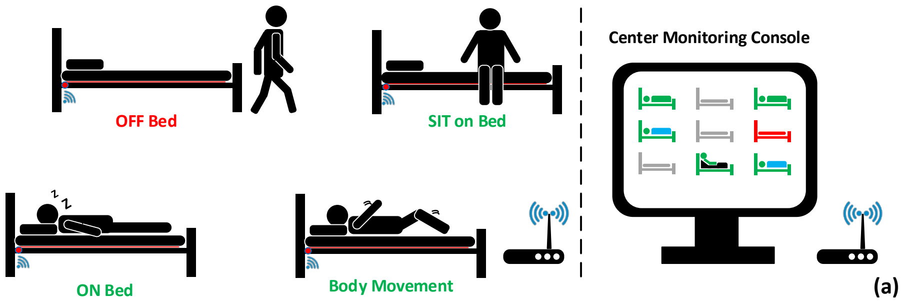

Fig. 6.1: Schematic diagram of RAM system.

The laser source used here is a distributed feedback (DFB) laser with a single wavelength around 1550 nm, which is also the standard laser source for the MZI system. The performance of the DFB laser is shown in Fig. 6.2. It can be seen that the monochromaticity performance is good. The center wavelength is about 1535.2 nm and the linewidth is around 0.1 nm. The inset shows the full optical spectrum in the wavelength range from 1550 nm to 1580 nm.

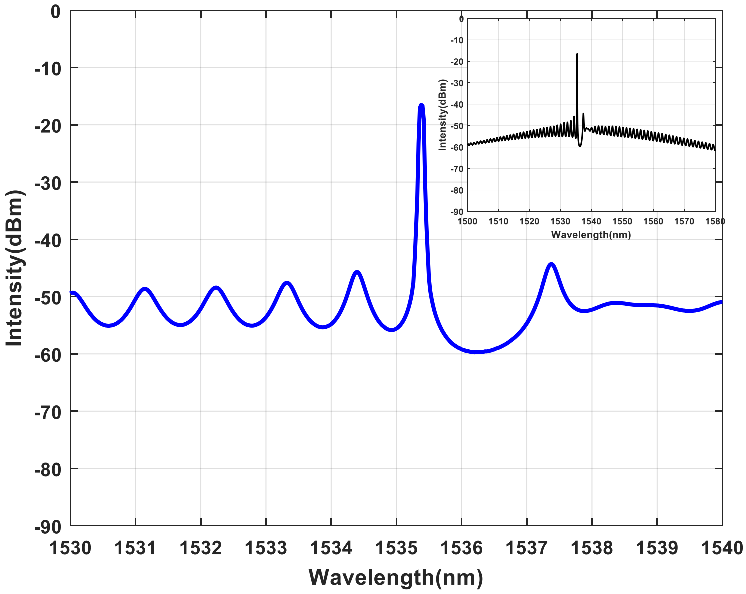

Fig. 6.2: Optical spectrum of DFB laser.

To make sure the optical fiber sensing system in a stable state, a test on the laser source is necessary. For DFB laser, we change the driver current and record the output power and center wavelength, the results of which are shown in Fig. 6.3. It can be seen that, with current from 9.7 mA to 19.7 mA, the power increases from -40.1 dBm to -5.73 dBm, while center wavelength changes from 1552.828 nm to 1552.96 nm, which demonstrates the desirable stability of the DFB laser.

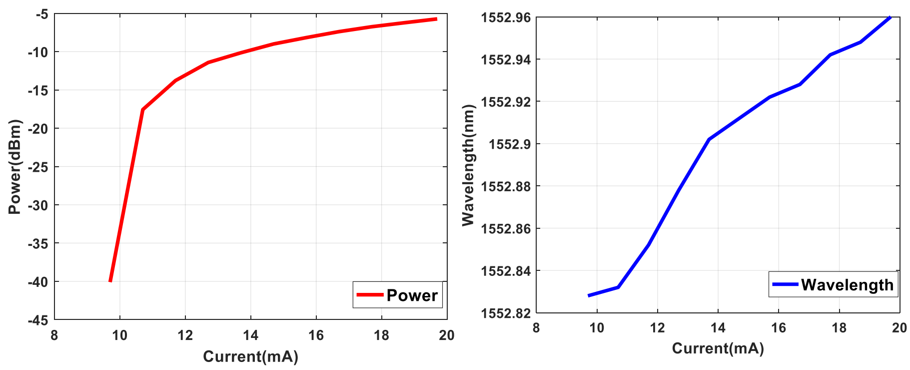

Fig. 6.3: Stability test of DFB laser.

Also, we try the Fabry-Perot (FP) laser as laser source with multiwavelength, the optical spectrum of FP laser is shown in Fig. 6.4.

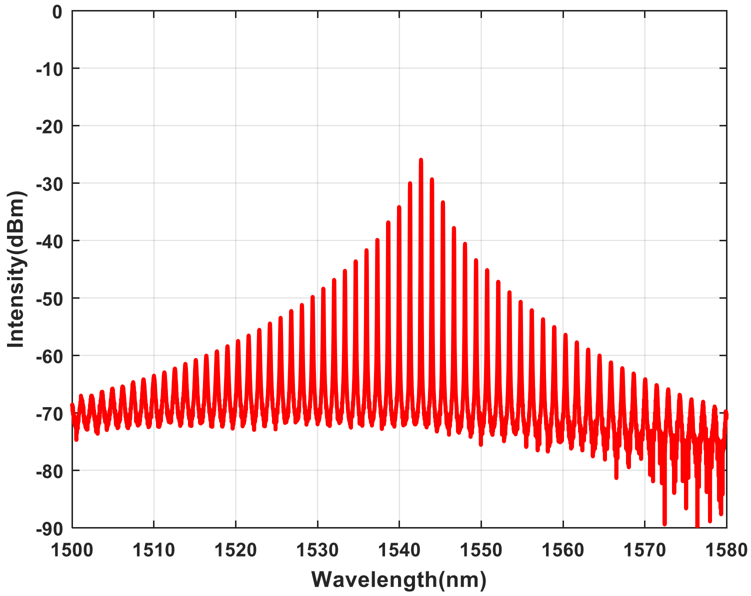

Fig. 6.4: Optical spectrum of FP laser.

The optical fiber sensing system used in the RAM system is a conventional MZI, the diagram of which is shown in Fig. 6.5. Two arms are separated for reference arm and sensing arm. In principle, the FSR of the spectrum of MZI decreases with the length difference of two arms. MZI will own high sensitivity with a small free spectrum range (FSR). Thus, to make the RAM work under high sensitivity, we increase the length difference of two arms as much as possible until the interference loses. According to the optical spectrum of DFB laser, the center wavelength is 1552 nm while the linewidth is 0.2 nm, which concludes the coherence length to be 15 mm. Thus, the MZI is fabricated with length difference around 15 mm.

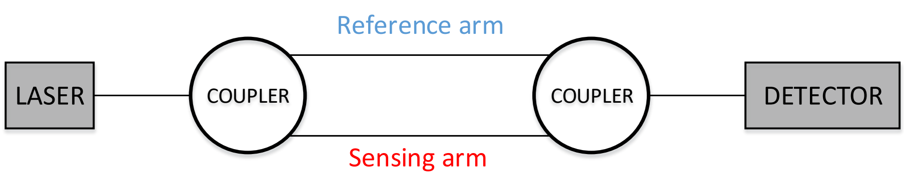

Fig. 6.5: Schematic diagram of MZI.

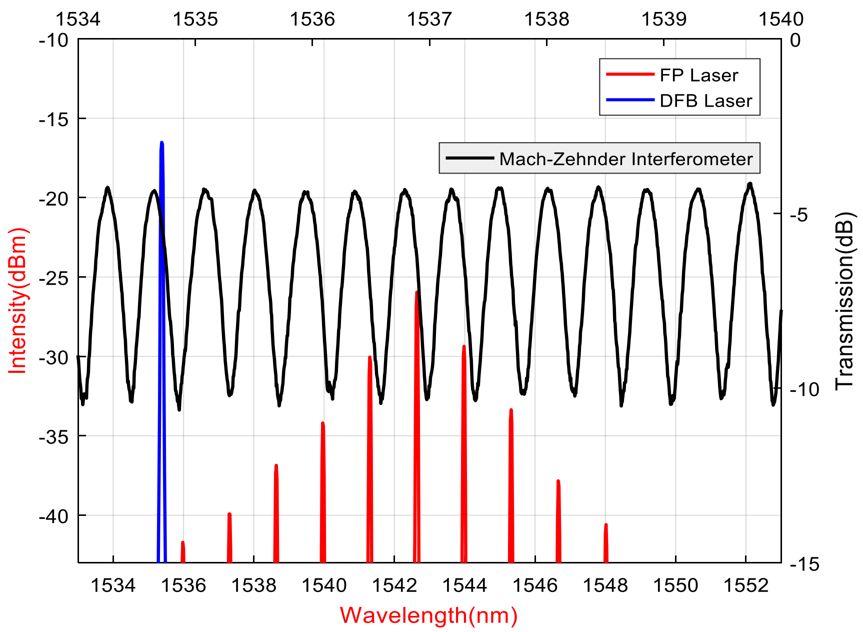

Fig. 6.6: Optical spectrum of MZI and laser options.

6.3 Algorithm for activities recognition

To recognize four activities of the patients: sit/movement/on/off bed, we first collect the corresponding waveforms and then compare them as shown in Fig. 6.7(a). A jitter level analysis method is adopted here to distinguish four activities, the principle of which is shown in Fig. 6.7(b). Jitter level (J_1) on one point, such as point 1, is calculated from the Y-axis length difference between 1_L and 1_R, in which the points L and R are the left and right points of point 1 respectively as shown in the lower equation in Fig. 6.7 (b). Data is sectioned with equal length, and the total jitter level within every region (J_T) is obtained from the sum of the jitter level of every point, which is shown in the upper equation in Fig. 6.7 (b). To identify the state of ON and SIT, an electrical pressure sensor is used in the system. Both optical fiber signals and electrical signals are used to distinguish these four activities. Based on the data collected from four activities within 5 minutes, the calculation results are shown in Fig. 6.8.

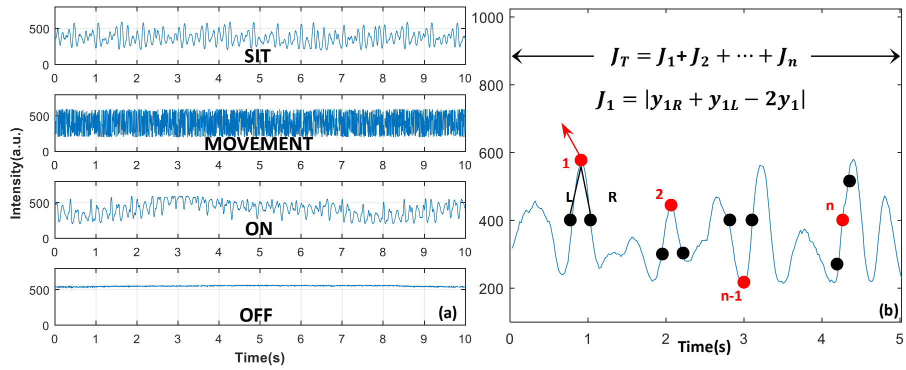

Fig. 6.7: Waveform of SIT/MOVEMENT/ON/OFF and jitter level calculation principle.

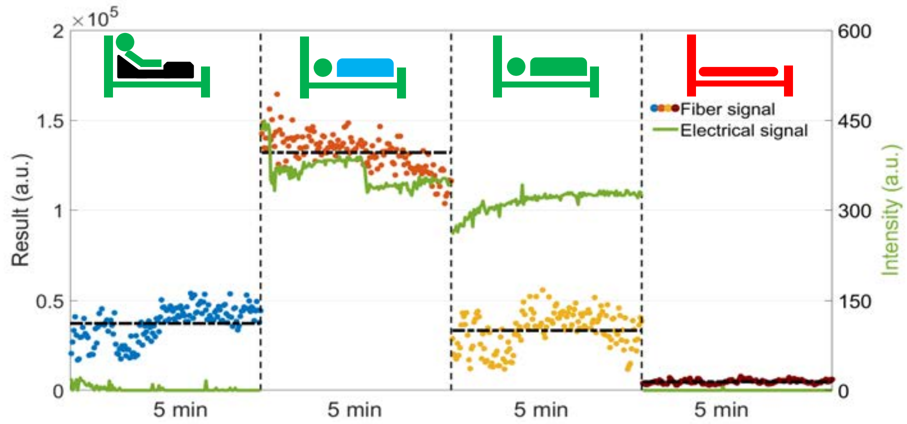

Fig. 6.8: Four activities identification using both optical fiber and electrical pressure sensor results.

In Fig. 6.8, every point stands for the jitter level calculation result based on sectioned data and four colors: blue, orange, yellow and red stand for the results of sit, body movement, on and off bed, respectively. It can be seen from Fig. 6.8 that, combined with signals from electrical pressure sensors, four activities can be distinguished successfully.

Other than four activities recognition, the vital signs can also be obtained, including the heartbeat and respiration. The wavelet analysis method is utilized on the signal of on-bed activity, and the results are shown as Fig. 6.9 (a). Fig. 6.9 (b) shows the comparison between the extracted heartbeat signal from Fig. 6.9 (a) and reference signal obtained simultaneously from commercial ECG monitor (AD8232, Sparkfun). Similarly, obtained respiration signal and compared results are shown in Fig. 6.9 (c). It can be seen that both heartbeat and respiration signals match well with the corresponding signals from commercial devices, which demonstrated that this bed sensor can also detect vital signs accurately.

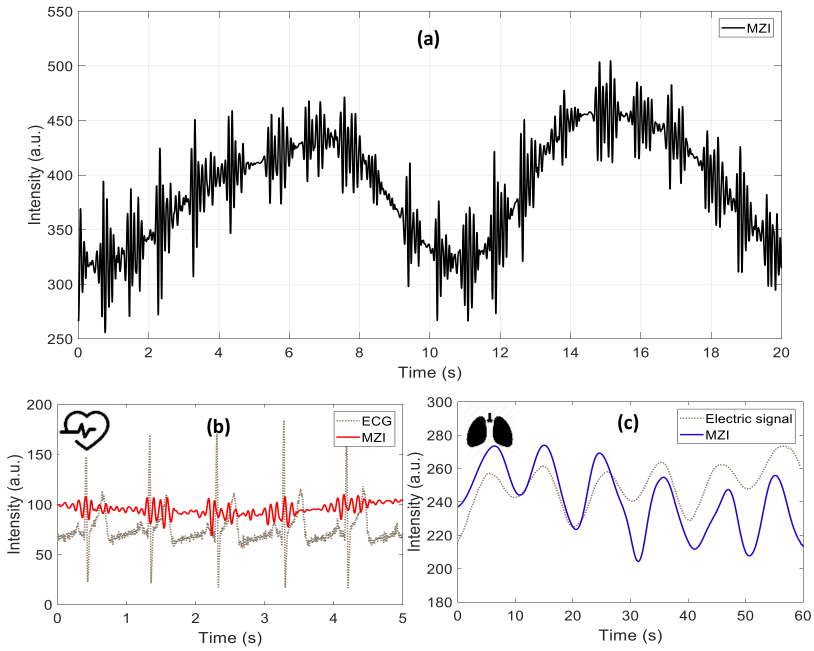

Fig. 6.9: Vital signs monitoring results based on MZI (a), including the recovered heartbeat waveform (b) and respiration waveform (c).

6.4 RAM system test and discussion

For the sake of patients' safety, most of the assisted living facilities are equipped as fewer outlets in a room as possible. For example, some nursing houses in Hong Kong are only equipped one outlet in a room which accommodates several beds. In addition, power consumption has always been a concern in practical usage of RAM system, especially in the nursing house. Thus, the rechargeable bed sensors with low power consumption will be more preferred for ADRD caregiving. For the upcoming application of our RAM system on a local nursing house, the power consumption of every component is summarized, and the power-saving result output algorithm is designed, which is shown in Fig. 6.10 (a) and (b). The total power consumption is 74 mA while the laser and detector account for 19%. In order to save power under normal working conditions, the laser and detector are controlled automatically by the regulator using our algorithm in Fig. 6.7 (b). OT, ET and MT represent Off bed, Electrical and Movement Threshold, which are obtained from Fig. 6.8 to distinguish and output four activities highlighted in Fig. 6.10 (b). Consequently, the RAM system can be allowed to operate over one week without recharging.

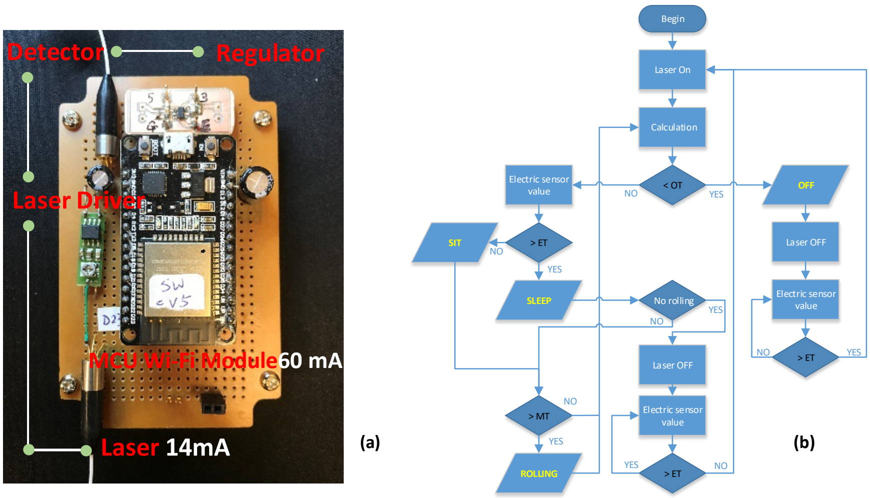

Fig. 6.10: Power consumption of every component in RAM system (a) and the algorithm design for activity recognition and automatic system on/off (b).

In order to make sure stable practical usage of the RAM system, the stability test beforehand is necessary. In our test, six subjects with a difference on gender and weight are selected, and they are arranged to conduct four activities on bed. The duration of every activity is about one hour. We stay aside to monitor their real activities meanwhile and collect the results output from the RAM system, which updates messages 20 times per minutes. The collected results are shown in Fig. 6.11. The X-axis represents the test duration of subjects under our direct observation while the Y-axis is the corresponding output result from the RAM system. It can be seen that the monitoring results of OFF and MOVE agree well with those from direct observation. The misjudgment from ON to MOVE is inevitable as well as acceptable in the practical application while the misjudgment from SIT to OFF may be due to the fact that subjects with low weight sit uncommonly on the corner of the bed and stay still for a while. In summary, the results show that the optical fiber MZI-based RAM system owns high-level stability.

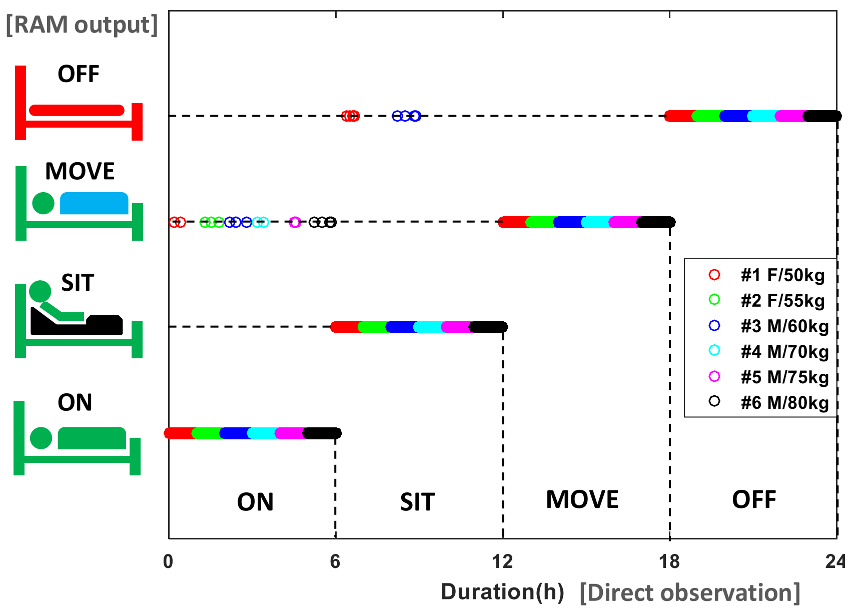

Fig. 6.11: Stability test with comparison between RAM system output and direct observation.

The most popular bed sensor in the RAM system is the traditional electrical sensor. Bed sensors recently proposed also include one kind of optical fiber sensor, in which specific structure is designed based on the weight induced bending loss on optical fibers [82]. This bending loss (BL)-based optical fiber bed sensors can be even used for vital signs monitoring. Compared with these sensors, our proposed MZI optical fiber bed sensor owns distinct advantages. On the one hand, most of them are based on the direct pressure change imposed on the mattress, no matter the electrical sensor or BL-based optical fiber sensor. This may result in the disability to distinguish human or just weight on the bed, which may cause a false alarm or even more severe outcome in practical usage. On the other hand, current bed sensors fail to fully cover the bed resulting in the alarm error when the patients do not sit on the sensing area accidentally. Based on the vibration induced by the blood flow, our sensitive bed sensor can successfully identify between the patient and weight on bed wherever the location is. Other than these, the fabrication complexity, cost, recognizable activities, the ability to monitor vital signs are also compared between current bed sensors and ours, which are summarized in Table. 6.1.

Table 6.1 Performance comparison of RAM system based on optical fiber MZI, electrical sensors and BL-based optical fiber sensors.

	MZI [optical fiber]	**Electrical sensor**	**BL [optical fiber]**
Fabrication complexity	Low	Medium	High
Cost	Low	Medium	Medium
Recognizable activity	ON/OFF/SIT/MOVE	ON/OFF	ON/OFF
Vital signs monitoring	Yes	No	Yes
Coverage area	Whole bed	Sensor area	Sensor area
Rechargeable Battery	Yes	No	No
Stability	High	High	Medium
Human/weight identification	Yes	No	No

In summary, a novel RAM system is proposed based on optical fiber sensors as a bed sensing unit for the ADRD caregiving. Traditional MZI is utilized and embedded under the mattress for non-invasive activities monitoring. All the components, including the laser, detector and MCU Wi-Fi module, are integrated on a chip, and the wireless network infrastructure is designed for practical deployment. This RAM system can not only recognize four activities, including ON bed/SIT on bed/OFF bed/Body movement but also monitor the vital signs of patients, such as respiration and heartbeat rate. Power consumption is also analyzed, and the proposed power-saving algorithm allows the system to operate over one week without recharging. The stability test was also conducted, the result of which demonstrates that this RAM system can work with stable performance. This novel optical fiber MZI-based RAM system can be an effective solution for ADRD patients.

6.5 Myocardial contractility assessment

Myocardial contractility, together with cardiac output, can fully characterize the function or state of a heart [121]. Unlike measurement on cardiac output volume with various methods, the assessment of myocardial contractility is challenging, and it can be only realized clinically by inserting a catheter into the left ventricle to measure the time derivative of left ventricular pressure [122,123]. This disadvantage of discomforting the patients urges another non-invasive standard or parameter to assess myocardial contractility. The pre-ejection period (PEP) is the isovolumetric contract time interval of the heart and is also demonstrated to be an indicator for contractility [124,125]. Each cardiac cycle is composed of electrical and mechanical signals, in which the electrical signal precedes the mechanical conventionally. Currently, PEP can be measured as the time interval from ECG Q-wave (electrical signal) to ICG B-wave (mechanical signal). However, due to the intrinsic disadvantages of invasive and unstable detection, this method is not popular clinically. To realize non-invasive, unobtrusive and inexpensive method for PEP measurement, researchers derived a parameter from the BCG and ECG signal, which is the interval between R-wave of ECG and J-wave of BCG (R-J interval), and demonstrated that it is highly correlated to PEP from 2126 heartbeats across ten subjects [126]. We follow this method and achieve the myocardial contractility assessment using the MZI based vital signs monitoring system.

The myocardial contractility assessment experimental setup is shown in Fig. 6.12. The MZI is packaged and embedded in a cushion, which is placed on the chair. The reason why this system is performed using cushion is that the BCG signal shows the largest amplitude change in head-to-foot direction. BCG signal is collected using optical fiber sensors while the ECG signal is obtained from the same commercially available device aforementioned above. The DAQ card works under the sampling rate of 1 kHz and BCG, as well as ECG signal, are recorded simultaneously using two independent channels.

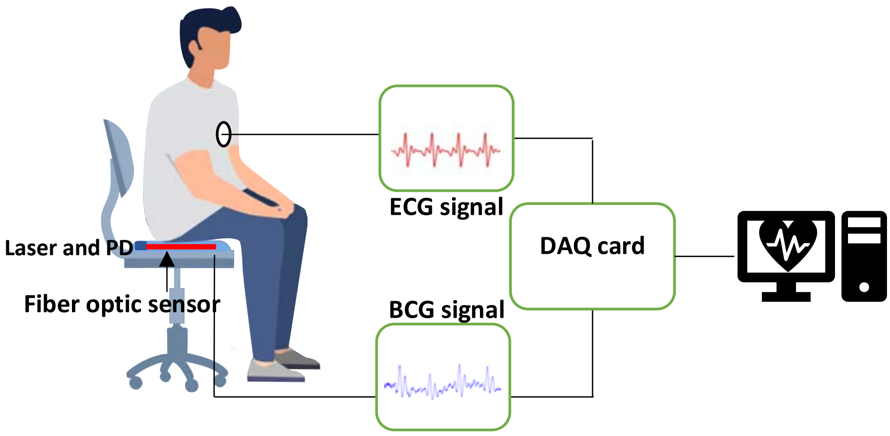

Fig. 6.12: Myocardial contractility assessment experimental setup.

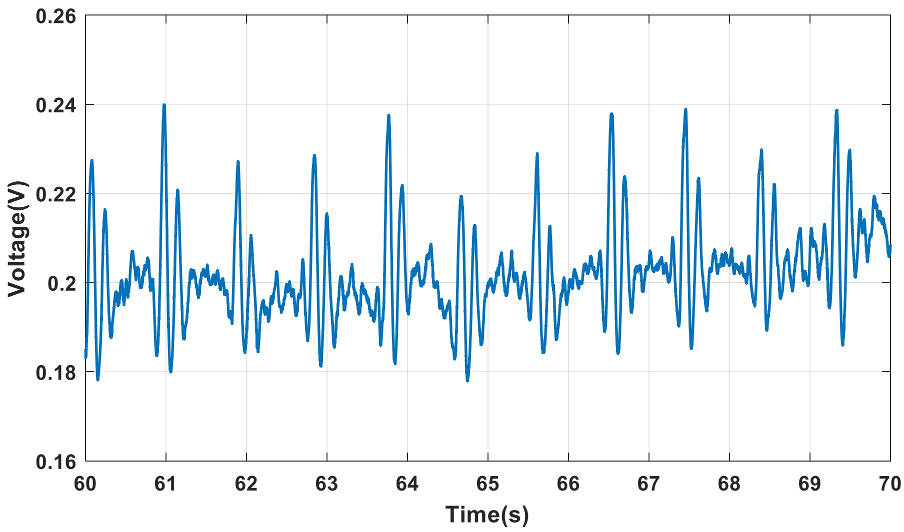

Fig. 6.13: BCG signal from optical fiber sensors.

BCG signal from the optical fiber MZI system is shown in Fig. 6.13. It can be seen that *J* peak in the BCG signal can be obtained easily, and the other detailed peaks also appear. At the same time, the ECG signal is recorded and shown in Fig. 6.14, in which the highest peak, R peak, can also be distinguished. J peak in BCG and R peak in ECG signal are used for R-J interval calculation.

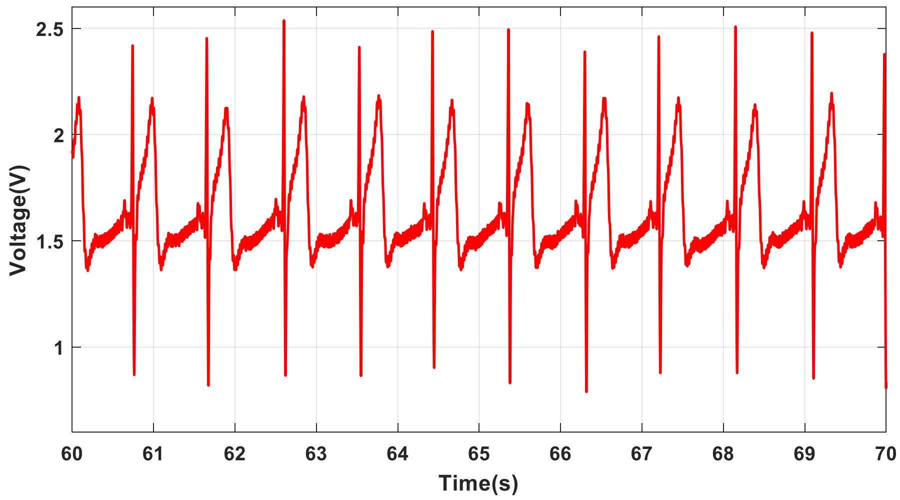

Fig. 6.14: ECG signal from AD8232.

To demonstrate the effectiveness of R-J interval for myocardial contractility assessment, contractility is changed intentionally, which can be characterized by PEP change. At the same time, the R-J interval is monitored so that the dynamic relationship between PEP and R-J interval can be obtained. Valsalva maneuver is traditionally used for contractility modulation in clinical test, and we also apply this manner to change PEP. In the beginning, the subject is instructed to remain still for 1 min and then perform the Valsalva maneuver and hold the strain period for about 20 seconds. Then the subjects release freely and stay still for about 1 min to recover. During this process, BCG and ECG signals are recorded synchronously, and R-J interval within this process of 80 s is obtained by off-line data processing. The results are shown in Fig. 6.15, in which ECG, BCG and R-J interval are shown from top to bottom. In the R-J interval result, it can be seen that, during the initial state about 20 s, the PEP keeps unchanged about 240 ms. Then, with the Valsalva maneuver, the R-J interval decreases suddenly to about 200 ms and then increases continuously back to 240 ms in normal state. This is due to the myocardial contractility change with the Valsalva maneuver.

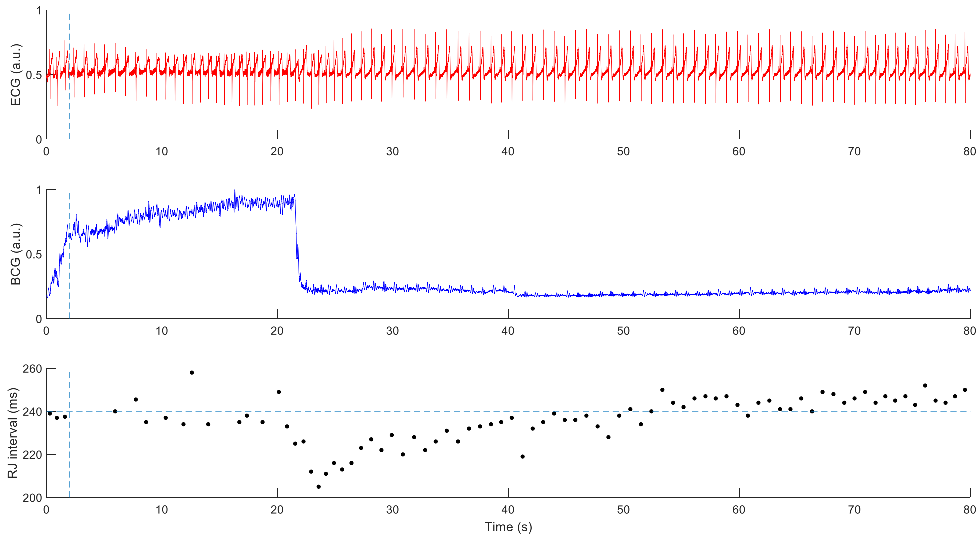

Fig. 6.15: R-J interval change induced by Valsalva maneuver.

It has been investigated quantitatively that the relationship between the PEP and R-J interval follows [126]:

$$y_{RJ} = 1.05 x_{PEP} + 138. \tag{6.1}$$

Then, the PEP above can be calculated, and the result is shown in Fig. 6.14.

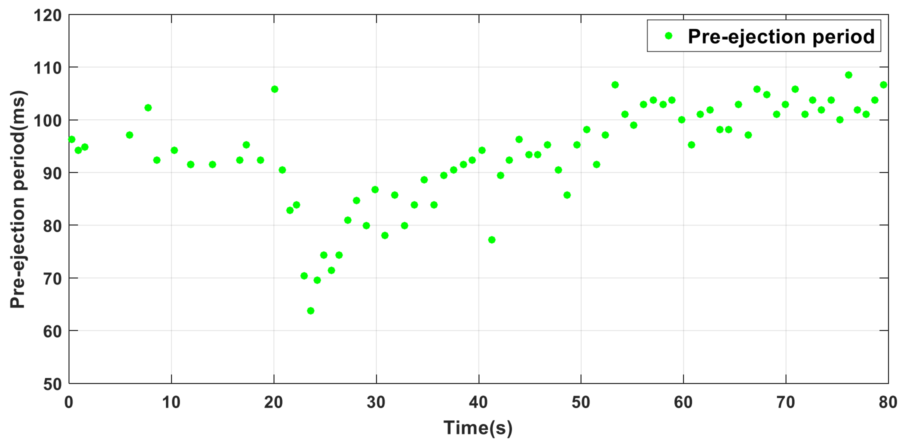

Fig. 6.16: Pre-ejection period measurement result.

In summary, myocardial contractility assessment is achieved by using optical fiber sensors. This kind of contractility is related to PEP, which can be replaced by the R-J interval parameter. R peak can be obtained from BCG signals using the optical fiber MZI, and J peak is from ECG signals. To demonstrate, PEP is modulated by Valsalva maneuver, and the R-J interval is obtained from synchronized BCG and ECG signals. Results show the PEP change during the whole process, which demonstrates that myocardial contractility assessment can be realized using optical fiber sensors.

6.6 Summary

RAM system is proposed for non-invasive remote activities monitoring for ADRD patients and caregivers. The RAM system includes optical fiber MZI, wireless network, and monitoring console. The optical fiber MZI is fabricated by splicing two couplers together to form both sensing arm and reference arm. The length difference of two arms is optimized to increase the sensitivity as high as possible. The DFB laser source with a single wavelength is employed, and the performance is tested, including output power and wavelength variation under different driving currents. Low-cost photodetector is utilized in the circuit with the laser source, driver and regulator. A Wi-Fi module named ESP32 is applied in the system to realize wireless communication. According to the collected data, a jitter level calculation method is employed. Combined with one electric pressure sensor, four activities can be distinguished: ON/OFF/MOVEMENT/SIT. Other than activities, HR and RR can also be monitored successfully. Power consumption of every component is analyzed, and the algorithm is designed to lower the power consumption. Finally, the RAM test is conducted, and the results show the stable performance of the RAM system.

Then, combined with the ECG device, optical fiber MZI is proposed for myocardial contractility assessment. The contractility is modulated by the Valsalva maneuver, during which PEP can be used to assess this contractility. PEP has been demonstrated with a proportional relationship with RJ interval, which can be successfully obtained by BCG from MZI and ECG from AD8232.

7 Summaries and Future works

In this chapter, summaries are given and future works on applications of FMF and MCF sensors are presented.

7.1 Summaries

The SDM system has been widely investigated and FMF as well as MCF, as typical specialty optical fibers in the SDM transmission system, are also explored in a wide range of applications. In the communication area, FMF can be designed with more than one mode supported with excellent transmission performance in the MDM system while MCF can be fabricated with various structures according to different transmission requirements in core-multiplexing systems. Other than the SDM communication system, FMF and MCF can also be good candidates in the optical fiber sensing community and excellent research works were devoted to this. Research work in this thesis focus on the investigation of FMF and MCF and further exploration of their sensing applications.

7.1.1 FMF and its mode characterization and sensing application

FMF, which can support more than one mode propagating through a single optical fiber, is a good candidate for both high-capacity communication and some sensing applications. Chapter 2 firstly introduces SDM, FMF and basic parameters in FMF. Then, based on the Maxwell equation, mode calculation in FMF is described in detail. Electric and intensity field distribution of modes in FMF is obtained, including the FM and HOMs. For the first attempt on sensing application, a MMI is introduced on SMF for temperature sensing. The same MMI structure is fabricated on TMF, and different mode interference performance with more than one mode pair is obtained.

For mode characterization in FMF, chapter 3 presents the S^2 imaging technique, which is based on the mode interference in FMF. The mode characterization experiment is conducted on two kinds of FMF: TMF and four-mode fiber, and data processing methods using filtering techniques are introduced. Based on this, mode properties are obtained, including DMGD between FM and HOMs, intensity as well as phase distribution of modes, and distributed and discrete mode coupling. Also, the standard S^2 imaging system is modified to mitigate the EMI, which can help to improve the measurement accuracy. At last, the PCA method is utilized for interference mode pairs classification.

7.1.2 MCF and its application on torsion sensing

Other than FMF, MCF is also a promising candidate in the SDM system, in which different cores can be regarded as independent channels for information transmission. Core-mode coupling exists in MCF, which can be utilized for torsion sensing. Chapter 4 proposes a torsion sensor based on inter-core mode coupling in SCF. Taper structure is fabricated on SCF with an optimized dimension. Under different twist angles on tapered SCF, the obtained spectrum experiences red-shift with increasing sensitivities. The detailed analysis of sensitivity performance shows that this torsion sensor owns tunable sensitivity, which can achieve as high as 1 nm/^{o}. In addition, rotation direction discrimination capability is demonstrated by monitoring wavelength shift direction when the tapered SCF is rotated in C.W and C.C.W directions. Repeated experiments are conducted to verify the stability performance of the torsion sensor and quantify the accuracy, the result of which can achieve $\pm 1^{o}$. Theoretically, mode coupling dynamics as well as optical anisotropy theory are introduced to analyze the torsion sensitivity performance and results agree well with the experiments.

7.1.3 FMF and MCF for non-invasive vital signs monitoring

Other than conventional industrial applications, FMF and MCF also own the potential in the healthcare area, such as vital signs monitoring. In chapter 5, vital signs signal, including HR and RR, are firstly introduced and corresponding techniques to realize HR and RR monitoring are presented, including wearable devices and Wi-Fi techniques in a non-invasive way. To achieve non-invasive vital signs monitoring, FMF and MCF are proposed then. TCF based sensor is firstly designed and fabricated with an optimized dimension. Then, it is packaged under the mattress to realize non-invasive vital signs signals collection in the experimental setup. Based on filtering techniques, breath and heartbeat can be extracted simultaneously from raw data, and HR and RR are then obtained, which match well with reference signals. For further applications, post-exercise physiological activities characterization using this TCF-based sensor is achieved. In theory, supermode interference in TCF is introduced and curvature sensing experiments are conducted with achieved sensitivity as high as 18 nm/m^{-1}, which supports its excellent vital signs monitoring performance.

Apart from TCF, two kinds of FMFs, including TMF and four-mode fiber, and SCF, are also explored for non-invasive vital signs monitoring. The offset distances between SMF and FMF/SCF are analyzed in the experiment to achieve good interference with high sensitivities. As demonstrated, both TMF and four-mode fiber can realize simultaneous HR and RR monitoring with an acceptable accuracy. For SCF, MMF is introduced between SMF and SCF to fully excite all the cores in order to form interference between center-core mode and surrounding outer-core modes. This SCF in-line interferometer can realize RR monitoring.

7.1.4 MZI for remote activity monitoring and myocardial contractility assessment

Chapter 6 further explores the healthcare applications of optical fiber sensors. The first is the RAM system for ADRD patients and caregivers. MZI, which is fabricated by splicing two couplers with optimized arm length difference, is employed here in the form of a smart mattress. All the components, including the DFB laser source, detector, driver, regulator and MCU, are integrated together. As a result, the activities of ON/OFF/MOVE/SIT can be distinguished using the proposed as well as optimized jitter level calculation method. Other than activities, vital signs can also be obtained, including HR and RR. Power consumption of this RAM system is considered, and the test is conducted with stable monitoring performance.

Another application of MZI is explored, which is the myocardial contractility assessment. A smart cushion embedded with MZI is utilized for complete as well as accurate BCG signal collection. This BCG signal can be used for PEP measurement combined with ECG signals. PEP is a conventional parameter to evaluate the myocardial contractility. Valsalva maneuver is introduced to modulate the PEP, which is totally characterized by optical fiber MZI in a non-invasive way.

7.2 Future works

Based on current systems and results presented in this thesis, the future works are illustrated in this section.

7.2.1 Mode coupling dynamics characterization in FMF

As introduced above, in the S^2 imaging system, both discrete and distributed mode coupling can be obtained quantitively. The mode coupling results are measured under stable or unchanged ambiance, such as room temperature and free strain. Based on the coupled-mode theory, the power exchange between modes in FMF is highly sensitive with the RI change of core, which can be modulated by temperature and strain. Also, they follow some specific coefficients. Therefore, mode coupling dynamics under variational ambiance can be characterized, and related parameters regarding HOMs can be obtained, which is of significance on future FMF sensing performance analysis and applications. In the meantime, the response of HOMs on many physical parameters can be obtained.

7.2.2 Specialty MCF design and fabrication for vital signs monitoring

As introduced above, the in-line optical fiber interferometers employing MCF, especially TCF, show excellent performance on the application of vital signs monitoring. Superior to MZI, MCF-based in-line optical fiber interferometers own the advantages of spectral stability and ease of packaging. However, during the experiment, desired vital signs signal detection usually depends on the layout of two cores, variation of which may impact the sensitivity. This can be analyzed based on the curvature sensing results. The interference between cores contributes to high curvature sensitivity and TCF is just the first attempt. Thus, to overcome the dependence of core layout in TCF on sensitivity, specialty MCF with different core arrangements, such as four-core fiber with one central core and three outer-cores in a triangle form, can be designed and homemade for vital signs monitoring with high sensitivity and stability in the meantime.

7.2.3 Filter-free detailed BCG characterization using MZI

BCG is the mechanical signal generated during the heart pumping blood, and accurate or detailed BCG signal extraction is necessary for characterization on heart activities. Standard BCG signal is composed of five peaks, including *H, I, J, K, L*, which can be used to describe single blood-pumping cycle fully. Their amplitudes and the intervals between these peaks are significant, and abnormal BCG signal is directly related to some heart diseases. Currently, the most effective way to measure these peaks is based on the electric sensors in the form of weight scale, and many kinds of filtering techniques in both software and hardware are utilized. The filtering techniques inevitably cause amplitude change and phase shift on the original signal, which results in inaccurate BCG signal extraction. In chapter 6, MZI has been demonstrated with high sensitivity for this BCG signal extraction as shown in Fig.

6.13. Further work can thus focus on the package of MZI and optimization on laser source, such as the feedback wavelength control, to fully detect detailed BCG signals with accurate and stable performance.

7.2.4 Specific cardiovascular diseases diagnose based on BCG and ECG signals using big data analysis methods

MZI has been demonstrated with excellent performance to measure BCG signals in detail. The peaks in the BCG signal represent the blood pumping process in a mechanical way. With accurate and comprehensive BCG signal measurement, the working process of the heart can be fully characterized. With a sufficient dataset of BCG and specifically developed machine learning algorithms, other than HR monitoring, many heart diseases may also be potentially detected or diagnosed. On the other hand, BCG and ECG signal can characterize the heart function in both mechanical and electrical way. With synchronized BCG and ECG signals, using big data analysis methods, some cardiovascular and cerebrovascular diseases can be linked with some abnormal heart activities, which is of great significance for early diagnose of specific heart diseases.

Bibliography

1. K. C. Kao and G. A. Hockham, "Dielectric-fibre surface waveguides for optical frequencies," Proceedings of the Institution of Electrical Engineers **113**, 1151–1158 (1966).

2. G. P. Agrawal, *Fiber-Optic Communication Systems*, John Wiley & Sons, **222**, (2012).

3. G. Li, N. Bai, N. Zhao, and C. Xia, "Space-division multiplexing: the next frontier in optical communication," Advances in Optics and Photonics **6**, 413–487 (2014).

4. N. Bai, E. Ip, Y.-K. Huang, E. Mateo, F. Yaman, M.-J. Li, S. Bickham, S. Ten, J. Liñares, C. Montero, V. Moreno, X. Prieto, V. Tse, K. Man Chung, A. P. T. Lau, H.-Y. Tam, C. Lu, Y. Luo, G.-D. Peng, G. Li, and T. Wang, "Mode-division multiplexed transmission with inline few-mode fiber amplifier," Optics Express **20**, 2668 (2012).

5. A. Li, Y. Wang, and W. Shieh, "Few-mode fiber based optical sensors," 2015 IEEE Photonics Conference, IPC 2015 **23**, 319–320 (2015).

6. H. Yuan, A. Saljoghei, T. Hayashi, T. Nakanishi, E. Sillekens, L. Galdino, P. Bayvel, Z. Liu, and G. Zervas, "Experimental Investigation of Static and Dynamic Crosstalk in Trench-Assisted Multi-Core Fiber," in *2019 Optical Fiber Communications Conference and Exhibition, OFC 2019*, pp. 1–3 (2019).

7. R. Ryf, R. J. Essiambre, S. Randel, A. H. Gnauck, P. J. Winzer, T. Hayashi, T. Taru, and T. Sasaki, "MIMO-based crosstalk suppression in spatially multiplexed 3 × 56-Gb/s PDM-QPSK signals for strongly coupled three-core fiber," IEEE Photonics Technology Letters **23**, 1469–1471 (2011).

8. T. Sakamoto, K. Saitoh, S. Saitoh, K. Shibahara, M. Wada, Y. Abe, A. Urushibara, K. Takenaga, T. Mizuno, and T. Matsui, "High spatial density six-mode seven-core fibre for repeated dense SDM transmission," in *Proc. 43th Eur. Conf. Exhib. Opt. Commun.* (2017).

9. Y. Amma, Y. Sasaki, K. Takenaga, S. Matsuo, J. Tu, K. Saitoh, M. Koshiba, T. Morioka, and Y. Miyamoto, "High-density multicore fiber with heterogeneous core arrangement," in *2015 Conference on Optical Fiber Communication*, pp. 1-3 (2015).

10. D. Soma, Y. Wakayama, S. Beppu, S. Sumita, T. Tsuritani, T. Hayashi, T. Nagashima, M. Suzuki, M. Yoshida, K. Kasai, M. Nakazawa, H. Takahashi, K. Igarashi, I. Morita, and M. Suzuki, "10.16-Peta-B/s Dense SDM/WDM Transmission over 6-Mode 19-Core Fiber Across the C+L Band," Journal of Lightwave Technology **36**, 1362–1368 (2018).

11. S. Chen, F. Tan, Z. Huang, T. Yang, J. Tu, and C. Yu, "Non-invasive smart monitoring system based on multi-core fiber optic interferometers," in *2018 Asia Communications and Photonics Conference (ACP)*, pp. 1–3 (2018).

12. F. Tan, Z. Liu, J. Tu, C. Yu, C. Lu, and H.-Y. Tam, "Torsion sensor based on inter-core mode coupling in seven-core fiber," Optics Express **26**, 19835 (2018).

13. M. Wang, H. Wu, M. Tang, Z. Zhao, Y. Dang, C. Zhao, R. Liao, W. Chen, S. Fu, C. Yang, W. Tong, P. P. Shum, and D. Liu, "Few-mode fiber based Raman distributed temperature sensing," Optics Express **25**, 4907 (2017).

14. Z. Zhao, M. A. Soto, M. Tang, and L. Thévenaz, "Distributed shape sensing using Brillouin scattering in multi-core fibers," Optics Express **24**, 25211 (2016).

15. A. Li, Y. Wang, and W. Shieh, "Few-mode fiber based optical sensors," in

2015 IEEE Photonics Conference (IPC), pp. 319–320 (2015).

16. J. Montoya, C. Hwang, D. Martz, C. Aleshire, T. Y. Fan, and D. J. Ripin, "Photonic lantern kW-class fiber amplifier," Optics Express **25**, 27543 (2017).
17. N. K. Fontaine, C. R. Doerr, M. A. Mestre, R. R. Ryf, P. J. Winzer, L. L. Buhl, Y. Sun, X. Jiang, and R. Lingle, "Space-division multiplexing and all-optical MIMO demultiplexing using a photonic integrated circuit," in *OFC/NFOEC* pp. 1–3 (2012).
18. T. Morioka, "New generation optical infrastructure technologies: "EXAT initiative" towards 2020 and beyond," *in 14th OptoElectronics and Communications Conference, OECC 2009*, pp. 1–2 (2009).
19. J. M. Fini, B. Zhu, T. F. Taunay, and M. F. Yan, "Statistics of crosstalk in bent multicore fibers," Optics express **18**, 15122–15129 (2010).
20. S. Randel, "Space-division multiplexed transmission," in *2013 Optical Fiber Communication Conference and Exposition and the National Fiber Optic Engineers Conference (OFC/NFOEC)*, pp. 1–60 (2013).
21. F. Yaman, N. Bai, B. Zhu, T. Wang, and G. Li, "Long distance transmission in few-mode fibers," Optics Express **18**, 13250–13257 (2010).
22. A. W. Snyder, "Coupled-Mode Theory for Optical Fibers.," J. Opt. Soc. Am **62**, 1267–1277 (1973).
23. B. Dong, Z. Shen, C. Yu, and Y. Wang, "Modal Excitations in Fully and Partially Ethanol-Filled Photonic Bandgap Fibers and Their Applications as Fiber Sensors," Journal of Lightwave Technology **34**, 3853–3858 (2016).
24. B. Dong, Y. Ge, Y. Wang, and C. Yu, "High extinction-ratio dual thin-taper fiber interferometer fabricated by arc-discharge and its performance as sensors," Optics Communications **355**, 225–229 (2015).
25. B. Dong, Y. Peng, Y. Wang, and C. Yu, "Mode division multiplexing in a

fiber modal interferometer for dual-parameters measurement," IEEE Photonics Technology Letters **28**, 143–146 (2016).

26. S. Ramachandran, Z. Wang, and M. Yan, "Bandwidth control of long-period grating-based mode converters in few-mode fibers," Optics Letters **27**, 698 (2002).

27. B. Dong, Y. Wang, and C. Yu, "Intensity-modulated micro-displacement sensor with an embedded fiber dual cladding modes interferometer," Sensors and Actuators, A: Physical **236**, 334–337 (2015).

28. N. K. Fontaine, R. Ryf, H. Chen, A. V. Benitez, J. E. Antonio Lopez, R. Amezcua Correa, B. Guan, B. Ercan, R. P. Scott, S. J. Ben Yoo, L. Grüner-Nielsen, Y. Sun, and R. J. Lingle, "30×30 MIMO transmission over 15 spatial modes," *in Optical Fiber Communication Conference, OFC 2015*, pp. 20–22 (2015).

29. Y. Jung, Q. Kang, J. K. Sahu, B. Corbett, J. O'Callagham, F. Poletti, S. U. Alam, and D. J. Richardson, "Reconfigurable modal gain control of a few-mode EDFA supporting six spatial modes," IEEE Photonics Technology Letters **26**, 1100–1103 (2014).

30. K. P. Ho and J. M. Kahn, "Mode Coupling and Its Impact on Spatially Multiplexed Systems," Elsevier Inc., (2013).

31. D. J. Richardson, J. M. Fini, and L. E. Nelson, "Space-division multiplexing in optical fibres," Nature Photonics **7**, 354–362 (2013).

32. R. Maruyama, N. Kuwaki, S. Matsuo, and M. Ohashi, "Experimental investigation of relation between mode-coupling and fiber characteristics in few-mode fibers," *in 2015 Conference on Optical Fiber Communication*, pp. 1–3 (2015).

33. M. Nakazawa, M. Yoshida, and T. Hirooka, "Measurement of Mode

Coupling Distribution Along a Few-Mode Fiber Using a Synchronous Multi-Channel OTDR," in *Optical Fiber Communication Conference 2014*, 454–456 (2014).

34. J. W. Nicholson, A. D. Yablon, J. M. Fini, and M. D. Mermelstein, "Measuring the modal content of large-mode-area fibers," IEEE Journal on Selected Topics in Quantum Electronics **15**, 61–70 (2009).

35. K. Jespersen, Z. Li, L. Gruner-Nielsen, B. Palsdottir, F. Poletti, and J. W. Nicholson, "Measuring distributed mode scattering in long, few-moded fibers," in *Optical Fiber Communication Conference 2012*, OTh3I-4 (2012).

36. J. W. Nicholson, A. D. Yablon, S. Ramachandran, and S. Ghalmi, "Spatially and spectrally resolved imaging of modal content in large-mode-area fibers," Optics Express **16**, 7233 (2008).

37. J. Su, X. Dong, and C. Lu, "Property of Bent Few-Mode Fiber and Its Application in Displacement Sensor," IEEE Photonics Technology Letters **28**, 1387–1390 (2016).

38. Y. Weng, E. Ip, Z. Pan, and T. Wang, "Single-end simultaneous temperature and strain sensing techniques based on Brillouin optical time domain reflectometry in few-mode fibers," Optics Express **23**, 9024 (2015).

39. F. Tan, C. Yu, J. Zhao, and G. Li, "Accurate measurement of total mode coupling in few mode fibers (FMFs) based on a modified spatial and spectral resolved (S^2) imaging system," in *2017 Opto-Electronics and Communications Conference (OECC) and Photonics Global Conference (PGC)*, pp. 1–2 (2017).

40. F. Tan, J. Zhao, Q. Mo, and G. Li, "A modified spatial and spectral (S^2) imaging system based on electromagnetic disturbance mitigation," in *Asia Communications and Photonics Conference*, pp. 1-3 (2015).

41. B. Sévigny, G. Le Cocq, C. C. C. Carrero, C. Valentin, P. Sillard, G. Bouwmans, L. Bigot, and Y. Quiquempois, "Advanced S2 imaging: Application of multivariate statistical analysis to spatially and spectrally resolved datasets," Journal of Lightwave Technology **32**, 4004–4010 (2014).

42. R. Xu, A. Yurkewich, and R. V Patel, "Curvature, torsion, and force sensing in continuum robots using helically wrapped FBG sensors," IEEE Robotics and Automation Letters **1**, 1052–1059 (2016).

43. M. Kristensen, L. Nielsen, and L. Glavind, "A Multicore Fiber Sensor for Monitoring Twists of Wind Turbine Parts," in *Bragg Gratings, Photosensitivity, and Poling in Glass Waveguides*, BM5B-6 (2016).

44. X. Dong, Z. Xie, Y. Song, K. Yin, Z. Luo, J. Duan, and C. Wang, "Highly sensitive torsion sensor based on long period fiber grating fabricated by femtosecond laser pulses," Optics & Laser Technology **97**, 248–253 (2017).

45. B. Huang and X. Shu, "Highly sensitive torsion sensor with femtosecond laser-induced low birefringence single-mode fiber based Sagnac interferometer," Optics express **26**, 4563–4571 (2018).

46. H. Zhang, Z. Wu, P. P. Shum, X. Shao, R. Wang, X. Q. Dinh, S. Fu, W. Tong, and M. Tang, "Directional torsion and temperature discrimination based on a multicore fiber with a helical structure," Optics express **26**, 544–551 (2018).

47. K. Shibahara, T. Mizuno, D. Lee, Y. Miyamoto, H. Ono, K. Nakajima, Y. Amma, K. Takenaga, and K. Saitoh, "DMD-Unmanaged Long-Haul SDM Transmission Over 2500-km 12-Core× 3-Mode MC-FMF and 6300-km 3-Mode FMF Employing Intermodal Interference Canceling Technique," Journal of Lightwave Technology **37**, 138–147 (2019).

48. K. Pulverer, T. Tanaka, U. Häbel, C. Castro, M. Bohn, T. Mizuno, A. Isoda, K. Shibahara, T. Inui, and Y. Miyamoto, "First demonstration of single-mode

MCF transport network with crosstalk-aware in-service optical channel control," in *2017 European Conference on Optical Communication (ECOC)*, pp. 1–3 (2017).

49. J. M. D. Mendinueta, S. Shinada, R. S. Luis, Y. Hirota, H. Furukawa, H. Harai, and N. Wada, "Experimental Demonstration of a 53 Tb/s Coherent SDM-TDM Add/Drop/Through Optical Network with Time-division Spatial Super-channels and High-speed Joint Switching System," in *2017 European Conference on Optical Communication (ECOC)*, pp. 1–3 (2017).

50. A. S. Kurkov, S. A. Babin, I. A. Lobach, and S. I. Kablukov, "New mechanism of the mode coupling in multi-core fiber lasers," Fiber Lasers V: Technology, Systems, and Applications, **33**, (2008).

51. Y. Huo, G. G. King, and P. K. Cheo, "Second-harmonic generation using a high-energy and tunable Q-switched multicore fiber laser," IEEE Photonics Technology Letters **16**, 2224–2226 (2004).

52. J. E. Antonio-Lopez, Z. S. Eznaveh, P. LiKamWa, A. Schülzgen, and R. Amezcua-Correa, "Multicore fiber sensor for high-temperature applications up to 1000 C," Optics letters **39**, 4309–4312 (2014).

53. J. Villatoro, O. Arrizabalaga, G. Durana, I. S. De Ocáriz, E. Antonio-Lopez, J. Zubia, A. Schülzgen, and R. Amezcua-Correa, "Accurate strain sensing based on super-mode interference in strongly coupled multi-core optical fibres," Scientific Reports **7**, 4451 (2017).

54. J. P. Moore and M. D. Rogge, "Shape sensing using multi-core fiber optic cable and parametric curve solutions," Optics Express **20**, 2967 (2012).

55. P. S. Westbrook, T. Kremp, K. S. Feder, W. Ko, E. M. Monberg, H. Wu, D. A. Simoff, T. F. Taunay, and R. M. Ortiz, "Continuous multicore optical fiber grating arrays for distributed sensing applications," Journal of Lightwave

Technology **35**, 1248–1252 (2017).

56. M.-S. Yoon, S.-B. Lee, and Y.-G. Han, "In-line interferometer based on intermodal coupling of a multicore fiber," Optics express **23**, 18316–18322 (2015).

57. F. Ye, J. Tu, K. Saitoh, and T. Morioka, "Simple analytical expression for crosstalk estimation in homogeneous trench-assisted multi-core fibers," Optics Express **22**, 23007 (2014).

58. J. Tu, K. Saitoh, M. Koshiba, K. Takenaga, and S. Matsuo, "Design and analysis of large-effective-area heterogeneous trench-assisted multi-core fiber," Optics express **20**, 15157–15170 (2012).

59. J. Zubia, J. Arrue, and A. Mendioroz, "Theoretical analysis of the torsion-induced optical effect in a plastic optical fiber," Optical Fiber Technology **3**, 162–167 (1997).

60. H. Tai and R. Rogowski, "Optical anisotropy induced by torsion and bending in an optical fiber," Optical Fiber Technology **8**, 162–169 (2002).

61. E. Udd and W. B. Spillman Jr, *Fiber Optic Sensors: An Introduction for Engineers and Scientists*, John Wiley & Sons, (2011).

62. Y. Wang, M. Wang, and X. Huang, "In fiber Bragg grating twist sensor based on analysis of polarization dependent loss," Optics Express **21**, 11913 (2013).

63. O. Frazão, R. M. Silva, J. Kobelke, and K. Schuster, "Temperature-and strain-independent torsion sensor using a fiber loop mirror based on suspended twin-core fiber," Optics letters **35**, 2777–2779 (2010).

64. S. G. Alonso, I. de la Torre Díez, and B. G. Zapiraín, "Predictive, Personalized, Preventive and Participatory (4P) Medicine Applied to Telemedicine and eHealth in the Literature," Journal of Medical Systems **43**, 140 (2019).

65. Y. Khan, A. E. Ostfeld, C. M. Lochner, A. Pierre, and A. C. Arias, "Monitoring of Vital Signs with Flexible and Wearable Medical Devices," Advanced Materials **28**, 4373–4395 (2016).

66. M. Weenk, M. Koeneman, T. H. van de Belt, L. J. L. P. G. Engelen, H. van Goor, and S. J. H. Bredie, "Wireless and continuous monitoring of vital signs in patients at the general ward," Resuscitation **136**, 47–53 (2019).

67. A. Stephenson, J. W. Adams, and M. Vaccarezza, "The vertebrate heart: an evolutionary perspective," Journal of Anatomy **231**, 787–797 (2017).

68. G. A. Fonzo and A. Etkin, "Brain Connectivity Reflects Mental and Physical States in Generalized Anxiety Disorder," Biological Psychiatry **80**, 733–735 (2016).

69. Z. Wang, Z. Yang, and T. Dong, "A Review of Wearable Technologies for Elderly Care that Can Accurately Track Indoor Position, Recognize Physical Activities and Monitor Vital Signs in Real Time," Sensors **17**, 341 (2017).

70. Z. C. Harberman, R. T. Jahn, R. Bose, H. Tun, J. S. Shinbane, R. N. Doshi, P. M. Chang, and L. A. Saxon, "Wireless Smartphone ECG Enables Large-Scale Screening in Diverse Populations," Journal of Cardiovascular Electrophysiology **26**, 520–526 (2015).

71. C. M. Lochner, Y. Khan, A. Pierre, and A. C. Arias, "All-organic optoelectronic sensor for pulse oximetry," Nature Communications **5**, 5745 (2014).

72. J. Harju, A. Tarniceriu, J. Parak, A. Vehkaoja, A. Yli-Hankala, and I. Korhonen, "Monitoring of heart rate and inter-beat intervals with wrist plethysmography in patients with atrial fibrillation," Physiological Measurement **39**, 065007 (2018).

73. B. Desai and U. Chaskar, "Comparison of optical sensors for non-invasive

hemoglobin measurement," in *2016 International Conference on Electrical, Electronics, and Optimization Techniques (ICEEOT)*, pp. 2211–2214 (2016).

74. G. Schwartz, B. C.-K. Tee, J. Mei, A. L. Appleton, D. H. Kim, H. Wang, and Z. Bao, "Flexible polymer transistors with high pressure sensitivity for application in electronic skin and health monitoring," Nature Communications **4**, 1859 (2013).

75. M. Folke, L. Cernerud, M. Ekström, and B. Hök, "Critical review of non-invasive respiratory monitoring in medical care," Medical & Biological Engineering & Computing **41**, 377–383 (2003).

76. O. Mimoz, T. Benard, A. Gaucher, D. Frasca, and B. Debaene, "Accuracy of respiratory rate monitoring using a non-invasive acoustic method after general anaesthesia," British Journal of Anaesthesia **108**, 872–875 (2012).

77. P. Corbishley and E. Rodriguez-Villegas, "Breathing Detection: Towards a Miniaturized, Wearable, Battery-Operated Monitoring System," IEEE Transactions on Biomedical Engineering **55**, 196–204 (2008).

78. J. Liu, Y. Chen, Y. Wang, X. Chen, J. Cheng, and J. Yang, "Monitoring Vital Signs and Postures During Sleep Using WiFi Signals," IEEE Internet of Things Journal **5**, 2071–2084 (2018).

79. M. Nosrati, S. Shahsavari, S. Lee, H. Wang, and N. Tavassolian, "A Concurrent Dual-Beam Phased-Array Doppler Radar Using MIMO Beamforming Techniques for Short-Range Vital-Signs Monitoring," IEEE Transactions on Antennas and Propagation **67**, 2390–2404 (2019).

80. X. Hui and E. C. Kan, "Monitoring vital signs over multiplexed radio by near-field coherent sensing," Nature Electronics **1**, 74–78 (2018).

81. O. T. Inan, P.-F. Migeotte, K.-S. Park, M. Etemadi, K. Tavakolian, R. Casanella, J. Zanetti, J. Tank, I. Funtova, G. K. Prisk, and M. Di Rienzo,

"Ballistocardiography and Seismocardiography: A Review of Recent Advances," IEEE Journal of Biomedical and Health Informatics **19**, 1414–1427 (2015).

82. X. Yang, Z. Chen, C. S. M. Elvin, L. H. Y. Janice, S. H. Ng, J. T. Teo, and R. Wu, "Textile Fiber Optic Microbend Sensor Used for Heartbeat and Respiration Monitoring," IEEE Sensors Journal **15**, 757–761 (2015).

83. J. Guzmán-Sepúlveda, R. Guzmán-Cabrera, M. Torres-Cisneros, J. Sánchez-Mondragón, and D. May-Arrioja, "A Highly Sensitive Fiber Optic Sensor Based on Two-Core Fiber for Refractive Index Measurement," Sensors **13**, 14200–14213 (2013).

84. Y. Zhao, H. Guo, Z. Zheng, L. Yue, Y. Xu, A. Zhou, and L. Yuan, "A novel fiber Michelson interferometer based on cascaded twin core fiber and side-hole fiber," in *2017 25th Optical Fiber Sensors Conference (OFS)*, pp. 1-4 (2017).

85. O. Frazão, S. F. O. Silva, J. Viegas, J. M. Baptista, J. L. Santos, J. Kobelke, and K. Schuster, "All fiber MachZehnder interferometer based on suspended twin-core fiber," IEEE Photonics Technology Letters **22**, 1300–1302 (2010).

86. A. Zhou, G. Li, Y. Zhang, Y. Wang, C. Guan, J. Yang, and L. Yuan, "Asymmetrical Twin-Core Fiber Based Michelson Interferometer for Refractive Index Sensing," Journal of Lightwave Technology **29**, 2985–2991 (2011).

87. S. Feng, H. Li, O. Xu, S. Lu, and S. Jian, "Compact in-fiber Mach-Zehnder interferometer using a twin-core fiber," in *2009 Asia Communications and Photonics Conference and Exhibition*, pp. 1-3 (2009).

88. B. Kim, T.-H. Kim, L. Cui, and Y. Chung, "Twin core photonic crystal fiber for in-line Mach-Zehnder interferometric sensing applications," Optics

Express **17**, 15502 (2009).

89. O. Frazão, R. M. Silva, J. Kobelke, and K. Schuster, "Temperature- and strain-independent torsion sensor using a fiber loop mirror based on suspended twin-core fiber," Optics Letters **35**, 2777 (2010).

90. Z. Li, C. Liao, Y. Wang, L. Xu, D. Wang, X. Dong, S. Liu, Q. Wang, K. Yang, and J. Zhou, "Highly-sensitive gas pressure sensor using twin-core fiber based in-line Mach-Zehnder interferometer," Optics Express **23**, 6673 (2015).

91. Z. Liu, M. V. Tse, C. Wu, D. Chen, C. Lu, and H. Tam, "Intermodal coupling of supermodes in a twin-core photonic crystal fiber and its application as a pressure sensor," Optics Express **20**, 21749 (2012).

92. A. Zhou, Y. Zhang, G. Li, J. Yang, Y. Wang, F. Tian, and L. Yuan, "Optical refractometer based on an asymmetrical twin-core fiber Michelson interferometer," Optics Letters **36**, 3221 (2011).

93. R. Vallée and D. Drolet, "Practical coupling device based on a two-core optical fiber," Applied Optics **33**, 5602 (1994).

94. P. Rugeland and W. Margulis, "Revisiting twin-core fiber sensors for high-temperature measurements," Applied Optics **51**, 6227 (2012).

95. Z. Liu, Y. Wei, Y. Zhang, Y. Zhang, E. Zhao, J. Yang, and L. Yuan, "Twin-core fiber SPR sensor," Optics Letters **40**, 2826 (2015).

96. Jae Hyuk Shin and Kwang Suk Park, "HRV analysis and blood pressure monitoring on weighing scale using BCG," in *2012 Annual International Conference of the IEEE Engineering in Medicine and Biology Society*, pp. 3789–3792 (2012).

97. J. H. Shin, S. H. Hwang, M. H. Chang, and K. S. Park, "Heart rate variability analysis using a ballistocardiogram during Valsalva manoeuvre and post exercise," Physiological Measurement **32**, 1239–1264 (2011).

98. Y. Zhong, K. Jan, K. H. Ju, and K. H. Chon, "Quantifying cardiac sympathetic and parasympathetic nervous activities using principal dynamic modes analysis of heart rate variability," American Journal of Physiology-Heart and Circulatory Physiology **291**, 1475-1483 (2006).

99. R. González-Camarena, S. Carrasco-Sosa, R. Román-Ramos, M. J. Gaitán-González, V. Medina-Bañuelos, and J. Azpiroz-Leehan, "Effect of static and dynamic exercise on heart rate and blood pressure variabilities," Medicine and science in sports and exercise **32**, 1719-1728 (2000).

100. L. Szostkiewicz, M. Napierala, A. Ziolowicz, A. Pytel, T. Tenderenda, and T. Nasilowski, "Cross talk analysis in multicore optical fibers by supermode theory," Optics Letters **41**, 3759 (2016).

101. G. L. Yin, S. Q. Lou, W. L. Lu, and X. Wang, "A high-sensitive fiber curvature sensor using twin core fiber-based filter," Applied Physics B **115**, 99–104 (2014).

102. C. Schulze, R. Bruning, S. Schroter, and M. Duparre, "Mode Coupling in Few-Mode Fibers Induced by Mechanical Stress," Journal of Lightwave Technology **33**, 4488–4496 (2015).

103. A. Association, "2018 Alzheimer's disease facts and figures," Alzheimer's & Dementia **14**, 367–429 (2018).

104. K. L. Lanctôt, J. Amatniek, S. Ancoli-Israel, S. E. Arnold, C. Ballard, J. Cohen-Mansfield, Z. Ismail, C. Lyketsos, D. S. Miller, E. Musiek, R. S. Osorio, P. B. Rosenberg, A. Satlin, D. Steffens, P. Tariot, L. J. Bain, M. C. Carrillo, J. A. Hendrix, H. Jurgens, and B. Boot, "Neuropsychiatric signs and symptoms of Alzheimer's disease: New treatment paradigms," Alzheimer's and Dementia: Translational Research and Clinical Interventions **3**, 440–449 (2017).

105. M. Moran, C. Lynch, C. Walsh, R. Coen, D. Coakley, and B. Lawlor, "Sleep disturbance in mild to moderate Alzheimer's disease," Sleep Medicine **6**, 347–352 (2005).

106. L. Peter-Derex, P. Yammine, H. Bastuji, and B. Croisile, "Sleep and Alzheimer's disease," Sleep Medicine Reviews **19**, 29–38 (2015).

107. K. Brazil, G. Carter, C. Cardwell, M. Clarke, P. Hudson, K. Froggatt, D. McLaughlin, P. Passmore, and W. G. Kernohan, "Effectiveness of advance care planning with family carers in dementia nursing homes: A paired cluster randomized controlled trial," Palliative Medicine **32**, 603–612 (2018).

108. A. Association, "2017 Alzheimer's disease facts and figures," Alzheimer's & Dementia **13**, 325–373 (2017).

109. J. E. Gaugler, M. Reese, and R. Tanler, "Care to Plan: An Online Tool That Offers Tailored Support to Dementia Caregivers," The Gerontologist **56**, 1161–1174 (2016).

110. G. Demiris, *Information Technology to Support Aging: Implications for Caregiving*, Elsevier Inc., (2015).

111. P. Kumari, L. Mathew, and P. Syal, "Increasing trend of wearables and multimodal interface for human activity monitoring: A review," Biosensors and Bioelectronics **90**, 298–307 (2017).

112. V. A. J. Block, E. Pitsch, P. Tahir, B. A. C. Cree, D. D. Allen, and J. M. Gelfand, "Remote Physical Activity Monitoring in Neurological Disease: A Systematic Review," PLOS ONE **11**, 0154335 (2016).

113. K. C. Preusse, T. L. Mitzner, C. B. Fausset, and W. A. Rogers, "Older Adults' Acceptance of Activity Trackers," Journal of Applied Gerontology **36**, 127–155 (2017).

114. M. A. Rowe, A. Kelly, C. Horne, S. Lane, J. Campbell, B. Lehman, C. Phipps,

M. Keller, and A. P. Benito, "Reducing dangerous nighttime events in persons with dementia by using a nighttime monitoring system," Alzheimer's & Dementia **5**, 419–426 (2009).

115. M. Z. Uddin, W. Khaksar, and J. Torresen, "Ambient sensors for elderly care and independent living: A survey," Sensors **18**, 1–31 (2018).

116. M. Mulvenna, A. Hutton, V. Coates, S. Martin, S. Todd, R. Bond, and A. Moorhead, "Views of Caregivers on the Ethics of Assistive Technology Used for Home Surveillance of People Living with Dementia," Neuroethics **10**, 255–266 (2017).

117. K. S. Tanev, A. Winokur, and R. K. Pitman, "Sleep Patterns and Neuropsychiatric Symptoms in Hospitalized Patients With Dementia," The Journal of Neuropsychiatry and Clinical Neurosciences **29**, 248–253 (2017).

118. G. G. Mora, J. M. Kortelainen, E. R. P. Hernandez, M. Tenhunen, A. M. Bianchi, and M. O. Mendez, "Evaluation of Pressure Bed Sensor for Automatic SAHS Screening," IEEE Transactions on Instrumentation and Measurement **64**, 1935–1943 (2015).

119. Y. Xiao, S. A. Mendez, M. Hofmann, M. Gauch, H. Ehlers, D. Ristau, C. Mueller, and H. Zappe, "Sensitivity enhancement of polymeric Mach–Zehnder interferometers by use of thin high-index films," Sensors and Actuators, A: Physical **265**, 181–186 (2017).

120. X. Dong, H. Du, X. Sun, Z. Luo, and J. Duan, "A novel strain sensor with large measurement range based on all fiber mach-zehnder interferometer," Sensors **18**, 1549-1555 (2018).

121. D. M. Thal, K. T. Homan, J. Chen, E. K. Wu, P. M. Hinkle, Z. M. Huang, J. K. Chuprun, J. Song, E. Gao, and J. Y. Cheung, "Paroxetine is a direct inhibitor of g protein-coupled receptor kinase 2 and increases myocardial

contractility," ACS chemical biology **7**, 1830–1839 (2012).

122. M. Pernot, M. Couade, P. Mateo, B. Crozatier, R. Fischmeister, and M. Tanter, "Real-time assessment of myocardial contractility using shear wave imaging," Journal of the American College of Cardiology **58**, 65–72 (2011).

123. N. A. Mensah-Brown, R. T. Wakai, B. Cheulkar, S. Srinivasan, and J. F. Strasburger, "Assessment of left ventricular pre-ejection period in the fetus using simultaneous magnetocardiography and echocardiography," Fetal Diagnosis and Therapy **28**, 167–174 (2010).

124. J. H. Houtveen, P. F. C. Groot, and E. J. C. De Geus, "Effects of variation in posture and respiration on RSA and pre-ejection period," Psychophysiology **42**, 713–719 (2005).

125. C. Velayo, N. Sato, T. Ito, H. Chisaka, N. Yaegashi, K. Okamura, and Y. Kimura, "Understanding congenital heart defects through abdominal fetal electrocardiography: Case reports and clinical implications," Journal of Obstetrics and Gynaecology Research **37**, 428–435 (2011).

126. M. Etemadi, O. T. Inan, L. Giovangrandi, and G. T. A. Kovacs, "Rapid assessment of cardiac contractility on a home bathroom scale," IEEE Transactions on Information Technology in Biomedicine **15**, 864–869 (2011).